



TÉCNICO
LISBOA

Electrical Impedance Tomography - Thorax

Rafael Filipe Lopes Gonçalves

Thesis to obtain the Master of Science Degree in

Biomedical Engineering

Supervisors: Professor Raul Daniel Lavado Carneiro Martins
Professor Maria Isabel de Sousa Rocha

Examination Committee

Chairperson: Professor Mónica Duarte Correia de Oliveira
Supervisor: Professor Raul Daniel Lavado Carneiro Martins
Members of the Committee: Professor Francisco André Corrêa Alegria
Professor Mário João Martins Oliveira

December 2014

“Recomeça...
Se puderes,
Sem angústia e sem pressa.
E os passos que deres,
Nesse caminho duro
Do futuro,
Dá-os em liberdade.
Enquanto não alcances
Não descanses.
De nenhum fruto queiras só metade.”
Miguel Torga, Recomeçar (excerto)

Acknowledgments

My first acknowledgment goes to my Supervisor and Co-Supervisor, Professor Raul Martins and Professor Isabel Rocha, for the challenging task proposed, for introducing me not only to this this area of research but to the research environment and for giving me all the required conditions to carry out this project.

Secondly I would like to thank Bruno Rosa for each of the precious advice in difficult moments regarding technical issues.

Finally I want to thank my family and friends, for giving me all the support I needed, and specially to my parents and to Catarina, for always being there, for their encouragement to surpass all obstacles, never letting me give up, and for never turning a deaf ear to my endless speeches about this work.

Thank you all. Without you, none of this would be possible!

Resumo

O objetivo desta tese consiste no desenvolvimento de um *software* para a obtenção de mapas de impedância do tórax humano recorrendo a métodos de reconstrução linear.

Este *software* destina-se a simular uma tecnologia de tomografia para aplicações biomédicas que consiste na reconstrução de mapas da distribuição de propriedades eletromagnéticas passivas no interior do corpo, designada por tomografia por impedância elétrica.

A obtenção das propriedades eletromagnéticas passivas requer um método de resolução do problema directo, baseado na técnica de integração finita, de forma a modular a interação entre a radiação electromagnética e o corpo, levando à obtenção dos dados necessários para serem utilizados no processo de reconstrução de imagem. Este método foi concebido para ser totalmente automático, de forma a necessitar apenas da intervenção do utilizador em relação à geometria do problema. Este método foi de seguida validado recorrendo a um conjunto de exercícios cujos princípios físicos se encontram bem estabelecidos.

Finalmente, e de forma a obter a reconstrução da imagem, foram implementados os métodos de retroprojeção e retroprojeção filtrada ao longo das linhas de isopotencial. Estas, por sua vez, foram calculadas através do campo elétrico e da transformação de Möbius.

A reconstrução de imagem por tomografia por impedância elétrica, que envolve o método desenvolvido para a resolução do problema inverso, foi primeiramente testado num conjunto de fantasmas¹ a duas dimensões antes de ser finalmente aplicado a uma segmentação de um tórax obtida através de uma tomografia axial computarizada.

Os resultados obtidos foram satisfatórios na medida em que demonstram a aplicabilidade destas tecnologias em ambiente clínico.

Palavras-chave: Tomografia por Impedância Eléctrica, Tórax, Técnica de Integração Finita, Reconstrução 3D.

¹Tradução do autor para *Phantom*. Designa um objeto desenvolvido no campo da imagiologia médica para avaliar, analisar e ajustar o desempenho de vários dispositivos de imagem.

Abstract

The objective of this thesis is to develop an imaging software to perform linear reconstruction imaging to a human thorax.

This software is intended to simulate a tomographic imaging technology aimed for biomedical applications, the electrical impedance tomography, consisting in the reconstruction of body interior distribution maps of the passive electromagnetic properties.

To accomplish this goal a numerical forward method, based on the finite integration technique, was first implemented to modulate the interaction between the electromagnetic radiation and the body, producing the required data to be subsequently used in the image reconstruction process. This method was intended to be fully automatic, requiring only some input from the user regarding the problem geometry. This method was first validated with a set of well established physics problems.

Finally, for the image reconstruction, the back-projection and the filtered back-projection methods were implemented along isopotential lines which were calculated using the electrical field and the Möbius transformation. Still regarding the electrical impedance tomography image reconstruction, the applicability of the developed inverse problem was first tested in a set of two dimensional phantoms, and later applied to a thorax obtained with image segmentation of a x-ray computed tomography scan.

The results achieved were satisfying in the sense that they demonstrate the applicability of these technologies to clinical environment.

Keywords: Electrical Impedance Tomography, Thorax, Finite Integration Technique, 3D Reconstruction.

Contents

Acknowledgments	v
Resumo	vii
Abstract	ix
List of Tables	xiii
List of Figures	xviii
List of Acronyms	xx
List of Symbols	xxii
1 Introduction	1
1.1 Motivation and Objectives	1
1.2 Organization of the Thesis	2
2 Context and State of the Art	5
2.1 Bioimpedance	5
2.1.1 Definition	5
2.1.2 State of the Art	8
2.2 Electrical Impedance Tomography	9
2.2.1 Definition	9
2.2.2 State of the Art	10
3 EIT Forward Problem	15
3.1 Maxwell's Equations	15
3.2 Finite Integration Technique	18
3.2.1 Maxwell-Grid-Equations	20
3.2.2 Discretization of Electromagnetic Operators	23
3.2.3 Discretization of Material Properties	26
3.3 Local Mesh Refinement	28
3.3.1 Proposed Algorithm for Mesh Refinement	30

3.3.2	Matrix Operators for Mesh Refinement	32
3.4	Grid Electro-Magnetic Validation	34
3.4.1	Point Charge	35
3.4.2	Multiple Charges	37
3.4.3	Helmholtz Coil	40
3.4.4	Electromotive Force	42
4	EIT Inverse Problem	45
4.1	Reconstruction Algorithms	45
4.2	Isopotential Calculation	47
4.2.1	Electrical Field	48
4.2.2	Möbius Transformation	50
4.3	Input Data	53
4.4	2D Image Reconstruction	54
4.4.1	Results	54
4.4.2	Discussion	62
4.5	3D Image Reconstruction	63
4.5.1	Results	65
4.5.2	Discussion	67
5	Conclusions and Future Developments	69
	Bibliography	76
A	Filtered Backprojection Algorithm	77

List of Tables

- 2.1 Mean Conductivity and Relative Permittivity values for tissues of interest at 1 MHz (required for better tissue characterization - β dispersion). Taken from Hasgall et al. [2014]. 7

- 3.1 Finite integration technique (FIT) Discrete Electromagnetic Quantities 22
- 3.2 Discrete Operators Algebraic Properties. 26
- 3.3 Discrete Operators in grid doublet. 26
- 3.4 Adopted nomenclature for cell resolution in grid. 31

List of Figures

2.1	Cell Electronic Model.	6
2.2	Admittivity dependence on frequency. α , β and γ dispersion. Dashed curves indicate additional, and smaller, relaxation effects. (taken from Schwan [1988])	7
2.3	Domain and boundary regions for the Electrical Impedance Tomography (EIT) problem. Current injection and voltage sensing sites are also depicted. Electrodes marked as red circles.	9
2.4	Electrical impedance computer mammograph (taken from Yusof [2009])	12
2.5	Devices for brain imaging EIT (taken from Yerworth et al. [2003])	12
2.6	Conductivity reconstruction maps in a transversal plane for a biological phantom composed of excised organs (taken from Rosa [2014])	13
2.7	A photograph of the experimental system <i>CardioInspect</i> (modified from Zlochiver et al. [2006])	14
3.1	FIT grid doublet - $\{\mathbf{G}; \tilde{\mathbf{G}}\}$	19
3.2	Cell complex with adopted nomenclature for grid functions.	20
3.3	Discretization of divergence operator.	23
3.4	Sketch Demonstration of Equation 3.28. For example, \hat{e}_x occurs once with a positive and once with a negative sign for the <i>curl</i> summation of fluxes \hat{b}_z and \hat{b}_y	25
3.5	Allocation of metrical information of the <i>Maxwell's-Grid-Equations</i> and grid dimensions in $\{\mathbf{G}, \tilde{\mathbf{G}}\}$. Taken from Clemens and Weiland [2001] with modifications.	27
3.6	Grid refinement structure. a) OcTree top-down approach. b) Multi-linked List	29
3.7	Grid example for EIT simulation. Left) 3D view; Right) Top view.	32
3.8	Low to high resolution interface for 1-forms. a_n , in orange, can be seen as a electromagnetic quantity along the edges of $\tilde{\mathbf{G}}$ (not shown). The virtual neighbor, a , is represented by a red arrow and the coefficients for N_{zy+} (left) and N_{zz+} (right) matrices are given by the formula below the image.	33

3.9	High to low resolution interface for aligned and misaligned 1-forms. Arrow nomenclature is the same as in Figure 3.8 and the coefficients for neighbor matrices are given by the formulas presented.	33
3.10	Left: Low to high neighbor interface for 0-form. Right: High to low neighbor interface for 0-form. Each virtual neighbor is depicted in red and allocated in \mathbf{G} , while a_n , in blue, are allocated in the barycenters of $\tilde{\mathbf{G}}$. Again, the coefficients for neighbor matrices are given by the formula bellow each image.	34
3.11	Phases of Modeling and Simulation and the Role of Validation (taken from Oberkampff and Trucano [2002])	35
3.12	Axial cut ($z = 0\text{m}$) of Electric Field Direction (arrows) and Isopotential Lines for a point charge in a discretized mesh with $L_m = 0.001\text{m}$, $(x, y, z) = (0.025, 0.025, 0.005)\text{ m}$ and centered at the origin. Colorbar normalized to the modulus of applied charge.	36
3.13	Electric scalar potential Φ dependence on distance from a point charge C	37
3.14	Dipole simulation with varying distances between charges with $ C = 1 \cdot 10^{-8}$. Images correspond to an axial cut at $z = 0\text{ m}$ of a mesh with the following characteristics: $L_m = 0.001\text{ m}$; $(x, y, z) = (0.05, 0.05, 0.01)\text{ m}$; $N_c = 25000$. Colorbar in volt.	38
3.15	Axial cut ($z = 0\text{m}$) of electrical dipole with different conductivities paths between charges. Discretized mesh with $L_m = 0.001\text{m}$; $(x, y, z) = (0.05, 0.05, 0.01)\text{ m}$; $N_c = 25000$ and centered at the origin. Colorbar in volt.	39
3.16	Experimental protocol to measure reactance of materials.	39
3.17	Axial cut ($z = 0\text{m}$) of electromagnetic irradiation board. The same material is used in both simulations but with different surface areas. Discretized mesh with $L_m = 0.001\text{m}$; $(x, y, z) = (0.05, 0.05, 0.05)\text{ m}$; $N_c = 125000$ and centered at the origin. Colorbar in volt.	40
3.18	<i>Helmholtz Coil</i> schematic.	41
3.19	Magnetic vector potential of one coil with <i>radius</i> = 0.04m, 5 <i>coil loops</i> and a <i>Current</i> = 1A	42
3.20	<i>Helmholtz Coil</i> with <i>radius</i> = 0.04 m computer model simulation. Discretized mesh with $L_m = 0.002\text{ m}$; $(x, y, z) = (0.1, 0.1, 0.1)\text{ m}$; $N_c = 125000$ and centered at the origin.	42
3.21	<i>e.m.f</i> computer model calculation. Mesh area for sensing coil with $L_m = 0.01\text{ m}$; $(x, y, z) = (0.5, 0.5, 0.5)\text{ m}$; $N_c = 125000$ and centered at sensing coil barycenter.	43

3.22	<i>e.m.f</i> result for 90 degrees angle between coils with increasing discretization of the sensing coil.	44
4.1	Projections through an object and the corresponding coordinate system for x-ray Computed Tomography (CT).	46
4.2	Image reconstruction conducted along the isopotential lines.	47
4.3	Isopotential lines obtained through the electric field calculation. Electrodes position are marked with magenta circles and the colorbar indicates the electrode identification number.	49
4.4	Isopotential lines with opposite method. Electrodes position are marked with magenta circles and the colorbar indicates the electrode identification number.	50
4.5	Möbius transformation. Axis in m	51
4.6	Möbius transformation of isopotential lines.	52
4.7	Isopotential lines calculated with the Möbius transformation method.	53
4.8	Backprojection isopotentials with adjacent electrodes protocol for phantom with an increased conductivity sphere with 0.04 m radius at the center.	55
4.9	Backprojection reconstruction of phantom in Figure 4.8(a) for a system of 16 electrodes with adjacent electrode protocol.	55
4.10	Backprojection reconstruction with increasing number of electrodes.	56
4.11	Backprojection reconstruction with different phantom sizes, placement and geometries. Colorbar in V/V	57
4.12	Backprojection reconstruction of circular phantom with 0.03 m and centered at $(x, y) = (-0.06, 0.06)$ m. Colorbar in V/V	58
4.13	Backprojection reconstruction of multiple conductivity phantoms. (a),(b) and (c) are conductivity maps. (d),(e) and (f) are the reconstruction result. (g),(h) and (j) are single projections in the backprojection algorithm. Colorbar of all Figures in V/V	59
4.14	Normalized plots for one projection of a circular phantom.	59
4.15	Backprojection image reconstruction from a phantom of a thorax.	60
4.16	Filtered Backprojection reconstruction of phantom in Figure 4.15(a).	61
4.17	Spectral analysis of one projection of phantom in Figure 4.15(a).	61
4.18	3D mesh used to construct the thorax model. Axis in m	63
4.19	3D Segmentation from CT-scan. Thorax transverse cut. Axis in m	64
4.20	3D electrodes distribution in the thorax. On the right is a close-up view of one vertical line of electrodes.	66

4.21 3D Backprojection results for thorax impedance imaging. Axis in m	66
A.1 Common filters employed in filtered backprojection method. 1, Ram-Lak; 2, Shepp-Logan; 3, low-pass cosine; and 4, generalized Hamming. Taken from Gabashvili and Snider 2003	78

List of Acronyms

2D

Two-dimensional space

3D

Three-dimensional space

AC

Alternating current

CT

X-ray computed tomography

DC

Direct current

EIT

Electrical impedance tomography

EMF

Electromotive force

FDTD

Finite difference time domain

FEM

Finite element method

FFT

Fast fourier transform

FIT

Finite integration technique

Mk1

Sheffield mark 1 system

MRI

Magnetic resonance imaging

PET

Positron emission tomography

SPECT

Single photon emission computed tomography (SPECT)

List of symbols

\mathbf{Z}	Bioimpedance	$[\Omega]$
\mathbf{V}	Electric Voltage	$[\text{V}]$
\mathbf{I}	Electric Current	$[\text{A}]$
Y	Complex Admittance	$[\text{S}]$
G	Conductance	$[\text{S}]$
B	Susceptance	$[\text{S}]$
γ	Complex Admittivity	$[\text{S}/\text{m}]$
σ	Electric Conductivity	$[\text{S}/\text{m}]$
ϵ	Dielectric Permittivity	$[\text{F}/\text{m}]$
ϵ_r	Relative Permittivity	$[-]$
μ	Magnetic Permeability	$[\text{H}/\text{m}]$
ρ	Electric Charge Density	$[\text{C}/\text{m}^3]$
w	Angular Frequency	$[\text{rad}/\text{s}]$
χ	Electric Susceptibility	$[-]$
χ_m	Magnetic Susceptibility	$[-]$
ϵ_0	Vacuum Permittivity	$[\text{F}/\text{m}]$
μ_0	Vacuum Permeability	$[\text{H}/\text{m}]$
$\delta\Omega$	Problem Boundary	$[-]$
Ω	Problem Domain	$[-]$
\vec{D}	Dielectric Flux Density	$[\text{C}/\text{m}^2]$
\vec{B}	Magnetic Flux Density	$[\text{Wb}/\text{m}^2]$
\vec{E}	Electric Field	$[\text{V}/\text{m}]$
\vec{H}	Magnetic Field Intensity	$[\text{A}/\text{m}^2]$
\vec{J}	Current Density	$[\text{A}/(\text{s}\cdot\text{m})]$
\vec{J}_m	Magnetic Current Density	$[\text{A}/(\text{s}\cdot\text{m})]$

\vec{J}_e	Electric Current Density	[A/(s·m)]
\vec{J}_p	Polarization Current Density	[A/(s·m)]
\vec{A}	Magnetic Vector Potential	[(V·s)/m]
\vec{P}	Dielectric Polarization	[C/m ²]
\vec{M}	Magnetization Vector	[A/m]
G	Main grid	[–]
$\tilde{\mathbf{G}}$	Dual grid	[–]
V_N	Cell volume	[–]
N_c	Total number of cells	[–]
$curl$	Discrete curl operator in the main grid	[–]
\widetilde{curl}	Discrete curl operator in the dual grid	[–]
div	Discrete divergence operator in the main grid	[–]
\widetilde{div}	Discrete divergence operator in the dual grid	[–]
$grad$	Discrete gradient operator in the main grid	[–]
\widetilde{grad}	Discrete gradient operator in the dual grid	[–]
\hat{e}	Electric grid voltage	[V/m]
\hat{h}	Magnetic grid voltage	[A/m]
\hat{b}	Magnetic grid facet flux	[Wb/m ²]
\hat{d}	Dielectric grid facet flux	[C/m ²]
\hat{j}	Current grid facet flux	[A/m ²]
\hat{j}_e	Electric current grid facet flux	[A/m ²]
\hat{j}_m	Magnetization current grid facet flux	[A/m ²]
\hat{j}_p	Polarization current grid facet flux	[A/m ²]
\hat{p}	Polarization grid facet flux	[C/m ²]
\hat{m}	Magnetization grid voltage	[A/m]
\hat{a}	Magnetization vector grid potential	[(A·s)/m]
q	Charge distribution	[C/m ³]
Φ	Electrical scalar potential	[V]
M_ϵ	Constitutive Material Matrix for Permittivities	[F/m]
M_ν	Constitutive Material Matrix for Reluctivities	[m/H]
M_σ	Constitutive Material Matrix for Conductivities	[S/m]

Chapter 1

Introduction

1.1 Motivation and Objectives

Medical imaging, as a scientific research field that constitutes a discipline in biomedical engineering, refers to a large set of noninvasive technologies used to “view” the human body in order to study or treat medical conditions. In this bounded definition, medical imaging can be seen as the solution of mathematical inverse problems where properties of living tissues are inferred from the observed signal. As an example, in CT the different radiation absorption rates are used to distinguish different tissues within the body. Despite these imaging techniques being considered noninvasive, in the sense that no instrument is introduced inside the patient’s body, there is still the issue of cell damage due to the use of ionizing radiation when these ions interact with molecules, breaking them into smaller fragments, or themselves take part in chemical reactions, spreading the damage.

Because each of the existing medical tomographic technologies, providing different information in a 2D cross-section view of the body being imaged, consist in a way to measure the interaction of different radiation types with the body in analysis one must first comprehend the underlying physical phenomenon in order to understand and correctly interpret the obtained measurements. And so, a model that mimics these interactions must be formulated and extensively studied for a better insight of all phenomena between the source and the sensing system.

Current tomographic techniques, like CT, Magnetic Resonance Imaging (MRI) and Positron Emission Tomography (PET), consists in very expensive, huge and bulky system in a fixed place at the hospital that are not likely to be implemented in surgical scenarios or used in patients in intensive care units. For these reasons a safe, low-cost, portable, and easy to use bedside system is needed for versatile clinical diagnosis. Since EIT has the capability to fulfill all these

specifications, but is still in the early stage of development and with a lot of studies to be made regarding its efficiency and effectiveness, the author was allured to take part in this investigation effort.

The objectives of the present thesis were set at the beginning and consisted in the development of an electromagnetic grid for numerical simulations of the forward problem and the implementation of a linear method to solve the inverse problem and retrieve information of the impedance map distribution in a thorax.

The forward problem, mainly intended for the implementation of a model that simulates the electromagnetic interaction with a body with known physical characteristics when a radiation is applied to it, was first validated with a set of exercises, whose results are known, in order to have certainty that the data obtained with the forward problem was consistent with the physical properties of the tissues.

The method based in the backprojection algorithm to solve the inverse problem was chosen for two main reasons. Because of this model previous allocation of the electrode-pixel pair in the image there is capability of real-time imaging of the thorax. And secondly, if non-linear iterative methods are necessary for better estimation of the body tissues the backprojection algorithm serves as a very close first approximation while, theoretically, contributing to the decrease of overall inverse problem iterations.

This master's thesis, despite very demanding considering the amount of work to be done, was above all a very interesting venture due the the dispersion of disciplines to be enrolled and the possibility of contacting and being part of a multidisciplinary team focused on developing new and groundbreaking technologies.

1.2 Organization of the Thesis

This thesis is divided in two main components: the forward problem modulation and solving the inverse problem.

Before the forward problem is tackled, a brief explanation on the biomaterials electrical properties is given (Chapter 2) followed by a set of typical systems employed in imaging technologies, along with their operating principles and state of the art.

In Chapter 3 Maxwell's equations are presented, with no original mathematics, and the details of the finite integration technique applied in the discretized space to solve the direct problem are described. In the end a set of simple simulations are presented to validate the grid electromagnetic properties.

Chapter 4 deals with the backprojection reconstruction algorithm, in 2D and 3D, with special

attention being given for the isopotential lines construction. For this purpose, two methods are explored: (1) through calculation of the electrical field and its Jacobian; (2) using a Möbius space transformation.

In the last chapter, and regarding the overall thesis, the final conclusions are made and a final Section for further work containing ideas about intended future developments is presented.

Chapter 2

Context and State of the Art

This chapter aims to expose some concepts, and associated state of the art, of methods relying on bioimpedance measurements and the imaging techniques based on the Electrical Impedance Tomography. For this purpose, the chapter begins with the introduction of dielectric properties applied to biomaterials and their mathematical relationships, being complemented with relevant biophysical mechanisms that model the electromagnetic behavior on tissues. Finally, an exhaustive study of state of the art for the Electrical Impedance Tomography technique is presented, with the main focus on biomedical applications to obtain thorax impedance maps.

2.1 Bioimpedance

2.1.1 Definition

Bioimpedance, denoted by \mathbf{Z} , is one of the major electrical properties of tissues. While bioelectricity is the ability of a tissue to generate electricity, bioimpedance refers to the electrical properties of biological tissues, and their geometrical properties, measured when external current flows through them.

The two main and basic properties in bioimpedance are resistance and capacitance, being resistance the measure of the level to which a tissue opposes the flow of ions among its cells (and is related by the Ohm's Law (Equation 2.1) to current, denoted by \mathbf{I} , and voltage, \mathbf{V}) and capacitance the property of an electric conductor that is measured by the amount of electric charge separation that can be stored and released in the form of electrical potential.

$$\mathbf{Z} = \frac{\mathbf{V}}{\mathbf{I}} = \frac{|V|e^{j\theta_v}}{|I|e^{j\theta_i}} \quad (2.1)$$

The dielectric properties of a biological tissue results from the interaction of electromagnetic

radiation with its constituents at the cellular and molecular level. In fact, cells may be modeled as simple group of electronic components, Figure 2.1, where the extracellular space is represented by a resistor (**Re**), and the intracellular space and the membrane being modeled by a resistor (**Ri**) and a capacitor (**Ci**).

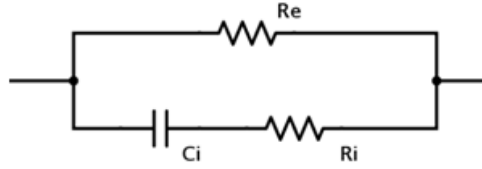


Figure 2.1: Cell Electronic Model.

Because of this model rough prediction of biological tissue behavior the present thesis adopts a more generic quantity, complex admittance, to model the behavior of a material under the influence of external electromagnetic radiation,

$$Y = \frac{1}{\mathbf{Z}} = G + jB = \frac{A}{d}\gamma = \frac{A}{d}(\sigma + jw\epsilon) \quad (2.2)$$

where Y is the complex admittance, G is the conductance, B the susceptance. The complex admittivity, electric conductivity and dielectric permittivity are represented by γ , σ and ϵ respectively. Finally, A/d is a scaling factor to separate geometrical properties from the constitutive ones and w the angular frequency.

Considering Equation 2.2, materials with small conductivity inhibit DC current and on the other hand conductive materials (or with high σ) allow both DC and AC current to flow inside the tissue. Using the same analogy for ϵ , materials with high permittivity will enhance AC current over DC current and so facilitating the proliferation of electromagnetic radiation inside the tissue. In physical terms, one can look at conductivity of a material as a measure of the capability of its charge to be transported throughout the volume when an external electric field is applied, and its permittivity as a measure of the capability of its dipoles to rotate or its charge to be stored by an applied external field.

Whenever A/d is kept constant and the electrodes position remains unaltered, the only changes between impedance measurements are due to changes of target tissue position (r) and angular frequency (w) in complex admittivity:

$$\gamma(r, w) = \sigma(r, w) + jw\epsilon(r, w) \quad (2.3)$$

If the tissue under analysis is considered to be isotropic, a simplification commonly found in bioimpedance studies, the dependence on r falls and so $\gamma(r, w) = \gamma(w)$.

This admittivity dependence on frequency was subject of extensive study over the years, in which is highlighted the work done by Schwan [1988] on the relative permittivity decrease at high frequencies variations in three main steps. These non-linear variations of admittivity with frequency, called dispersions, are found:

- At 10^9 Hz the γ dispersion is due to the polarization of water molecules.
- The β dispersion, in the 10^4 Hz region, is due mainly to the polarization of cellular membranes (like barriers to the flow of ions).
- The low frequency α dispersion is associated with ionic diffusion processes in cellular membrane.

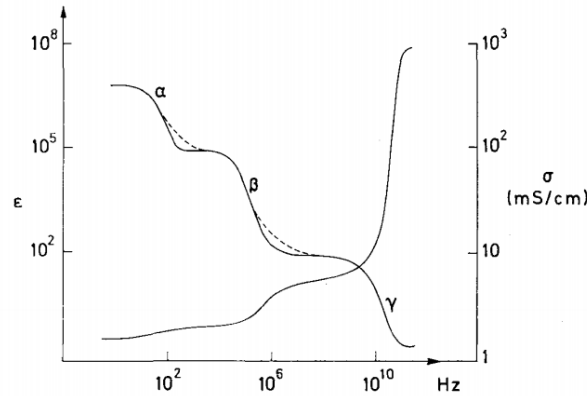


Figure 2.2: Admittivity dependence on frequency. α , β and γ dispersion. Dashed curves indicate additional, and smaller, relaxation effects. (taken from Schwan [1988])

With this diverse information about the internal constituents of the body (cell size and orientation or membrane thickness or water content) there is a great deal of information contained in a bioimpedance map of the body. As such, changes in this map imply a physiological or pathological change that can be monitored and measured.

Table 2.1: Mean Conductivity and Relative Permittivity values for tissues of interest at 1 MHz (required for better tissue characterization - β dispersion). Taken from Hasgall et al. [2014].

	σ (S/m)	ϵ_r
Heart	$3.28 \cdot 10^{-1}$	$1.97 \cdot 10^3$
Blood	$8.22 \cdot 10^{-1}$	$3.03 \cdot 10^3$
Lung	$1.36 \cdot 10^{-1}$	$7.33 \cdot 10^3$
Liver	$1.87 \cdot 10^{-1}$	$1.54 \cdot 10^3$
Subcutaneous Fat	$4.41 \cdot 10^{-2}$	$5.08 \cdot 10^1$
Bone	$2.44 \cdot 10^{-2}$	$1.45 \cdot 10^2$
Muscle	$5.03 \cdot 10^{-1}$	$1.84 \cdot 10^3$

Besides conductivity and permittivity there is another physical property in this model that lacks mentioning. The magnetic permeability (μ) is the degree of magnetization of a material

in presence of an applied magnetic field. Materials with high permeabilities allow magnetic flux through more easily than others. Because body tissue, like air, does not have any noticeable effect on a magnetic field, the magnetic permeability inside biological tissues is going to be considered equal to that in a vacuum.

2.1.2 State of the Art

The acquisition of anatomical and functional information about structures within the body is very important for the proper treatment of all disorders. For this reason the electrical properties of biological tissues have been of interest for over a century. And, as previously stated, since the electric properties of tissues are correlated with the cell fluids, membranes and ultimately the cell structure and its components, any change to the basal measure of electrical scalar potential distribution and pathways of current flow through the body can be assigned to a change in impedance due to a pathology or functional change in the body.

There are some applications, like therapeutic tools to laboratory analysis and hazard detection, that work based on measure of samples bioimpedance. For instance Lu et al. [2013] developed an electrical bioimpedance spectroscopy-based multi-electrode culture monitoring system to characterize cell growth; Alberto Yufera and Canete [2011] proposed some alternative methods for measuring and identifying cells involved in a variety of experiments, including cell cultures; Das et al. [2014] advanced with an analysis technique to extract the electrical properties of a single cell with impedance spectroscopy data from a group of cells in suspension; Halter et al. [2011], distinguished between benign and malignant formations; Siriopol et al. [2013] predicted mortality in haemodialysis patients by combining pre and post dialysis lung ultrasound and total body impedance;

There are now over 20 years that Weinhold et al. [1993] used thoracic electrical bioimpedance measures for early diagnosis of rejection in thirty-five transplant recipients. These patients were monitored and, with a sensitivity diagnostic parameter of 71%, was concluded that it was a quick and noninvasive monitoring technique which could be used in the outpatient clinic as a great supplement to invasive biopsies.

More recent studies have also contributed to the certification of bioimpedance measures as a great, quick and noninvasive method for monitoring of respiratory and cardiac function. Reviews like A Moshkovitz et al. [2004], highlighted significant progress in cardiac output determination by bioimpedance because of newer algorithms that used thoracic and whole body bioimpedance with better correlation with invasive cardiac output determination. A later study by Landaeta et al. [2006] proposed a user-friendly heart rate monitoring system for a standing

subject, insensitive to the movement of electrodes.

Limitations apart, real-time monitoring of organ function and tissue composition by means of non-invasive bioimpedance method has the advantage of providing routine and harmless examination while the patient incurs in every-day activities when comparing to other current technologies for the same examinations.

2.2 Electrical Impedance Tomography

2.2.1 Definition

EIT can be seen as an application of the bioimpedance method, that has been for the past decades studied and applied to a wide range of devices, in the biomedical field. EIT is a non-invasive imaging technique that involves the formation of 2D images or 3D volumes from a map of the internal admittivity distribution obtained from voltage measurements made at the boundary ($\delta\Omega$) of the body (Ω) under analysis.

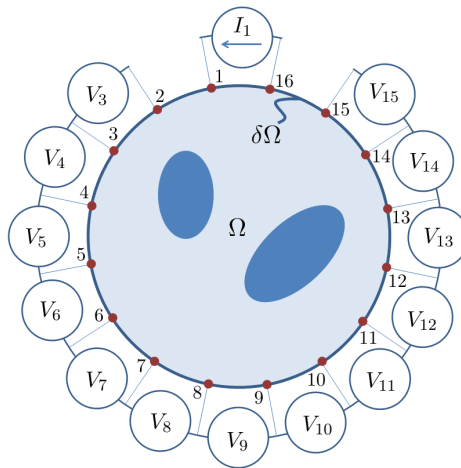


Figure 2.3: Domain and boundary regions for the EIT problem. Current injection and voltage sensing sites are also depicted. Electrodes marked as red circles.

Under the conditions above stated, EIT may be regarded as the inverse problem to determine the admittivity inside Ω . Besides ill-posed, because the system is under-determined due to the higher number of variables that must be estimated when compared the independent data points in the EIT acquisition protocol, the problem of determining the impedance inside the body is also non-linear. This non-linearity arises from the full set off unknown variables.

To perform an EIT a four-electrode method is used. In this method a set of electrodes is placed in the $\delta\Omega$ boundary with respect to the Ω region under investigation. According to Holder [2005], a small amplitude current (1-5 mA that flows inside Ω) with a fixed frequency is applied in a set of electrodes, henceforth known as drive pair, and the electrical potential at the

other electrodes position is recorded in a differential way between adjacent electrodes, known as receiver pairs. It must be emphasized that the drive pair electrodes are not exclusively adjacent. This process is repeated for different drive and receiver pairs to complete a frame acquisition. For a high independent number of measurements at the disposal of the reconstruction there must be a high number of these drive and receiver pairs in each frame.

Regarding the applied current there are a couple of important criteria that must be met. Because the current must intrude several layers of different tissues between electrodes there must be a compromise in the intensity/power of the applied current in order to accomplish the goal stated before and to have a current that is harmless and inoffensive to the tissues themselves. With that in mind, and recalling the tissues response to AC current in *Section 2.1*, a small amplitude with a frequency between the α and β dispersion region is able to give a good contrast between structures and liquids inside and outside the cells as their membranes allow alternating current to flow.

However, EIT is hindered by difficulties in interpreting the resulting images because of the simple shapes (circles, ellipses, and so forth) that are obtained in the reconstruction process. The mismatch between the true body shape and the one used for reconstruction is known to introduce errors, and has been properly characterized by Grychtol et al. [2012]. Other issue that interfere on EIT becoming a daily used imaging device is the computational burden on solving a ill-posed problem and the consequences of dealing with non-linear imaging techniques. Other issues of both the ill-conditioning and ill-posed nature of EIT that contribute to the already intricate mathematical formulation of EIT will be described in detail in the subsequent chapters.

2.2.2 State of the Art

EIT systems can be seen in application throughout hospital departments like Cardiology, Gastroenterology, and Tumor diseases due to the difference in admittivity recorded between tissues. Most EIT systems developed so far apply a small alternating current at a single frequency, however there are already some EIT devices that apply several frequencies to better differentiate tissues within the same organ.

The first images that appear to be made using bioimpedance information are attributed to Henderson and Webster [1978]. An impedance camera, using a rectangular array of 100 electrodes, was built to generate impedance maps of the thorax at rates up to 32 frames per second.

Even though Benabid et al. [1978] proposed a system for brain impedance tomography

made of a set of 128 electrodes, surrounded by an electrode guarding to make the electric field uniform and to enable a focused measure of the impedance by each electrode, the first system commercially available for clinical practice was the Sheffield Mark 1 - Mk1 - by Brown and Seagar [1987]. In the Mk1 system 16 electrodes are placed, equidistantly, in the $\delta\Omega$ boundary. A 50 kHz current is ejected between adjacent electrodes, in what is known as the *Sheffield Protocol*, and then the potential difference is measured in all the other remaining adjacent electrodes. The reconstruction of the 2D image from the data obtained was conducted along the equipotential lines according to the simple linear backprojection algorithm. More detailed explanation about this method is given at *Section 4.2*.

It was after the Mk1 launch that EIT received an increased attention within the scientific community, leading to a wide range of applications, that even included neonatal brain imaging proposed by Murphy et al. [1987] for the study of cerebral haemodynamic. In fact, and according to Holder [2005], in the mid to late 1980's about a dozen groups have developed their own system and reconstruction software and by the mid 1990's a study by Teschner and Imhoff [2011] concluded that more than 30 research groups were actively engaged in EIT related research with main objectives areas like imaging of lung ventilation, cardiac function, gastric emptying, brain function and pathology, and screening for breast cancer.

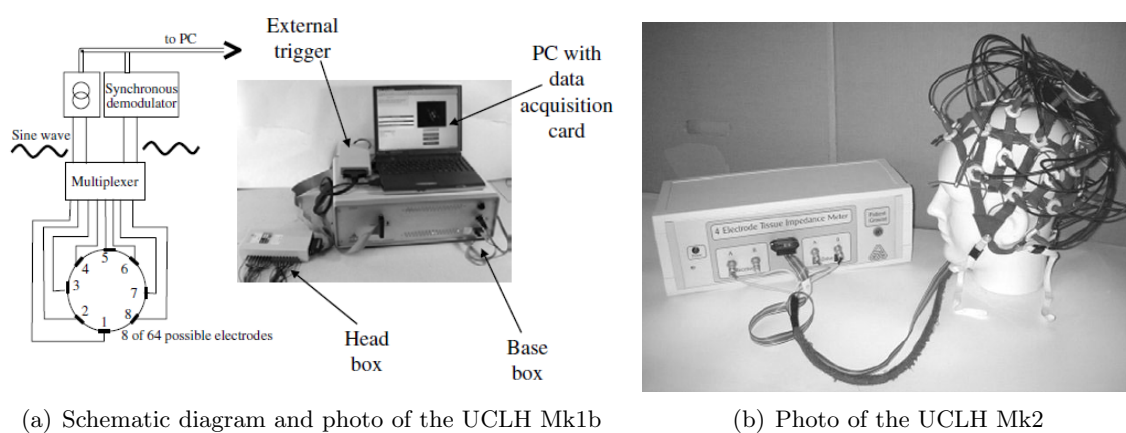
In the breast cancer screening using EIT, in which the principle that tissues have different electrical properties depending on their cell structure and pathology is used, a dual-frequency electrical impedance mammography for the diagnosis of non-malignant breast disease in 166 woman was used. Trokhanova et al. [2008] concluded that this technique enables one not only a diagnose of mastopathy but also allows accurate detection of its cystless form. In a technology review, Yusof [2009] assessed the effectiveness, safety and cost-effectiveness of EIT in the screening of breast cancer having determined that early symptoms of the mammary gland pathology were detected despite an inaccurate modeling of the regionally varying electrode-skin contact impedance and poor signal-to-noise ratio.

In EIT applications associated with the gastrointestinal tract this technique is used to detect alterations in admittivity within thick slices of body tissues. This principle is used by Podczeck et al. [2007] to monitor the movement of luminal materials through different compartments of the gastrointestinal tract in order to study normal physiology, and the effects of transit modifying substances used in the treatment of gut transit disorders. Despite the use of EIT to monitor luminal materials movement, there are other applications that can be found in the literature like patients with gastroesophageal reflux symptoms management using combined multichannel intraluminal impedance and pH, depicted by Jodorkovsky et al. [2014].



Figure 2.4: Electrical impedance computer mammograph (taken from Yusof [2009])

For the brain imaging EIT a portable and non-ionizing imaging system, which is suitable for long term monitoring or surgery planning, is provided. Systems based in the Mk1 design were developed to image visual evoked potentials in humans (Tidswell et al. [2001]) and preliminary data have been gathered during seizures (Tidswell et al. [2003]). Other systems, like the UCLH Mk1b (a system that operates at a single frequency, selectable from 18 frequencies between 225 Hz and 77 kHz) and UCLH Mk2 (designed to apply all the frequencies simultaneously to avoid temporal sampling errors due to impedance changes associated with the cardiac and respiratory cycles), were developed by Yerworth et al. [2003] for multiple frequency current application.



(a) Schematic diagram and photo of the UCLH Mk1b

(b) Photo of the UCLH Mk2

Figure 2.5: Devices for brain imaging EIT (taken from Yerworth et al. [2003])

Other potential application to EIT is the monitoring of bladder volume in 3D. In this field a publication by Leonhardt et al. [2011], where a pre-commercial EIT system was tested in preliminary lower torso impedance measurements of paraplegic patients, obtained a good cor-

relation between bladder volume and EIT measurements. The first portable and autonomous bioimpedance device for bladder volume-tracking is thoroughly described by Rosa [2014] for differential tissue imaging by means of simultaneous multi-tone signal injection and using the principles of EIT.

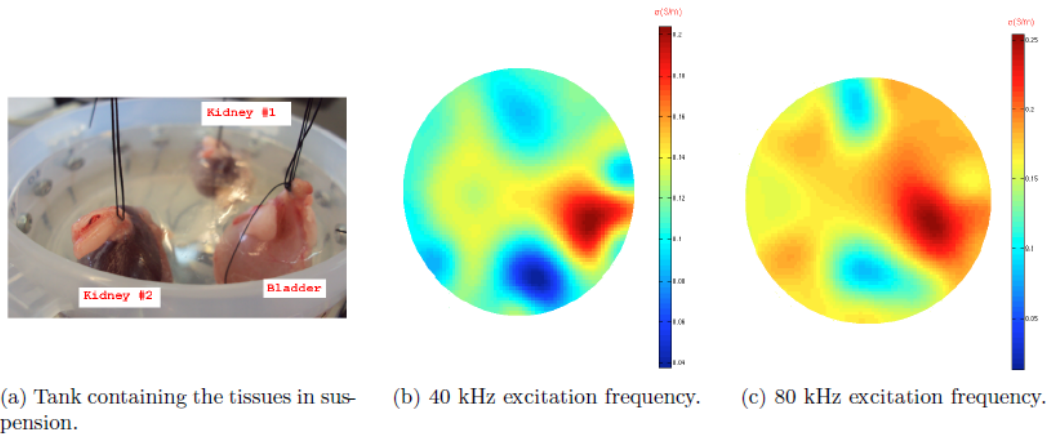


Figure 2.6: Conductivity reconstruction maps in a transversal plane for a biological phantom composed of excised organs (taken from Rosa [2014])

Finally, the acquisition of anatomical and functional information within the chest is very important for the proper treatment of cardiac, circulatory and ventilatory disorders. Given the variation of electrical impedance within the thorax (strongly related to cardiac and ventilatory events) the EIT takes natural place in the hospital environment for these thorax data acquisition. In the case of the lungs, tissue impedance varies with the air content. Thus ventilation and changes of end-expiratory lung volume results in changes of the voltages measured by electrodes at the body surface.

In order to accredit EIT in the current medical environment, some studies involving the correlation of results between EIT and well-established imaging devices are found in literature on both animal and human models.

Involving animal models, for example, a study by Frerichs et al. [2002], where EIT is compared with CT to detect regional changes in lung volume in healthy lung animal models, demonstrated a good correlation between the two methods. Later, Hinz et al. [2003] used animals to validate the use of EIT for measuring regional ventilation distribution by comparing it with Single Photon Emission CT (SPECT) scanning. More recently, Richard et al. [2009] compared EIT with PET in order to quantify the changes in regional ventilation secondary changes in ventilator parameters, obtaining in both models an excellent correlation.

In human testing it has been proven, by Eyuboglu et al. [1987], the possibility to perform

cardiosynchronous averaging and produce dynamic impedance images describing different times in the cardiac cycle. Later, Hoetink et al. [2002] reconstructed sources of a cardiac-related electrical impedance waveform using data from thoracic surface measurements, which corresponded well with MRI measurements of surface area changes of the thoracic organs during the cardiac cycle. More recently, Proença et al. [2014] studied the influence of heart motion on EIT-based stroke volume estimation having obtained an EIT-based total ventricular volume estimation error of -10.1 ± 15.7 ml and considered sufficiently low to be clinically useful in normal subjects. All these studies showed that, despite EIT signals being affected by myocardial motion, the results obtained are not compromised, and so, may be useful and used in clinical environment.

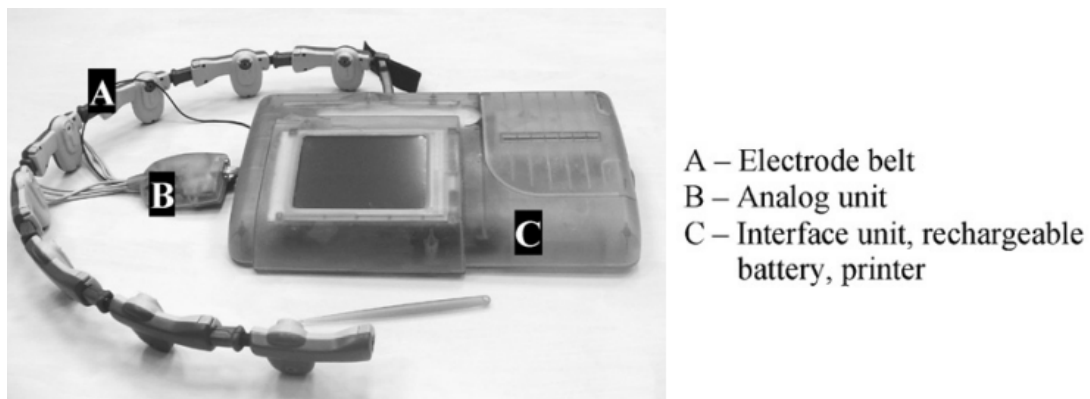


Figure 2.7: A photograph of the experimental system *CardioInspect* (modified from Zlochiver et al. [2006])

Regarding thorax imaging and pathology diagnosis, recent breakthroughs in the detection of pneumothorax (due to the presence of low-conducting air) and hemothorax (due to the presence of high-conducting liquids) were made by Hahn et al. [2006] using a system of 16 electrodes with a 50 kHz and 2.5 mA injection current placed around the thorax. At the same time, Zlochiver et al. [2006] developed a portable, and intended for home use, bio-impedance system for monitoring pulmonary edema. The system comprises an 8-electrode belt adjustable to different thorax sizes and injects currents with 3 mA of amplitude and frequency of 20 kHz sequentially to the body in an opposite configuration while voltages are recorded by the tetrapolar method to be used in a Newton-Raphson algorithm for image reconstruction.

The failure to adopt EIT as a viable clinical tool today is closely related to the experience of those who had tried to use it in the clinical setting. At this point, and after almost 30 years of existence, EIT has still not found a natural place in clinical practice, even though the results of all experimental studies suggests the tremendous potential clinical benefits of EIT.

Chapter 3

EIT Forward Problem

This chapter will describe Maxwell's equations that govern physical phenomena and their application in the area of medical imaging. For the application of these equations and their physical entities was adopted the harmonic regime for temporal schemes and resorted to the finite integration method for simulation of the discrete space. After discretization of Maxwell's equations and respective electromagnetic properties of the materials matrices, and in order to reduce computational complexity, an algorithm for local grid refining is proposed and the correct adjustments to the electromagnetic operators is explained. In the end, and to assess the correct functioning of the discretized simulation space, a set of exercises covering all physical quantities involved by Maxwell's equations were implemented.

3.1 Maxwell's Equations

James Clerk Maxwell developed the classical electromagnetic theory mainly in “A Dynamical Theory of the Electromagnetic Field” – one of the most important compilation of previous unrelated experimental observations and scattered laws by Charles-Augustin de Coulomb, Carl Friedrich Gauss, Jean-Baptiste Biot, Félix Savart, André-Marie Ampère, and Michael Faraday. Maxwell extended previous experiments by the introduction of the notion of “*Electromagnetic Momentum of a Current*” or Displacement Current and Field to postulate a set of partial differential equations applicable to all macroscopic electromagnetic phenomena.

After some reformulation by Oliver Heaviside and the development of more powerful mathematical descriptions of the electromagnetic field, that enable the equations to take a more simpler form, the famous four Maxwell's equations that describe electromagnetic phenomena in the presence of materials are thus presented in Equation 3.1 both for differential and integral

forms:

$$\nabla \cdot \vec{D} = \rho \quad \Leftrightarrow \quad \oiint_{\delta\Omega} \vec{D} \cdot d\vec{S} = \iiint_{\Omega} \rho dV \quad (3.1a)$$

$$\nabla \cdot \vec{B} = 0 \quad \Leftrightarrow \quad \oiint_{\delta\Omega} \vec{B} \cdot d\vec{S} = 0 \quad (3.1b)$$

$$\nabla \times \vec{E} = -\frac{d\vec{B}}{dt} \quad \Leftrightarrow \quad \oint_{\delta\Omega} \vec{E} \cdot d\vec{\ell} = -\frac{d}{dt} \oiint_{\Sigma} \vec{B} \cdot d\vec{S} \quad (3.1c)$$

$$\nabla \times \vec{H} = \vec{J} + \frac{d\vec{D}}{dt} \quad \Leftrightarrow \quad \oint_{\delta\Omega} \vec{H} \cdot d\vec{\ell} = \oiint_{\Sigma} (\vec{J} + \frac{d\vec{D}}{dt}) \cdot d\vec{S} \quad (3.1d)$$

The electromagnetic quantities are established by Maxwell's equations as being the dielectric flux density (\vec{D}), the magnetic flux density (\vec{B}), the electric field intensity (\vec{E}) and the magnetic field intensity (\vec{H}). But these equations can not describe all physical problems unless the equations that specify the response of free and bound charge and current to the applied fields (named constitutive relations) are known.

For simple media, which is linear, isotropic and homogeneous, these constitutive equations are given by:

$$\vec{D} = \epsilon \vec{E} \quad (3.2a)$$

$$\vec{B} = \mu \vec{H} \quad (3.2b)$$

where ϵ is related to the electric susceptibility of the material (χ) according to $\epsilon = \epsilon_0(1 + \chi)$ and μ is related to the magnetic susceptibility of the material (χ_m) considering $\mu = \mu_0(1 + \chi_m)$. With these entities two new electromagnetic quantities can be derived:

$$\vec{P} = \epsilon_0 \chi \vec{E} \quad (3.3a)$$

$$\vec{M} = \chi_m \vec{H} \quad (3.3b)$$

In Equation 3.3a \vec{P} is the vector field that expresses the density of permanent or induced electric dipole moments in a dielectric material, and in Equation 3.3b \vec{M} is the vector field that expresses the density of permanent or induced magnetic dipole moments in a magnetic material.

Even though these constitutive relations are commonly used they only approximate the real-world scenario (inhomogeneous, anisotropic and non-linear) and depending on the necessary level of detail and scrutiny of the problem these relations may be written assuming ϵ and μ as functions of \vec{E} , \vec{B} , position and time, and are tensorial in nature.

Equation 3.1a is *Gauss' law for electric fields* or also known as *Gauss' flux theorem* and

relates electric flux (number of electric field lines) crossing a closed surface $\delta\Omega$ with the total electric charge enclosed in Ω . The main idea of *Gauss' flux theorem* in differential form is that electric field produced by electric charge diverges from positive charge and converges upon negative charge.

Equation 3.1b is *Gauss's law for magnetic fields*. The key difference between the electric field and magnetic field version of *Gauss's law* result in the natural behavior of magnetic flux and on the divergence of magnetic field. While in *Gauss' law for electric fields* opposite electric charges may be isolated from one another, in *Gauss's law for magnetic fields* magnetic poles always occur in pairs. And so, the divergence of \vec{B} comes equal to zero. The differential form of Equation 3.1b simple states that the divergence of magnetic field is zero at any point.

Equation 3.1c is the extended form of *Faraday's law* or *Maxwell-Faraday's law of induction*. This law states that a time-varying magnetic flux through a surface Σ induces an electromotive force (EMF) in any boundary path $\delta\Omega$ of Σ in the direction as to oppose the change in flux. Likewise, a changing magnetic field induces a circulating electric field.

At last, Equation 3.1d is an extension of *Ampere's law* to time-dependent conditions or, as it is commonly known, *Ampere-Maxwell's law*. This equation refers that the sum of all current sources \vec{J} (Equation 3.4), through a surface, produces a circulating magnetic field around any path that bounds that surface.

$$\vec{J} = \vec{J}_m + \vec{J}_e + \vec{J}_p \quad (3.4)$$

where \vec{J}_m , \vec{J}_e and \vec{J}_p are electric current sources of magnetic, electric and polarization nature respectively.

After setting Maxwell's Equations one lacks only, and for completeness, to associate them a continuity equation that extends far beyond the electromagnetic theory and, as a fundamental law of nature, must be fulfilled at any time.

The first step, in the derivation of the continuity equation, relies in a vector identity that is always true. Which states that the divergence of the curl of any vector field is always zero:

$$\nabla \cdot (\nabla \times \vec{H}) = 0 \quad (3.5)$$

Applying the divergence operator to the Equation 3.1d and having in consideration Equation 3.5 one obtains:

$$\nabla \cdot (\nabla \times \vec{H}) = \nabla \cdot \left(\vec{J} + \frac{d\vec{D}}{dt} \right) = 0 \quad (3.6a)$$

$$\nabla \cdot \vec{J} = -\frac{d(\nabla \cdot \vec{D})}{dt} \quad (3.6b)$$

To reach the final expression of the continuity equation Equation 3.1a must be applied to Equation 3.6b:

$$\nabla \cdot \vec{J} = -\frac{d\rho}{dt} \quad (3.7)$$

This equation, that expresses (local) charge conservation, states that if there is a net electric current flowing in/out of a volume, then the charge within that volume must be increasing/decreasing in order to prevent the appearance/disappearance of spontaneous charge that disturbs the electromagnetic systems dynamics.

3.2 Finite Integration Technique

FIT is a spacial discretization scheme, convenient for computers, that serve as a constitutive basis to express differential equations. This technique, employed throughout physical domains, comes as a natural numerical implementation of Maxwell's Equations (Section 3.1) in both time and frequency domain that preserves basic topological properties of continuous equations such as conservation of charge and energy. This technique, first introduced by Weiland [1977], has been enhanced and applied to solve electromagnetic field problems over the years. This method stands out because of its flexibility in geometrical modeling of the domain of simulation with a limited number of regular-shaped cells that can handle curved boundaries and complex shapes (in Babic and Akyel [2005] and Haber and Ascher [2001]).

With proven numerical efficiency and solidity (Clemens and Weiland [2001]), FIT generates exact algebraic analogues to Maxwell's equations, which guarantee that physical properties of fields are maintained in the discrete space, and lead to a unique solution (Munteanu and Weiland [2007]).

According to Clemens and Weiland [2001] a set of steps are defined for the correct discretization of the problem:

1. Restriction of the electromagnetic problem, that usually represents an open boundary problem, to a simply connected and bounded space domain of the region of interest.
2. Decomposition of the computational domain into a finite number of disjoint cells, i.e. the intersection of two different cells is either empty or it must be a two-dimensional polygon, a one-dimensional edge shared by both cells or a point.

This decomposition defines the main grid \mathbf{G} , and a dual grid $\tilde{\mathbf{G}}$ (see Figure 3.1(a)) is also defined under the premise that barycenters of cubes in grid \mathbf{G} form vertices of cubes in grid $\tilde{\mathbf{G}}$ according to Figure 3.1(a). This brick-shaped decomposition is given by a tensor product

grid, in the cartesian space, defined by Equation 3.8 where the nodes (x_i, y_j, z_k) are enumerated with the coordinates i, j and k along the x -, y - and z -axis, and the allocation of potentials, voltages and fluxes are on cell barycenters, edges and surfaces according to Figure 3.1(b).

$$\mathbf{G} := \{V_{i,j,k} \in R^3 | V_{i,j,k} := [x_i, x_{i+1}] \times [y_i, y_{i+1}] \times [z_i, z_{i+1}]\} \quad (3.8)$$

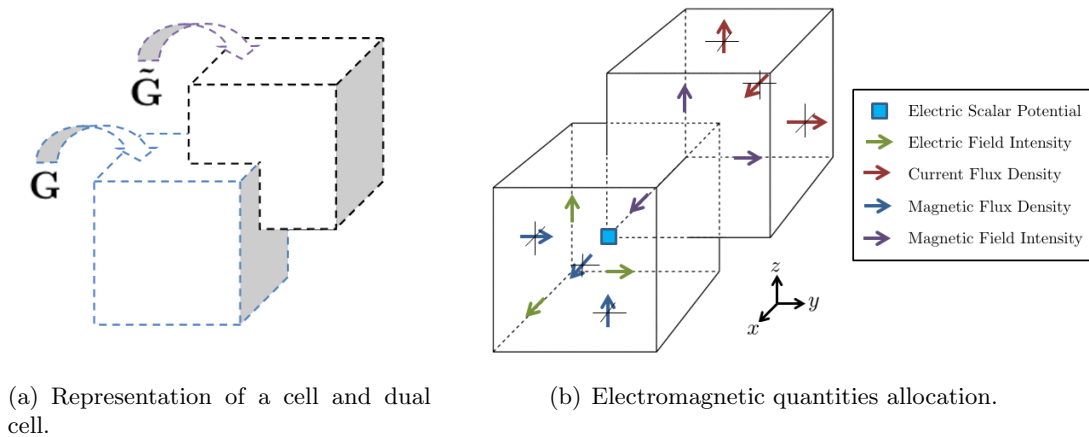


Figure 3.1: FIT grid doublet - $\{\mathbf{G}; \tilde{\mathbf{G}}\}$

Maxwell's equations and related material equations are transformed from continuous to discrete space in Section 3.2.1 and Section 3.2.3 respectively.

Besides FIT, there are two other differential equation methods worth mentioning. The Finite element method (FEM), a numerical technique to obtain approximate solutions to boundary problems, and the Finite difference time domain (FDTD), a method that approximates both spatial and temporal derivatives of Maxwell's equations by finite-difference expressions.

Comparing with FEM, both FDTD and FIT present similar advantages: simpler implementation, and possibility of implementing the problem in an efficient parallel computing model; and disadvantages: staircase approximation when modeling complex and non-orthogonal structures with a cartesian mesh.

FDTD, like FIT, requires a bounded computational domain and the specification of the material properties of each cell within the domain. The main difference is in the calculation of electric and magnetic fields, given that FIT uses matrix equations and FDTD calculates them in an iterative manner. This leads to approximation errors, mainly in the domain borders, and increased solution times. The most important and differentiating advantage in FIT, compared with FDTD, is that it satisfies Maxwell's equations on the whole domain and on every discretization cell allowing the prove of conservation properties of discrete fields in in-homogeneous

bodies.

3.2.1 Maxwell-Grid-Equations

The discretization of the analytical Maxwell's Equations into linear algebraic equations is made using grid functions (cell, face and edge-centers according to Figure 3.2). Due to grid symmetry the introduction of *Maxwell-Grid-Equations* is restricted to a single cell of volume V_N .

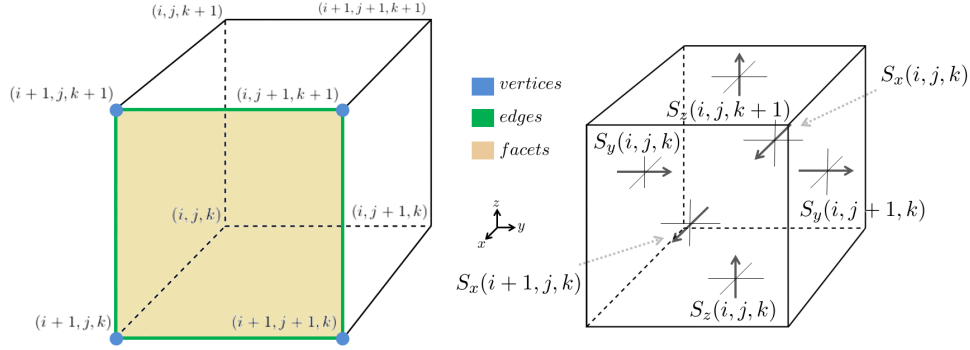


Figure 3.2: Cell complex with adopted nomenclature for grid functions.

Having defined grid doublet $\{\mathbf{G}, \tilde{\mathbf{G}}\}$ in previous Section, and before mathematical relations on Maxwell's Equations are applied to discrete case, the grid electromagnetic quantities used by FIT must be outlined. And so, electric field intensities integral (vectors in cell edges of \mathbf{G}) and magnetic field intensities integral (vectors in cell edges of $\tilde{\mathbf{G}}$) are transformed in electric (Equation 3.9) and magnetic grid voltages (Equation 3.10) respectively:

$$\hat{e}_x = \int_{(x_i, y_i, z_i)}^{(x_{i+1}, y_i, z_i)} \vec{E}(\vec{r}, t) \cdot d\vec{\ell} \quad (3.9a)$$

$$\hat{e}_y = \int_{(x_i, y_i, z_i)}^{(x_i, y_{i+1}, z_i)} \vec{E}(\vec{r}, t) \cdot d\vec{\ell} \quad (3.9b)$$

$$\hat{e}_z = \int_{(x_i, y_i, z_i)}^{(x_i, y_i, z_{i+1})} \vec{E}(\vec{r}, t) \cdot d\vec{\ell} \quad (3.9c)$$

$$\hat{h}_x = \int_{(\tilde{x}_i, \tilde{y}_i, \tilde{z}_i)}^{(\tilde{x}_{i+1}, \tilde{y}_i, \tilde{z}_i)} \vec{H}(\vec{r}, t) \cdot d\vec{\ell} \quad (3.10a)$$

$$\hat{h}_y = \int_{(\tilde{x}_i, \tilde{y}_i, \tilde{z}_i)}^{(\tilde{x}_i, \tilde{y}_{i+1}, \tilde{z}_i)} \vec{H}(\vec{r}, t) \cdot d\vec{\ell} \quad (3.10b)$$

$$\hat{h}_z = \int_{(\tilde{x}_i, \tilde{y}_i, \tilde{z}_i)}^{(\tilde{x}_i, \tilde{y}_i, \tilde{z}_{i+1})} \vec{H}(\vec{r}, t) \cdot d\vec{\ell} \quad (3.10c)$$

Finally, and in accordance to FIT formulation, fluxes are integrated over the surface (S)

oriented relative to either axis direction (Figure 3.2). The magnetic, dielectric and current flux densities are presented in Equations 3.11 to 3.13.

$$\widehat{b}_\zeta = \int_{S_\zeta(i,j,k)} \vec{B}(\vec{r}, t) \cdot d\vec{S}, \quad \forall \zeta = \{x, y, z\} \quad (3.11)$$

$$\widehat{d}_\zeta = \int_{\tilde{S}_\zeta(i,j,k)} \vec{D}(\vec{r}, t) \cdot d\vec{S}, \quad \forall \zeta = \{x, y, z\} \quad (3.12)$$

$$\widehat{j}_\zeta = \int_{\tilde{S}_\zeta(i,j,k)} \vec{J}(\vec{r}, t) \cdot d\vec{S}, \quad \forall \zeta = \{x, y, z\} \quad (3.13)$$

Recalling Equation 3.1c and the previous Equations, the *Maxwell-Faraday's law of induction* can be written for each cell facet in the following ordinary differential equations:

$$\widehat{e}_x(i, j, k) + \widehat{e}_z(i + 1, j, k) - \widehat{e}_x(i, j, k + 1) - \widehat{e}_z(i, j, k) = -\frac{d}{dt} \widehat{b}_y(i, j, k) \quad (3.14a)$$

$$\widehat{e}_y(i, j, k) + \widehat{e}_x(i, j + 1, k) - \widehat{e}_y(i + 1, j, k) - \widehat{e}_x(i, j, k) = -\frac{d}{dt} \widehat{b}_z(i, j, k) \quad (3.14b)$$

$$\widehat{e}_z(i, j, k) + \widehat{e}_y(i, j, k + 1) - \widehat{e}_z(i, j + 1, k) - \widehat{e}_y(i, j, k) = -\frac{d}{dt} \widehat{b}_x(i, j, k) \quad (3.14c)$$

For the electrical grid voltages and magnetic facet fluxes is assumed a lexicographical order over \mathbf{G} and their assembly uses the following expressions:

$$\widehat{e} := (\widehat{e}_x, n | \widehat{e}_y, n | \widehat{e}_z, n)_{n=1, \dots, N_p}^T \in R^{3N_c} \quad (3.15a)$$

$$\widehat{b} := (\widehat{b}_x, n | \widehat{b}_y, n | \widehat{b}_z, n)_{n=1, \dots, N_p}^T \in R^{3N_c} \quad (3.15b)$$

where N_c is the total number of cells in \mathbf{G} .

Equation 3.14 can be written in a more compact form as follows:

$$\mathit{curl} \widehat{e} = -\frac{d}{dt} \widehat{b} \quad (3.16)$$

where curl is the discrete curl operator and is a matrix that contains only topological information on the incidence relation of the cell edges within \mathbf{G} and their orientation. This means that this matrix has only coefficients $\mathit{curl}_{i,j} \in \{-1, 0, 1\}$. More detailed explanation about all discrete operators is found in Section 3.3.2.

The second equation to be approached is *Gauss' law for magnetic field*. Attending that Equation 3.1b describes the non-existence of magnetic charges, the sum of all magnetic flux

through each face of a cell must be equal to zero.

$$\widehat{b}_x(i, j, k) + \widehat{b}_y(i, j, k) + \widehat{b}_z(i, j, k) - \widehat{b}_x(i + 1, j, k) - \widehat{b}_y(i, j + y, k) - \widehat{b}_z(i, j, k + 1) = 0 \quad (3.17)$$

In a similar way this relation can be applied to all cells within \mathbf{G} yielding the discrete divergence operator (*div*) in Equation 3.18 that also depends on grid topology just like the discrete *curl* operator.

$$\text{div } \widehat{b} = 0 \quad (3.18)$$

The discretization of *Ampere-Maxwell's law* is made in analogy to the *Maxwell-Faraday's law of induction* so that the sum of magnetic field intensity is equal to the displacement current and conductive current through the considered facet. And finally, the *Gauss' law for electrical field* for the $\tilde{\mathbf{G}}$ yields the discrete *div* operator for the dual-grid. And so, the last two *Maxwell-Grid-Equations* are given bellow and complemented by some derived results:

$$\widetilde{\text{curl}} \widehat{h} = -\frac{d}{dt} \widehat{d} + \widehat{j} \quad (3.19a)$$

$$\widetilde{\text{div}} \widehat{d} = q \quad (3.19b)$$

$$\widehat{j} = \widehat{j}_m + \widehat{j}_e + \widehat{j}_p \quad (3.19c)$$

$$\widetilde{\text{div}} \widehat{j} = \frac{dq}{dt} = 0 \quad (3.19d)$$

This system of equations will serve as basis for the description of all studied phenomena in this thesis. Some simplifications for the imaging techniques studied here, using mathematical manipulations or discrete operators algebraic properties (Table 3.2), are made to diminish computational burden.

Table 3.1 will assist the interpretation of Maxwell's equations and all electromagnetic quantities in the discrete case for this point forward.

Table 3.1: FIT Discrete Electromagnetic Quantities

Electromagnetic Quantity	Variable	Allocation
electric grid voltage	\widehat{e}	\mathbf{G}
magnetic grid voltage	\widehat{h}	$\tilde{\mathbf{G}}$
magnetic facet flux	\widehat{b}	\mathbf{G}
dielectric facet flux	\widehat{d}	$\tilde{\mathbf{G}}$
current facet flux	\widehat{j}	$\tilde{\mathbf{G}}$
electric scalar potential	Φ	\mathbf{G}
charge distribution	q	$\tilde{\mathbf{G}}$

3.2.2 Discretization of Electromagnetic Operators

The discretization of electromagnetic operators (gradient, divergence, and curl) followed in this Section will be mostly 2D. Even though this thesis is meant for 3D application of Maxwell's equations to a human thorax there are two main advantages in this procedure. First, both gradient (*grad*) and *div* discrete operators in 3D consist on a basic extension of the 2D case, and second, the discretization of the *curl* operator only involves 2D embedded plains, which means that the *curl* operator can be directly extended from 2D discretization of the *grad* operator.

The first operator to be addressed is the *div*, mainly because the discretization of this operator is deduced naturally from the Gauss' formula for the divergence of a cell with volume V_N (Figure 3.3).

$$\frac{1}{V_N} \int_{cell} \nabla \cdot \vec{J} dV = \frac{1}{V_N} \int_{facescell} \vec{J} d\vec{S} = \frac{1}{V_N} (j_{x1} - j_{x2} + j_{y1} - j_{y2}) \quad (3.20)$$

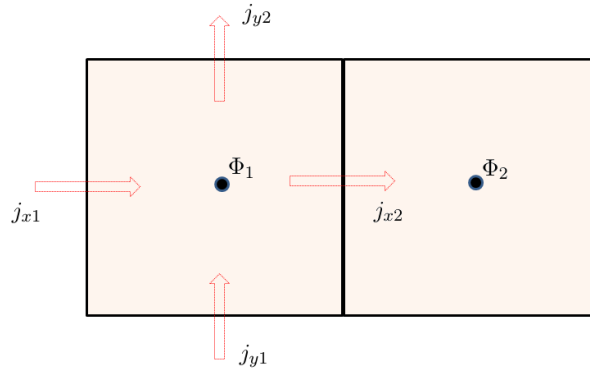


Figure 3.3: Discretization of divergence operator.

Equation 3.20 can be written in matricial form and applied to all cells in \mathbf{G} according to the next expression, resulting in the definition of *div* operator.

$$\begin{pmatrix} \dots & \dots & \dots & \dots \\ \dots & 1 & \dots & -1 & \dots & 1 & \dots & -1 & \dots \\ \dots & \dots \end{pmatrix} \left(\dots \ j_{x1}^N \ \dots \ j_{x2}^N \ \dots \ j_{y1}^N \ \dots \ j_{y2}^N \ \dots \right)^T \quad (3.21)$$

The *div* matrix corresponds to the coboundary operator applied to cochains of degree two (surface degrees of freedom) that yields cochains of degree three, a degree of freedom connected to a whole cell volume (Tonti [1996]). This discretization can be proven to be second order accurate (Haber and Heldmann [2007]) and, as expected, only depends on the grid topology.

To discretize *grad* operator, in FIT context, one must start by representing the electric grid

voltages (located at cell edges) as a difference of discrete potential values, Φ , onto the intersecting grid mesh points, such that the following relations are satisfied:

$$\widehat{e}_x(i, j, k) = \Phi(i, j, k) - \Phi(i + 1, j, k) \quad (3.22a)$$

$$\widehat{e}_y(i, j, k) = \Phi(i, j, k) - \Phi(i, j + 1, k) \quad (3.22b)$$

$$\widehat{e}_z(i, j, k) = \Phi(i, j, k) - \Phi(i, j, k + 1) \quad (3.22c)$$

Using vectors to describe the relations in 3.22 over the whole cell complex \mathbf{G} , one obtain:

$$\widehat{e} = -grad \Phi \quad (3.23)$$

where *grad* maps from cells barycenters to faces and is the negative transpose of the dual discrete *div* operator.

Finally, the discretization of *curl* operator can be made by several forms, being the simplest attained while discretizing the *Maxwell-Faraday's law* in Equation 3.14 resulting in the following expression:

$$\underbrace{\left(\begin{array}{cccccccc} \dots & \dots \\ \dots & 1 & \dots & 1 & \dots & -1 & \dots & -1 & \dots \\ \dots & \dots \end{array} \right)}_{curl} \underbrace{\begin{pmatrix} \dots \\ \widehat{e}_{n1} \\ \dots \\ \widehat{e}_{n2} \\ \dots \\ \widehat{e}_{n3} \\ \dots \\ \widehat{e}_{n4} \\ \dots \end{pmatrix}}_{\widehat{e}} = \frac{d}{dt} \underbrace{\begin{pmatrix} \dots \\ \widehat{b}_n \\ \dots \end{pmatrix}}_{\widehat{b}} \quad (3.24)$$

The other, and more useful way to express this discretization is using a block matrix with blocks equal to extensions of the 2D discretization of the *grad* operator and zero. First, one starts by expanding $\nabla \times$ in Cartesian coordinates for $A = [A_x, A_y, A_z]$:

$$\nabla \times A \equiv \begin{vmatrix} \mathbf{i} & \mathbf{j} & \mathbf{k} \\ \frac{\partial}{\partial x} & \frac{\partial}{\partial y} & \frac{\partial}{\partial z} \\ A_x & A_y & A_z \end{vmatrix} = \left(\frac{\partial A_z}{\partial y} - \frac{\partial A_y}{\partial z} \right) \mathbf{i} + \left(\frac{\partial A_x}{\partial z} - \frac{\partial A_z}{\partial x} \right) \mathbf{j} + \left(\frac{\partial A_y}{\partial x} - \frac{\partial A_x}{\partial y} \right) \mathbf{k} \quad (3.25)$$

And after writing Expression 3.25 in a matricial form

$$\nabla \times A \equiv \begin{pmatrix} 0 & -\frac{\partial}{\partial z} & \frac{\partial}{\partial y} \\ \frac{\partial}{\partial z} & 0 & -\frac{\partial}{\partial x} \\ -\frac{\partial}{\partial y} & \frac{\partial}{\partial x} & 0 \end{pmatrix} \begin{pmatrix} A_x & 0 & 0 \\ 0 & A_y & 0 \\ 0 & 0 & A_z \end{pmatrix} \begin{pmatrix} \mathbf{i} \\ \mathbf{j} \\ \mathbf{k} \end{pmatrix} \quad (3.26)$$

and replacing $\frac{\partial}{\partial x}$, $\frac{\partial}{\partial y}$ and $\frac{\partial}{\partial z}$ for the discretized form of *grad* the final form of the *curl* matrix is obtained:

$$curl = \begin{pmatrix} 0 & -grad_z & grad_y \\ grad_z & 0 & -grad_x \\ -grad_y & grad_x & 0 \end{pmatrix} \quad (3.27)$$

There are some important relations that FIT discrete operators must fulfill. One of which, depicted in Equation 3.28, result from the fact that each electric grid voltage is considered twice and with opposite signals in the *curl* operator. For this reason the overall summation of fluxes, in the assembly of *div* matrix, must be equal to zero (Figure 3.4).

$$div \, curl = 0 \quad (3.28)$$

This relation holds true for both grids and is recognized for its conservation and stability properties once it allows for a unique way to verify correctness and precision of the numerical solution.

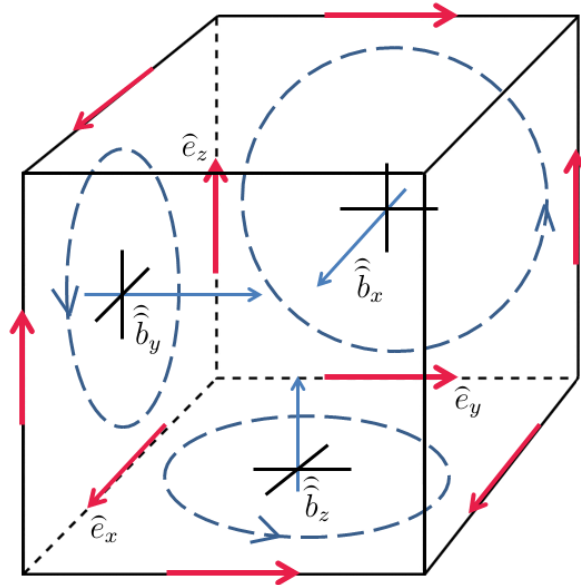


Figure 3.4: Sketch Demonstration of Equation 3.28. For example, \hat{e}_x occurs once with a positive and once with a negative sign for the *curl* summation of fluxes \hat{b}_z and \hat{b}_y .

Other preserved property in FIT, derived from transposition of Equation 3.28 and its dual in combination with the identity, is that gradient fields are irrotacional (Equation 3.29).

$$\text{curl grad} = 0 \quad (3.29)$$

All properties discussed previously, for both \mathbf{G} and $\tilde{\mathbf{G}}$, including those used to reduce the complexity of discretized Maxwell's equations are summarized in Table 3.2, and the nomenclature adopted for the operators in the grid doublet is found in Table 3.3.

Table 3.2: Discrete Operators Algebraic Properties.

$\text{div curl} = 0$	$\widetilde{\text{div}} \widetilde{\text{curl}} = 0$	$\text{grad} = -\widetilde{\text{div}}^T$
$\widetilde{\text{curl}} \text{div}^T = 0$	$\text{curl} \widetilde{\text{div}}^T = 0$	$\text{curl} = \widetilde{\text{curl}}^T$
		$\text{curl grad} = 0$

Table 3.3: Discrete Operators in grid doublet.

Operator	Grid		Dimension
	\mathbf{G}	$\tilde{\mathbf{G}}$	
∇	grad	$\widetilde{\text{grad}}$	$3N_c \times N_c$
$\nabla \cdot$	div	$\widetilde{\text{div}}$	$N_c \times 3N_c$
$\nabla \times$	curl	$\widetilde{\text{curl}}$	$3N_c \times 3N_c$

3.2.3 Discretization of Material Properties

So far the discretization performed for Maxwell's equations in the space of simulation has been artificially bounded and resulted in a exact representation of these equations on $\{\mathbf{G}, \tilde{\mathbf{G}}\}$. But when the variables allocated on one cell needs to be related to its neighbor (from the same or its dual grid complex) an approximation method must be applied in the constitutive material equations.

Starting from the constitutive equations in Section 3.1, FIT defines the matrix relations expressed in Equation 3.30 and dubbed *discrete Hodge operators* (Clemens and Weiland [2001]).

$$\widehat{j}_e = M_\sigma \widehat{e} \quad (3.30a)$$

$$\widehat{d} = M_\epsilon \widehat{e} + \widehat{p} \quad (3.30b)$$

$$\widehat{h} = M_\nu \widehat{b} - \widehat{m} \quad (3.30c)$$

M_σ , M_ϵ and M_ν , in case of isotropic materials, are $N_c \times N_c$ diagonal matrices that contain

information about conductivity, permittivity and reluctivity (the inverse of permeability) space distributions. Equation 3.30b is a variant to Ohm's law and $\widehat{\rho}$ and \widehat{m} arise from permanent electric and magnetic polarization.

Within these matrix equations the relations of degrees of freedom correspond to coupling edge degree with dual facet degrees of freedom in the case of conductivity and permittivity and the inverse coupling process is verified for reluctivity.

The construction of each matrix entry consists in an averaging of the material and grid dimensions. This process, involves a coupling of an edge in \mathbf{G} , that is bounded to the respective electromagnetic quantity that intersects, and a facet of $\tilde{\mathbf{G}}$ being intersected in the middle point.

In the case of conductivity matrix M_σ the diagonal entry m , derived in Equation 3.31, results from a coupling of electric currents and grid voltages in L_m of \mathbf{G} the intersects \tilde{A}_m in $\tilde{\mathbf{G}}$ according to Figure 3.5.

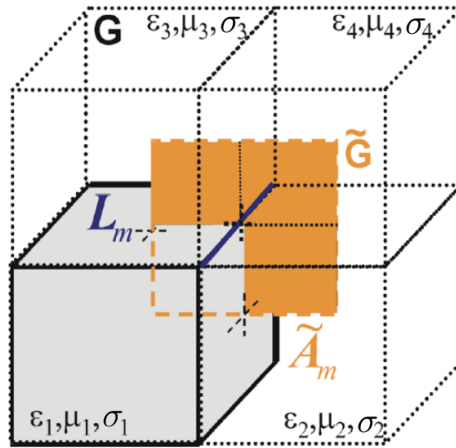


Figure 3.5: Allocation of metrical information of the *Maxwell's-Grid-Equations* and grid dimensions in $\{\mathbf{G}, \tilde{\mathbf{G}}\}$. Taken from Clemens and Weiland [2001] with modifications.

$$\begin{aligned} \frac{\widehat{j}_e^{(m)}}{\widehat{e}^{(m)}} &= \frac{\iint_{\tilde{A}_m} \vec{J} \cdot dA}{\int_{\tilde{L}_m} \vec{J} \cdot dS} + \mathcal{O}(h^l) = \frac{\iint_{\tilde{A}_m} \sigma \vec{E} \cdot dA}{\int_{\tilde{L}_m} \vec{E} \cdot dS} + \mathcal{O}(h^l) \\ &\approx \bar{\sigma} \frac{\iint_{\tilde{A}_m} dA}{\int_{\tilde{L}_m} dS} + \mathcal{O}(h^l) = M_\sigma^{(m,m)} \end{aligned} \quad (3.31)$$

Applying similar reasoning in the diagonal entries of M_ϵ and M_ν , as the one made for M_σ ,

the following expressions are obtained:

$$\begin{aligned} \frac{\widehat{\mathbf{d}}^{(m)}}{\widehat{\mathbf{e}}^{(m)}} &= \frac{\iint_{\tilde{A}_m} \vec{D} \cdot d\mathbf{A}}{\int_{\tilde{L}_m} \vec{E} \cdot d\mathbf{S}} + \mathcal{O}(h^l) = \frac{\iint_{\tilde{A}_m} \epsilon \vec{E} \cdot d\mathbf{A}}{\int_{\tilde{L}_m} \vec{E} \cdot d\mathbf{S}} + \mathcal{O}(h^l) \\ &\approx \bar{\epsilon} \frac{\iint_{\tilde{A}_m} d\mathbf{A}}{\int_{\tilde{L}_m} d\mathbf{S}} + \mathcal{O}(h^l) = M_\epsilon^{(m,m)} \end{aligned} \quad (3.32a)$$

$$\begin{aligned} \frac{\widehat{\mathbf{h}}^{(m)}}{\widehat{\mathbf{b}}^{(m)}} &= \frac{\int_{\tilde{L}_m} \vec{B} \cdot d\mathbf{S}}{\iint_{\tilde{A}_m} \vec{B} \cdot d\mathbf{A}} + \mathcal{O}(h^l) = \frac{\int_{\tilde{L}_m} \nu \vec{B} \cdot d\mathbf{S}}{\iint_{\tilde{A}_m} \vec{B} \cdot d\mathbf{A}} + \mathcal{O}(h^l) \\ &\approx \bar{\nu} \frac{\int_{\tilde{L}_m} d\mathbf{S}}{\iint_{\tilde{A}_m} d\mathbf{A}} + \mathcal{O}(h^l) = M_\nu^{(m,m)} \end{aligned} \quad (3.32b)$$

The l exponent, in the error factor of previous equations, is equal to two in non-uniform grid spacing or if neighbor cells used in the approximation have different conductivities, and otherwise a value equal to three. This error factor highlights the problem discretization in the presence of curved boundary, also known as *Staircase Approximation*. However this error due to the problem geometry and the material averaging in FIT can be reduced using boundary approximation techniques like the triangular filling technique, proposed by Weiland [1979], or the tetrahedral filling technique, by Müller et al. [1982]. The use of non-orthogonal cells is, as well, a solution to decrease this approximation error, but like with other boundary approximation techniques compromises efficiency and presents a huge computational burden. For these reasons, the present thesis fills each cell with only one type of material and grid regions exhibiting discontinuous material interfaces are treated with local mesh refinement.

3.3 Local Mesh Refinement

Local Mesh Refinement arise from time and computational impossibilities of solving large problems with a single resolution mesh. This refinement, consisting in the division of regular elements into sub-elements, is therefore a mandatory requirement to solve 3D problems since it enables the allocation of higher resolution elements where they are required (to better approximate to curvilinear geometries or to accommodate a large variation on the electromagnetic material properties like air-skin transition) and the allocation of lower resolution elements where the solution is of less interest. This prolongation and restriction in the mesh grid may be responsible for some numerical instabilities due to some level of geometry mismatch in the transitions zones.

There is an extensive bibliography for local mesh refinement applied to electromagnetism problems. The first record dates back to Fedorenko [1962] in order to solve elliptic partial

differential equations, but it was after the work of Podebrad et al. [2003] that a consistent subgridding scheme was developed for FIT application. Since then several authors presented a variety of algorithms which led to an overall increase of the flexibility of $\{\mathbf{G}, \tilde{\mathbf{G}}\}$ while preserving the algebraic properties of the *Maxwell-Grid-Equations* (Clemens and Weiland [1999], Bandeira [2009], Caeiros [2010], Rosa [2014]).

Despite several types of refinement found in literature, in this thesis the OcTree type mesh (by Haber and Heldmann [2007]) was considered because it enables high resolution cells over the desired tissues but not in the space between them. The OcTree is generated in a top-down approach by recursively subdividing each cell into eight octants. Although this is an effective approach to subgridding problems, it lacks in efficiency due to its recursive nature, and so instead of a tree like structure to allocate the grid cells a multi-linked list from coarser to finer resolution elements was implemented (allowing a faster and more natural navigation protocol within the grid).

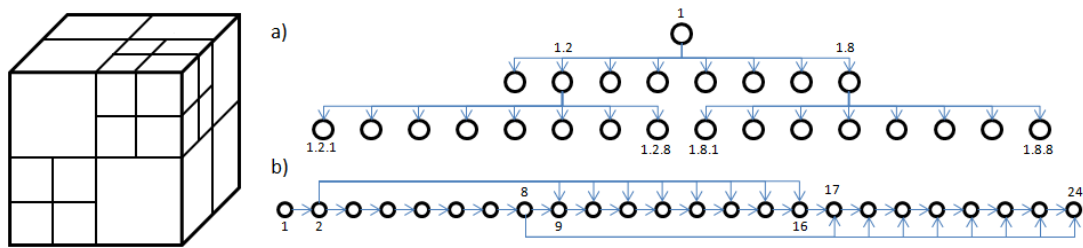


Figure 3.6: Grid refinement structure. a) OcTree top-down approach. b) Multi-linked List

Because FIT requires an exact knowledge of each cell position and its neighbors on every direction, in each subgridding step the neighbors are updated and is established a connection between parent and child as presented in Figure 3.6b). In regular grid this neighbor attribution does not present great challenge because in each direction the neighbors share four vertices, but for irregular grids the same is not verified. In this case a more elaborate and “smart” approach must be applied. The implemented search method in this thesis is presented in Algorithm 1 (see Figure 3.2 for vertices nomenclature).

Algorithm 1 Find Neighbors in x^+ direction. Similar reasoning is applied for remaining directions.

- 1: **procedure** FIND_NEIGHBORS(*Cube_id*, *Mesh*)
 - 2: $vert(1, :) \leftarrow gc(Cube_id(i + 1, j, k));$ $\triangleright gc(vertice)$ returns $[x,y,z]$ coords. of vertice
 - 3: $vert(2, :) \leftarrow gc(Cube_id(i + 1, j + 1, k));$
-

```

4:   vert(3,:) ← gc(Cube_id(i + 1, j, k + 1));
5:   vert(4,:) ← gc(Cube_id(i + 1, j + 1, k + 1));
6:   Result ← [0, 0, 0, 0];
7:   for inc ← 1, size(Mesh) do
8:     Cube ← Mesh(inc);
9:     vert_inc(1,:) ← gc(Cube(i, j, k));
10:    vert_inc(2,:) ← gc(Cube(i, j + 1, k));
11:    vert_inc(3,:) ← gc(Cube(i, j, k + 1));
12:    vert_inc(4,:) ← gc(Cube(i, j + 1, k + 1));
13:    if vert == vert_inc then
14:      return Cube                                     ▷ There is only one neighbor.
15:    else if vert(:, 1) == vert_inc(:, 1) then
16:      Result(1) = Cube;                               ▷ Found bottom-left neighbor.
17:    else if vert(:, 2) == vert_inc(:, 2) then
18:      Result(2) = Cube;                               ▷ Found bottom-right neighbor.
19:    else if vert(:, 3) == vert_inc(:, 3) then
20:      Result(3) = Cube;                               ▷ Found top-left neighbor.
21:    else if vert(:, 4) == vert_inc(:, 4) then
22:      Result(4) = Cube;                               ▷ Found top-right neighbor.
23:    end if
24:    indices ← find(Result == 0);
25:    if isempty(indices) then
26:      return Result;                                 ▷ There are four neighbors.
27:    end if
28:  end for
29:  disp( “error: One or more neighbors missing.”);
30: end procedure

```

3.3.1 Proposed Algorithm for Mesh Refinement

The algorithm for mesh refinement developed in this thesis uses a multi-linked list where the initial elements compose the first level of resolution, or lower resolution, given by the length of each cell, h . From this point, every new addition of lower resolution elements to the structure must fulfill a critical constraint in order to decrease numerical instabilities and large transition zones of material properties. This constraint is that all elements in the grid can not have more

than four neighbors regardless of the direction, implying that each element shares at least one vertice with its neighbors.

Since \mathbf{G} , and $\tilde{\mathbf{G}}$, can not possess a difference higher than one in resolution between neighbor elements an algorithm was developed to monitor each new addition to the structure and create new elements if required. Pseudo-code is presented in Algorithm 2.

Algorithm 2 Compare cell resolution with its neighbors to fulfill grid transition constraint.

```

1: procedure IMPOSE_CONSTRAINT(Cube, Mesh)
2:   list  $\leftarrow$  gn(Cube); ▷ gn(Cube) returns Cube neighbors in array
3:   resolution  $\leftarrow$  gr(Cube); ▷ gn(Cube) returns Cube resolution level
4:   for inc  $\leftarrow$  1, size(list) do
5:     aux_res  $\leftarrow$  gn(list(int));
6:     if aux_res < resolution + 1 then
7:       Mesh  $\leftarrow$  inc_resolution(list(inc), Mesh); ▷ inc_resolution(Cube,Mesh) returns
Mesh after Cube resolution is increased by 1.
8:     end if
9:   end for
10:  return Mesh;
11: end procedure

```

Each element in the grid consists in a nine field structure with the element identification number, vertices coordinates, barycenter coordinates, neighbors identification number, resolution (defined by an integer according Table 3.4), σ , ϵ , μ and children identification numbers if any.

Table 3.4: Adopted nomenclature for cell resolution in grid.

Resolution	h	$h/2$	$h/3$	$h/4$	\dots
Nomenclature	1	2	3	4	\dots

Variables like *mesh* [x, y, z] *dimension*, *geometric center*, *coarser resolution* or maximum cells edge size h are defined by user to generate the initial grid. And then, in an automatic way, the user specifies the location, geometrical form, and resolution increase for sequential subgridding in the regions of interest, as shown in Figure 3.7.

Since all elements are in some way linked to each other it is possible to undo changes made by the user to the initial grid. This undo capability may be conjugated to the increase resolution function to allow a time-varying functionality in the EIT grid so that it can adapt to the electromagnetic fields and ultimately reduce numerical errors due to approximation inaccuracies.

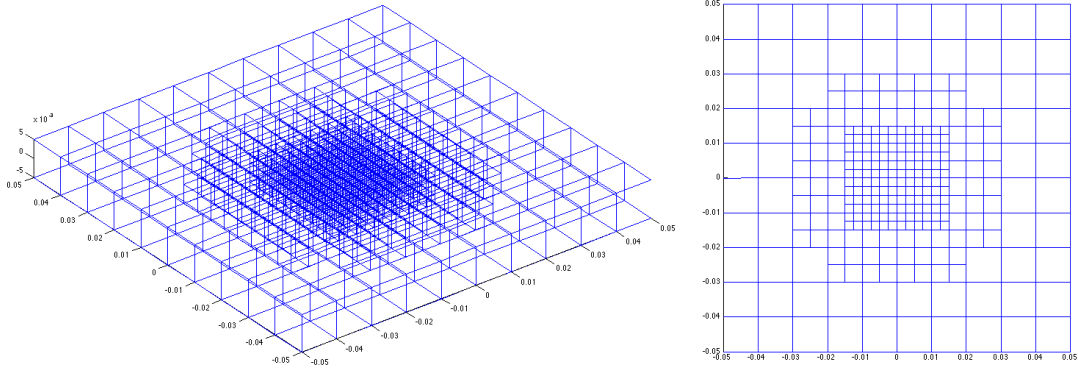


Figure 3.7: Grid example for EIT simulation. Left) 3D view; Right) Top view.

3.3.2 Matrix Operators for Mesh Refinement

As stated in Section 3.3, FIT requires an exact knowledge of each cell position and its neighbors on every direction of the grid. But the existence of elements with different resolutions implies a careful manipulation of the discrete Maxwell's operators because there is no longer a guarantee of one-to-one topological correspondence between elements. Although the one to one correspondence is still present in cells with the same resolution and cells with the higher resolution in the mesh, now there is a maximum of four neighbors for a coarser cell in contact with a finer grid for a particular dimension. Since there may not be direct neighbors in the mesh, reflected by the discrete coefficient set $\in \{-1, 0, 1\}$ of matrix entries for the differential operators, a virtual neighbor (presented in Bandeira [2009] and Bras et al. [2010]) has to be found by interpolation of neighbors interfaces.

This neighbor information is assembled in a set of six $N_c \times N_c$ sparse matrices for each possible direction (x^+ , x^- , y^+ , y^- , z^+ and z^-) in the form $N_{\{component\}\{direction\}}^{\{t-form\}}$ where $\{t-form\}$ refers to the type of form in the grid doublet; $\{component\}$ refers to any of the axis components of the electromagnetic quantity in study; $\{direction\}$ refers any of the six directions mentioned previously.

The lines in these matrices represent an element while the rows identifies its neighbors. Each entry has a value of *zero* if there are no direct neighbors, a value of *one* if the neighbor exists and their resolution is the same, and finally a set of interpolation weights redistributed through all the neighbors in a way that their sum is equal to *one*. These interpolation coefficients depend on where the electromagnetic quantity is allocated in the grid doublet (elements edge, facet or barycenter) and are depicted from Figure 3.8 to 3.10 for an a quantity defined at the facet center of each cell, when transiting from low-to-high and high-to-low resolution grids.

With the information stored in each of the six $N_c \times N_c$ sparse matrix it is possible to construct

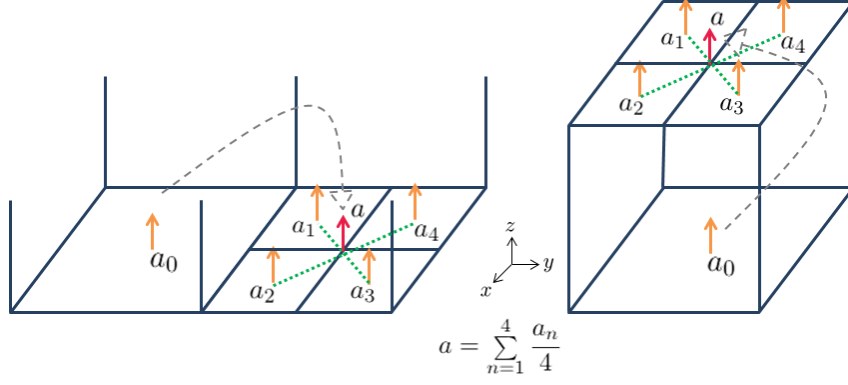


Figure 3.8: Low to high resolution interface for 1-forms. a_n , in orange, can be seen as a electromagnetic quantity along the edges of $\tilde{\mathbf{G}}$ (not shown). The virtual neighbor, a , is represented by a red arrow and the coefficients for N_{zy+} (left) and N_{zz+} (right) matrices are given by the formula below the image.

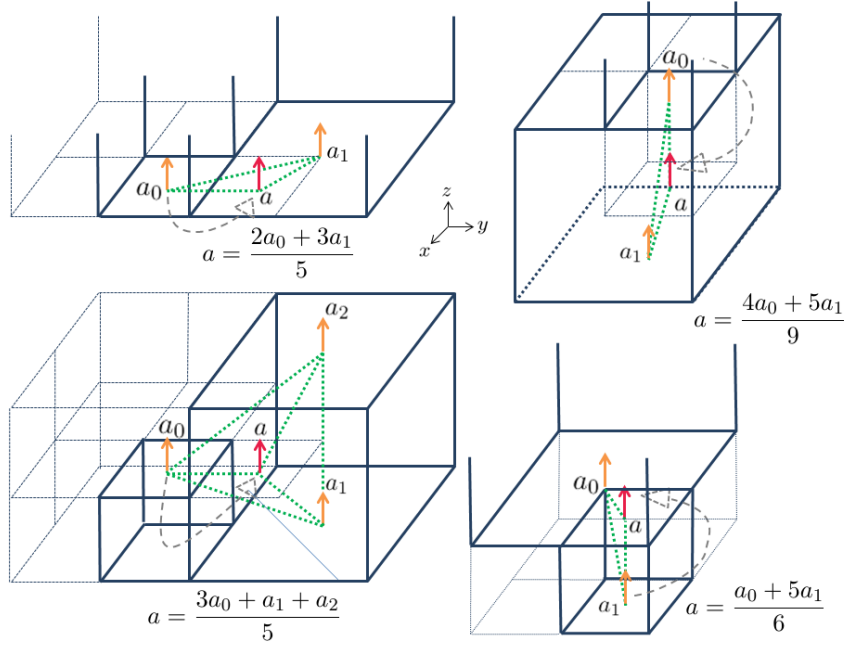


Figure 3.9: High to low resolution interface for aligned and misaligned 1-forms. Arrow nomenclature is the same as in Figure 3.8 and the coefficients for neighbor matrices are given by the formulas presented.

all required differential operators and constitutive relations in a natural and intuitive way. For instance, the p-form of $grad$ and div operators is given in Equation 3.33 and 3.34, respectively.

$$grad_x^p = D - N_{xx}^p \quad (3.33a)$$

$$grad_y^p = D - N_{yy}^p \quad (3.33b)$$

$$grad_z^p = D - N_{zz}^p \quad (3.33c)$$

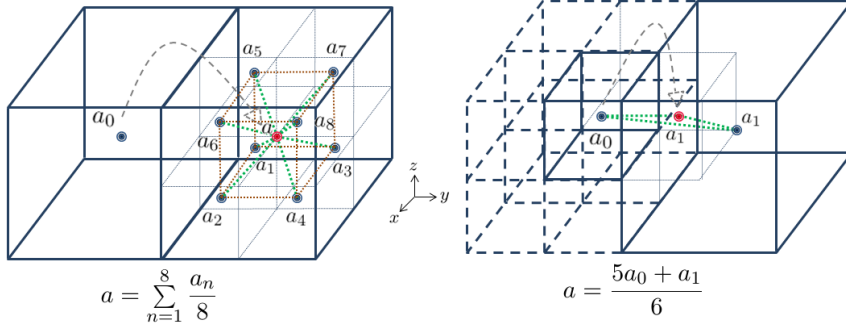


Figure 3.10: Left: Low to high neighbor interface for 0-form. Right: High to low neighbor interface for 0-form. Each virtual neighbor is depicted in red and allocated in \mathbf{G} , while a_n , in blue, are allocated in the barycenters of $\tilde{\mathbf{G}}$. Again, the coefficients for neighbor matrices are given by the formula bellow each image.

D is a $N_c \times N_c$ sparse matrix, with N_c equal to a total number of cells in \mathbf{G} as stated previously.

The fact that *grad* and *div* matrices are defined in opposite directions is to ensure that the electromagnetic operators properties are satisfied as stated in Section 3.3.2, and ultimately leading to the proper solution.

$$div_x^p = N_{xx+}^p - D \quad (3.34a)$$

$$div_y^p = N_{yy+}^p - D \quad (3.34b)$$

$$div_z^p = N_{zz+}^p - D \quad (3.34c)$$

Since all mathematical expressions used to solve the direct problem for each imaging technique only deals with the 0- and 1-*form* of the operators described before, or can be passively reduced to operators assembled with them, the remaining operators will not be demonstrated.

3.4 Grid Electro-Magnetic Validation

All numerical/computer based approaches, in this case to apply Maxwell's equations to electromagnetic problems, must at some point face the issue of result validation in order to measure the proximity of the obtained results when compared to the well-established physics of the problem, and ultimately to the reality (Figure 3.11). With this process one can actually verify the existence of discrepancies and explain eventual differences reproduction found in the simulation environment.

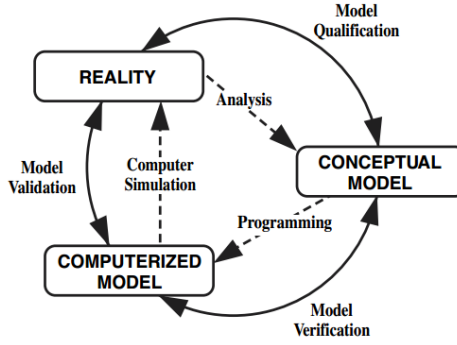


Figure 3.11: Phases of Modeling and Simulation and the Role of Validation (taken from Oberkampf and Trucano [2002])

For this purpose a set of exercises were implemented to assess the fidelity of the computerized model to the underlying conceptual basis and to ensure that the model consists in an accurate representation of the real world for its intended uses.

Given the sparse nature of the operators and the material properties matrices some numerical instabilities were initially expected in the solution of implemented system of equations ($Ax = b$). To overcome this issue a set of numerical optimizations (with preconditioning or conjugate gradient methods) could be implemented. Since the computation of $x = A^{-1}b$ was performed for the system at disposal (2.8 GHz Intel Core i7 processor with four 16 GB of DDR3 SRAM memory slots) in *quasireal* time no optimization method was developed.

3.4.1 Point Charge

This first grid validation section was implemented to establish the propagation of an electromagnetic field and potential through the grid doublet $\{\mathbf{G}, \tilde{\mathbf{G}}\}$. Taking into account that an electric field is produced by any electrically charged object, and *charge* is the fundamental property of forms of matter that exhibit electromagnetic properties, a decision was made to apply *Gauss' Law for electric fields* (Equation 3.1a) to a point charge (C) in space.

Recalling the aforementioned law in FIT notation (Equation 3.19c) one gets:

$$\begin{aligned}
 & \text{assuming } \widehat{p} \\
 \widetilde{div} \widehat{d} = q & \Leftrightarrow \widetilde{div} (M_\epsilon \widehat{e} + \widehat{p}) = q \stackrel{\downarrow}{\Leftrightarrow} \widetilde{div} M_\epsilon (-grad \Phi) = q \Leftrightarrow \\
 & \Leftrightarrow \Phi = -(\widetilde{div} M_\epsilon grad)^{-1} q
 \end{aligned} \tag{3.35}$$

Writing this equation in matrix notation and adopted terminology for the differential oper-

ators, the final expression for *Gauss' Law* is:

$$\underbrace{\begin{bmatrix} \Phi \end{bmatrix}}_{N_c \times 1} = - \left(\underbrace{\begin{bmatrix} div_x^1 & div_y^1 & div_z^1 \end{bmatrix}}_{N_c \times 3N_c} \underbrace{\begin{bmatrix} M_{\epsilon_x} & 0 & 0 \\ 0 & M_{\epsilon_y} & 0 \\ 0 & 0 & M_{\epsilon_z} \end{bmatrix}}_{3N_c \times 3N_c} \underbrace{\begin{bmatrix} grad_x^0 \\ grad_y^0 \\ grad_z^0 \end{bmatrix}}_{3N_c \times N_c} \right)^{-1} \underbrace{\begin{bmatrix} q \end{bmatrix}}_{N_c \times 1} \quad (3.36)$$

This forward model is expressed in the form $x = A^{-1}b$ where A contains the information derived from the product of the differential operators and the material properties and b is an array with entries equal to C for charged elements and equal to *zero* elsewhere. x is the solution of the system, in this case the scalar potential Φ for each of the $N_c = 3125$ cells and is presented in Figure 3.12.

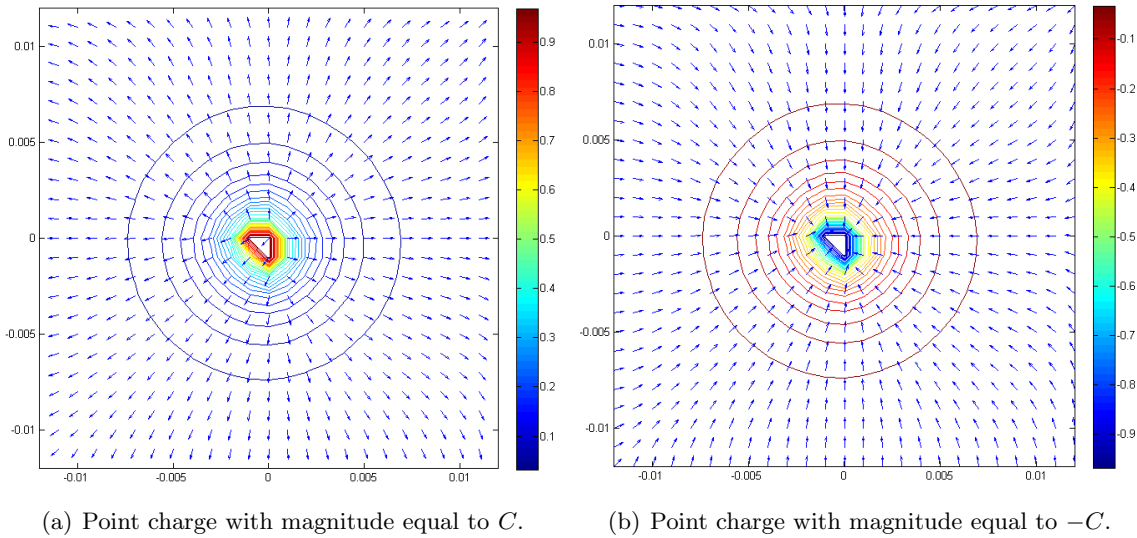


Figure 3.12: Axial cut ($z = 0$ m) of Electric Field Direction (arrows) and Isopotential Lines for a point charge in a discretized mesh with $L_m = 0.001$ m, $(x, y, z) = (0.025, 0.025, 0.005)$ m and centered at the origin. Colorbar normalized to the modulus of applied charge.

From the analysis of electric field direction and isopotential lines obtained with this model is possible to establish that the computerized model behaves in a similar way to the conceptual model and ultimately to the reality. Is even possible to see in Figure 3.13 the correct $1/r$ decrease of electric potential with distance. Due to the bounded space region some small defects can be spotted in electric field direction vectors of elements close to the mesh border, and a unexpected geometry appears in the mesh where the charge is located given the discretized environment and inherent discontinuity in Φ in that place. All this issues are simple to overcome with careful problem modeling and programming.

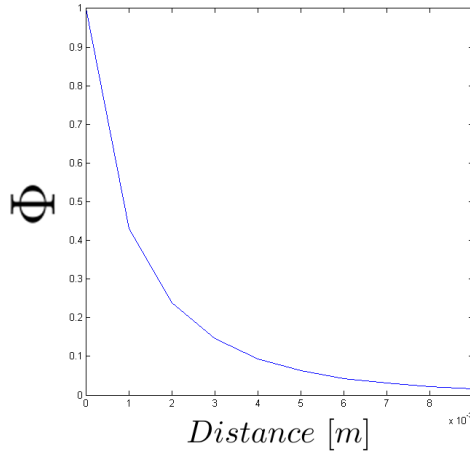


Figure 3.13: Electric scalar potential Φ dependence on distance from a point charge C .

3.4.2 Multiple Charges

Having successfully applied Equation 3.35 to a point charge in space, the next validation exercise that comes to mind is to increase the number of charges in the environment.

In Figure 3.14, an electric dipole consisting of two identical charges in module and of opposite sign separated by a distance d is simulated. This is a simple but very important system to replicate in this computer model because it allows the verification of the superposition principle in Maxwell's equations at work. This principle states that, for all linear systems (like the linear transformation between charges distribution and electric fields), the overall response at a given point caused by multiple stimuli is the sum of the responses which would have been caused by each stimulus individually.

Having successfully simulated an electric dipole, the behavior of electric field and discrete scalar potential in the presence of high/low conductive paths between the charged elements is now evaluated.

As described in Section 2.1, conductors are characterized by having free charges (electrons of atoms last layer with extremely weak bonding energy) that are rearranged within the material when an external electric field is applied. Once these charges are free, the absence of electrical forces in the conductive path when in electrostatic equilibrium is implied, so that $\vec{E} = 0$. Given the lack of electrical forces and Equation 3.23, one can conclude that Φ is constant throughout the entire volume of the conductor. This conductive path must then be a volume at the same potential and with electrical field lines normal to its surface.

In Figure 3.15 two simulations are depicted to demonstrate the computer model capability to adjust the electric field lines and potential according to the medium material properties. As expected, with a material slightly more conductive than the surrounding environment (Fig-

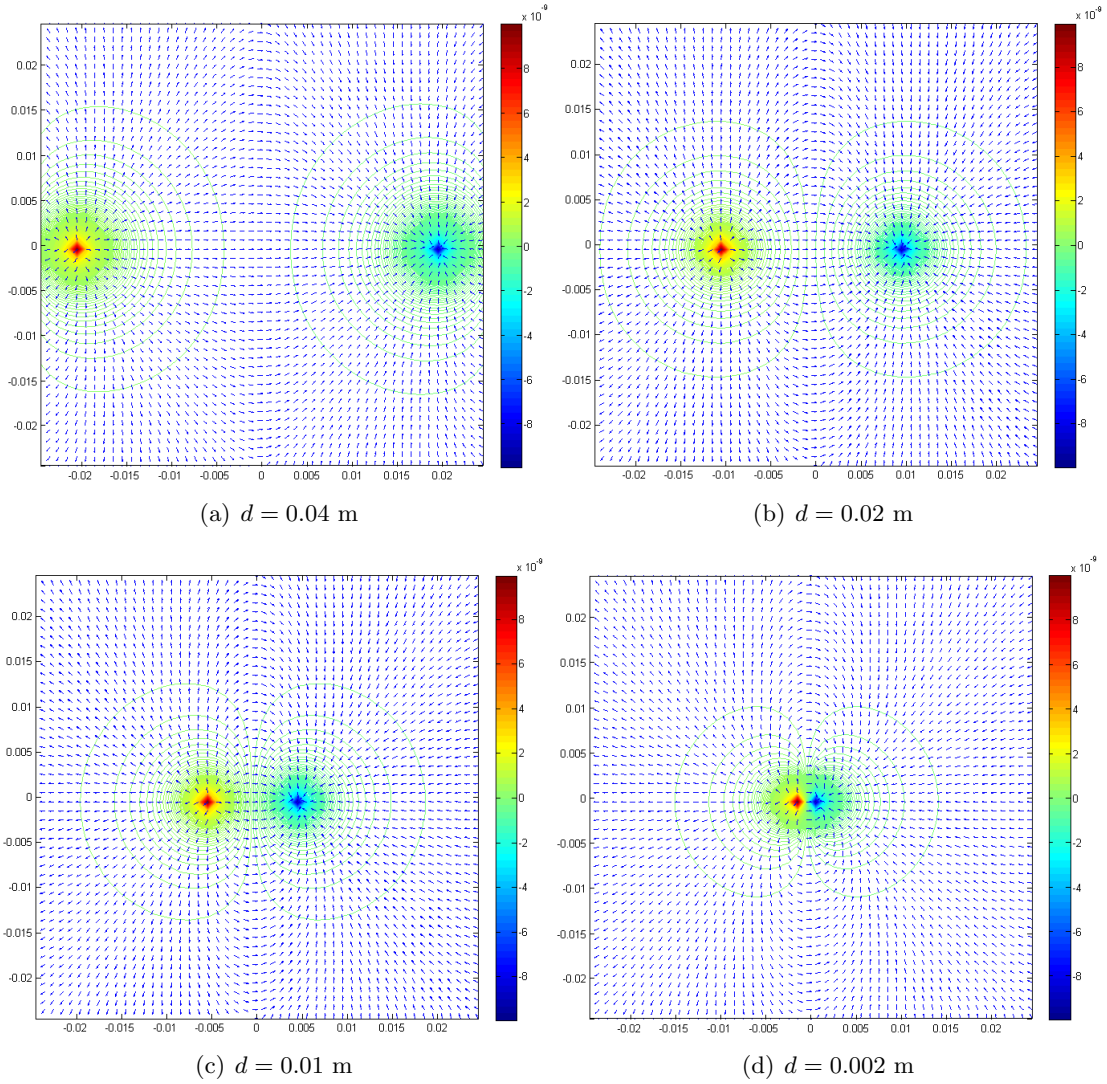


Figure 3.14: Dipole simulation with varying distances between charges with $|C| = 1 \cdot 10^{-8}$. Images correspond to an axial cut at $z = 0$ m of a mesh with the following characteristics: $L_m = 0.001$ m; $(x, y, z) = (0.05, 0.05, 0.01)$ m; $N_c = 25000$. Colorbar in volt.

Figure 3.15(a)) isopotential lines are constant across the conductive volume and the electric field lines tend to travel through this path. With a path less conductive than the environment the reverse is verified (Figure 3.15(b)). To be noted that if the material properties of the conductors were to be similar to those in reality (copper for instance), the obtained results in the simulation indicate no isopotential lines passing through the conductor, backing up the theoretical conclusion that Φ is consistent throughout the entire volume of the conductor.

Finally, a combination of multiple charged elements and conductive materials was simulated to access the electrical field lines behavior in an experimental protocol designed to measure the reactance of different materials.

This experiment, assembled in Figure 3.16, consists in an electromagnetic irradiation board connected to an oscillating voltage source and the corresponding current measurement passing

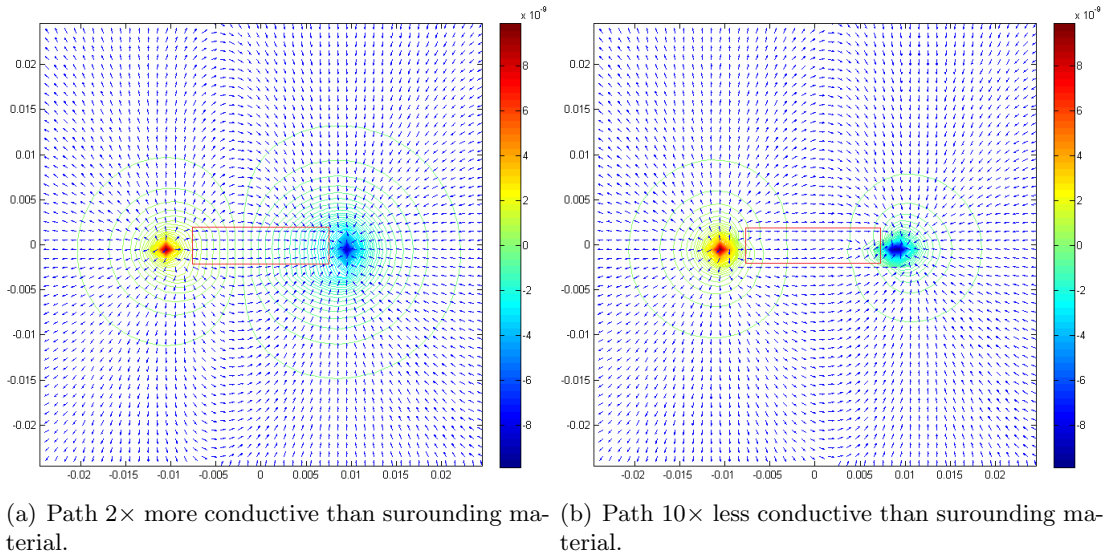


Figure 3.15: Axial cut ($z = 0\text{m}$) of electrical dipole with different conductivities paths between charges. Discretized mesh with $L_m = 0.001\text{m}$; $(x, y, z) = (0.05, 0.05, 0.01)\text{m}$; $N_c = 25000$ and centered at the origin. Colorbar in volt.

through a resistance connected in series to the common ground and the material of interest (at a known distance from the board). The electromagnetic irradiating source must be sufficiently large so that all electric field lines that reach the material are perpendicular to its surface.

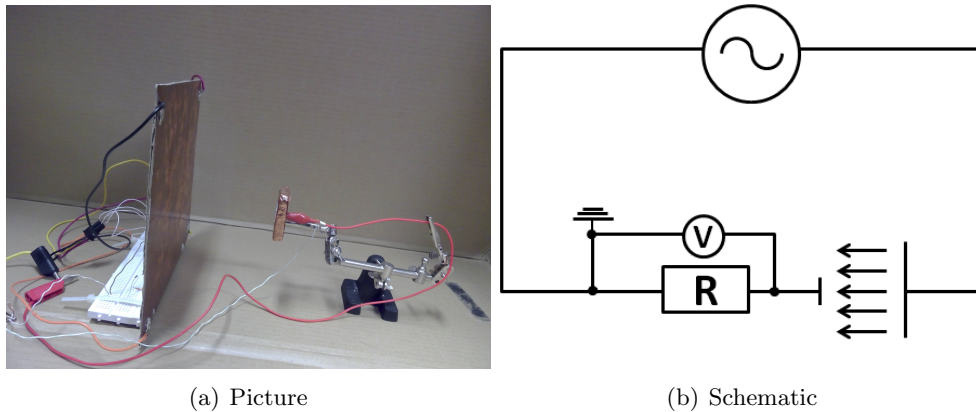
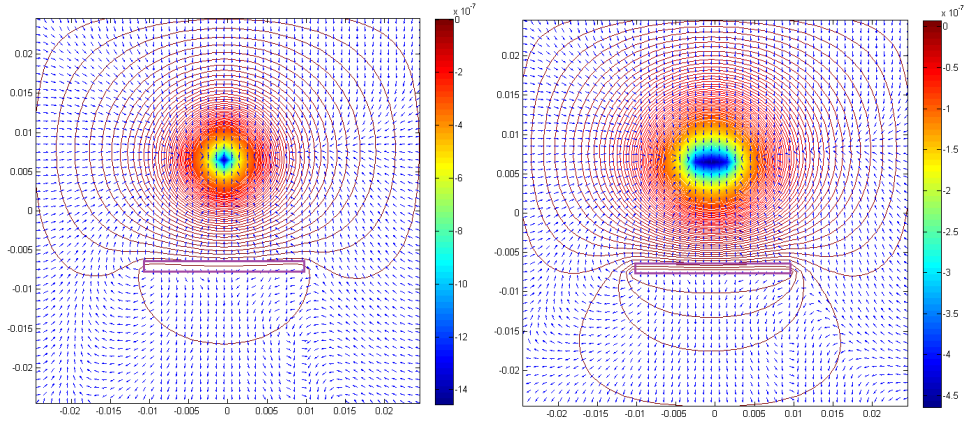


Figure 3.16: Experimental protocol to measure reactance of materials.

From the reproduction of this experiment in computer environment it is possible to identify some parasitic electric field lines that reach the material at the opposite face, and by doing so contaminating the reactance measurements of the sample. For this reason the material must be correctly isolated and connected to the common ground in order to decrease the measurement contamination due to this parasitic currents. Other aspect that can be seen is the relation of board and material size so that all lines that reach the material surface are perfectly perpendicular to it.



(a) Material with surface area of $0.001 \times 0.001\text{m}^2$ (b) Material with surface area of $0.005 \times 0.001\text{m}^2$

Figure 3.17: Axial cut ($z = 0\text{m}$) of electromagnetic irradiation board. The same material is used in both simulations but with different surface areas. Discretized mesh with $L_m = 0.001\text{m}$; $(x, y, z) = (0.05, 0.05, 0.05)\text{m}$; $N_c = 125000$ and centered at the origin. Colorbar in volt.

3.4.3 Helmholtz Coil

Before new tests are performed on the grid, an additional electromagnetic quantity must be presented and discussed, the *Magnetic Vector Potential* - \vec{A} . This quantity is very useful in many physical situations. Besides its large relevance in understanding both classical and quantum physics phenomena (Barbieri et al. [2013]), \vec{A} is fundamental in the discretization process of electromagnetic fields and in electromagnetic gauge theories because the calculation of \vec{B} poses several obstacles in the integration over differential volumes and coils geometry.

Because electric fields generated by stationary charges obey,

$$\nabla \times \vec{E} = 0 \quad (3.37)$$

and since irrotational vector fields are conservative (stationary or slow-moving charges with no acceleration in space) and \vec{E} just depends on charges location it is straightforward to write the electric field as the gradient of Φ . This is clearly a useful thing to do, since it makes possible to replace a vector field by simpler scalar field.

Because \vec{B} satisfies $\nabla \cdot \vec{B} = 0$ either in steady or unsteady currents, which means that the lines of the magnetic vector are closed loops, this electromagnetic quantity can not be described as gradient of a scalar field. And so, one possibility is to write \vec{B} as a *curl* of an auxiliary field.

$$\vec{B} = \nabla \times \vec{A} \quad (3.38)$$

This field was firstly proposed by Maxwell [1873] through an integral relation were \vec{A} is a vector

such that the flux of the magnetic field \vec{B} through any surface Σ is equal to the circulation of \vec{A} around the boundary $\partial\Sigma$ of Σ .

From Equation 3.38 and the *Bio-Savart law* below,

$$\vec{B}(\vec{r}) = \frac{\mu_0}{4\pi} \iiint_V \frac{\vec{J}(\vec{r}') \times (\vec{r} - \vec{r}')}{|\vec{r} - \vec{r}'|^3} d^3 r' \quad (3.39)$$

its possible to deduced the integral expression for \vec{A} :

$$\vec{A}(\vec{r}) = \frac{\mu_0}{4\pi} \iiint_V \frac{\vec{J}(\vec{r}')}{|\vec{r} - \vec{r}'|} d^3 r' \quad (3.40)$$

since $\frac{(\vec{r} - \vec{r}')}{|\vec{r} - \vec{r}'|^3} = \frac{-\nabla}{|\vec{r} - \vec{r}'|}$ and $-\vec{J}\nabla \times \Phi = \nabla \times (\vec{J}\Phi)$

Finally, and prior to the *Helmholtz Coil* mesh validation exercise, is important to highlight that the transformation in Equation 3.38 satisfies the differential operators properties, but \vec{A} is not uniquely defined according to the *Helmholtz's Theorem*. This degree of freedom must be disambiguated by completely defining the boundary conditions, which is termed gauging. In Equation 3.42 is one of the most commonly used gauges, the *Coulomb* choice of gauge.

$$\nabla \cdot \vec{A} = 0 \quad (3.41)$$

One is now in condition to apply the equations defined above to the mesh and access its behavior.

The *Helmholtz Coil* consist in a laboratory technique were a pair of identical coils with equal current flowing through them is assembled in a common axis and spaced one radius apart to obtain a uniform magnetic field between both coils. This assembly is shown in Figure 3.18.

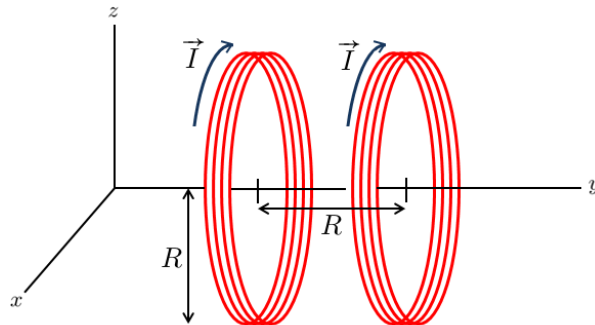


Figure 3.18: *Helmholtz Coil* schematic.

The magnetic vector potential \vec{A} on the grid \mathbf{G} for this example is calculated from the

Biot-Savart law in Equation 3.40. Similarly to electrical scalar potential in the electric dipole simulation, the magnetic vector potential from two coils of the *Helmholtz Coil* arrangement can be found by superimposing the two constituent potentials of each individual coil (Figure 3.19).

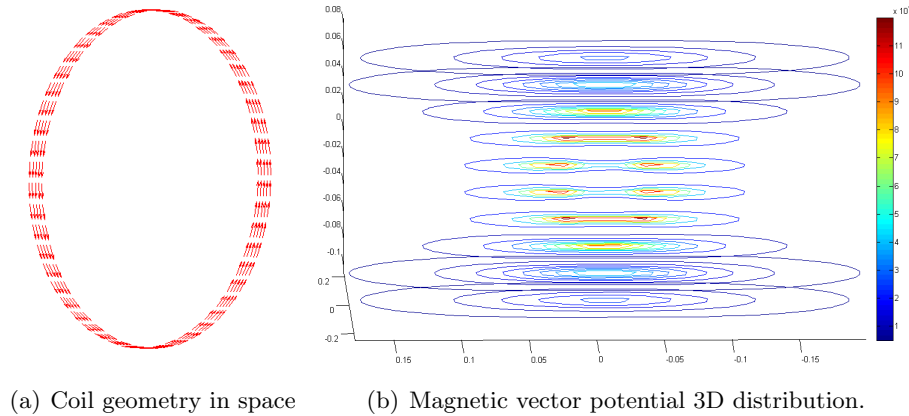
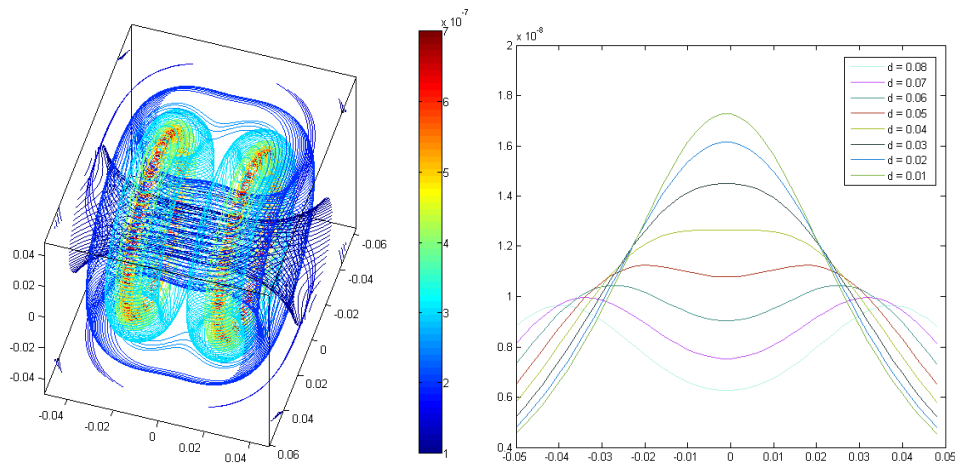


Figure 3.19: Magnetic vector potential of one coil with $radius = 0.04\text{m}$, 5 coil loops and a $Current = 1\text{A}$

In Figure 3.20 the simulation result of the *Helmholtz Coil*, with the computer model developed, is presented. Several distances between the coils were replicated and the result obtained is consistent with theoretical equations and physical conditions addressed previously.



(a) Magnetic vector potential for typical assembly protocol. Colorbar in $\text{V}\cdot\text{s}\cdot\text{m}^{-1}$ (b) Magnetic vector potential distribution, through the coils middle plane, with several distances between coils. Vertical axis in $\text{V}\cdot\text{s}\cdot\text{m}^{-1}$ and horizontal axis in m

Figure 3.20: *Helmholtz Coil* with $radius = 0.04\text{ m}$ computer model simulation. Discretized mesh with $L_m = 0.002\text{ m}$; $(x, y, z) = (0.1, 0.1, 0.1)\text{ m}$; $N_c = 125000$ and centered at the origin.

3.4.4 Electromotive Force

This validation exercise was implemented to test the grid electromagnetic behavior on cells with different resolution levels. In the previous Section the excitation coils were not discretized

over the grid, meaning that these coils are free within the grid domain, and the infinitesimal current-carrying loop pieces can be made as small as desired (considering numerical precision errors).

Unlike excitation coils, the sensing coils needed to calculate the EMF are dependent on the grid element on which the coil passes through. This is why a higher resolution grid is required in the sensing coil region, so that path of the coil in the mesh is better defined and ultimately reducing numerical errors caused by the discretization process.

The expression to calculate the induced EMF in the sensing coils by the varying magnetic field is described by the *Faraday's law* and can be written in the discrete form as,

$$\text{EMF} = -j\omega \sum_{i=1}^{N_{loop}} \sum_{j=1}^{N_{path}} c(i, j) \cdot \hat{a}_{i,j} \quad (3.42)$$

where N_{loop} is the number of loops in the coil, N_{path} is the number of mesh elements that intersect the coil and $c(i, j)$ are the tricubic interpolation coefficients of the magnetic vector potential for each grid element that defines the coil.

In this computer model the sensing coil has 1 *loop* with 0.04 m of diameter. The excitation coils have the same geometrical characteristics, but with a 0.08 m of diameter and carries a current of 1 A. In Figure 3.21(a) is depicted the coils assembly and in Figure 3.21(b) is shown the EMF variation with the angle between the sensing and excitation coils.

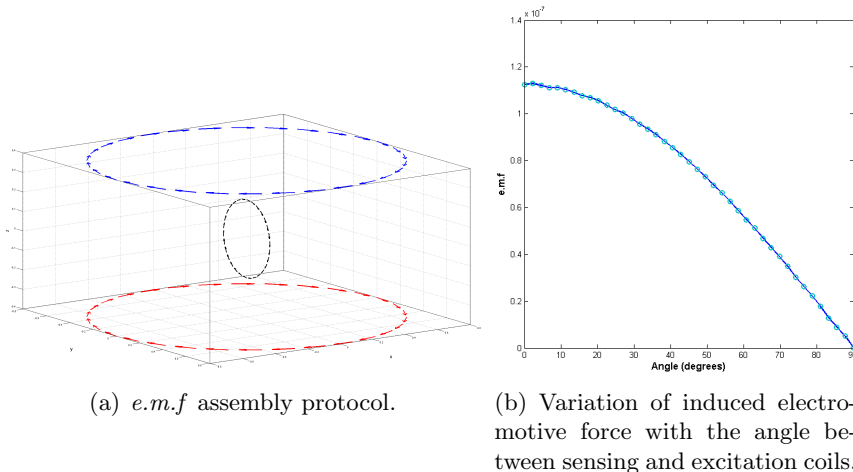


Figure 3.21: *e.m.f* computer model calculation. Mesh area for sensing coil with $L_m = 0.01$ m; $(x, y, z) = (0.5, 0.5, 0.5)$ m; $N_c = 125000$ and centered at sensing coil barycenter.

In this figure, and taking into account the magnetic vector potential properties, is verified the expected rapid decrease of the magnitude with the distance. It should be stated that the order of magnitude of the results are consistent with the ones calculated theoretically, using *Faraday's law*, except in the case were the coils form an angle of 90 degrees with each other. In

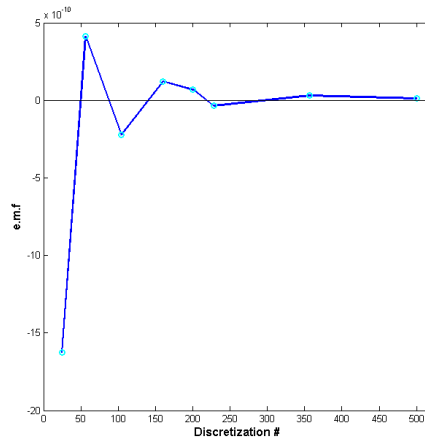


Figure 3.22: *e.m.f* result for 90 degrees angle between coils with increasing discretization of the sensing coil.

this case due to numerical errors the obtained EMF is not *zero* as it was expected, however this value tends to its theoretical result as the coil discretization is improved (see Figure 3.22).

Chapter 4

EIT Inverse Problem

This chapter will describe a linear method - Backprojection Algorithm - for image reconstruction. The respective modifications required to compatibilize it with EIT are also tackled in detail using two different methods followed by the numerical expressions employed in the forward model to retrieve the information about the electric scalar potential distribution at the electrodes position.

Before this method application to the 3D image of a thorax, the backprojection algorithm is studied for variable phantom geometries, sizes and positions to access the model behavior and predict possible artifacts present in the 3D EIT. This chapter ends with the reconstruction of a thorax from a set of CT images.

4.1 Reconstruction Algorithms

The problem of reconstructing a two-dimensional data matrix from a set of one-dimensional information is common to a different set of imaging modalities like CT, PET or SPECT. But unlike these imaging techniques, the reconstruction process for EIT has three main difficulties: (1) there is not a linear-relationship between the biomaterial properties inside the tissue and the measurements of the electrodes because of the “soft-field effect” (the electric field is distorted by the different tissue materials); (2) the problem is under-determined because there are limited number of independent measurements; (3) the inverse problem is ill-posed and ill-conditioned, making the solution sensitive to measurement errors and noise.

In mathematical form, the image reconstruction from data gathered with the forward problem is expressed as:

$$M(p) = d + e \tag{4.1}$$

where p is the real image, d is the data, M is the forward mapping operator and e is the

error between the image mapping and the gathered data. The issues related with the non-linearity of the problem and with the data insufficiency can be surpassed with increased electronic capabilities (hardware) and with better reconstruction models (software). The ill-conditioning of the problem is avoided if M has a well-defined inverse whose domain is all of data space, and if the condition number of M is controlled.

The reconstruction algorithms can be labeled as *Linear* or *Non-linear* and *Iterative* or *Non-iterative*. *Linear* algorithms, as the name implies, assume that a linear change occurs in the data when a small perturbation is introduced in the phantom. Due to the nature of these algorithms their performance is increased, and in some cases reduced to a simple matrix operation, when compared with *Non-linear* algorithms - designed only for small variations from an initial reconstruction estimation. Regarding the *Iterative* and *Non-iterative* nature of the algorithms, while the former is better suited for reconstruction of non-smooth distributions and present themselves as expensive from a computational point of view, the latter type have the advantage of being computationally inexpensive and can be calculated in real-time. For these reasons a *Linear* and *Non-iterative* reconstruction algorithm - *Back-projection* - based on the Radon Transform in CT, similarly to the one implemented in Mk1, was chosen.

The reconstruction process, in a tomographic imaging system like CT, is based on the principle that a 2D slice of the internal structure of an object ($f(x, y)$) can be reconstructed from a series of one-dimensional projections ($P_\phi(r)$) of the object acquired at different angles (ϕ), as seen in Figure 4.1. Regardless of the physical property of each system, the different signal intensities detected in these projections correspond to physical distribution of such property on the object.

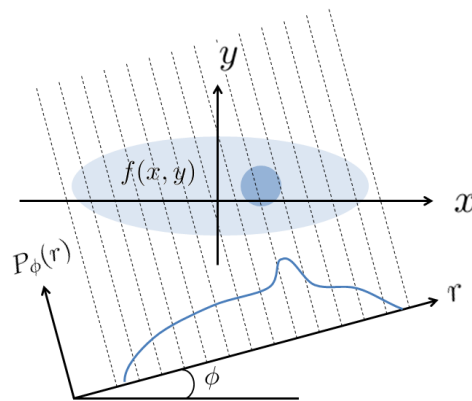


Figure 4.1: Projections through an object and the corresponding coordinate system for CT.

Each projection line is equally divided between the elements crossed by it, and in the end this process is repeated for all of the projections giving each element the sum of intensities of

all projection lines passing through it. Mathematically, this can be represented as

$$\hat{f}(x, y) = \sum_{j=1}^n P_{\phi_j}(r) d\phi \quad (4.2)$$

where n is the total number of projections.

Due to the linear characteristics of the x-ray path in the traditional *Backprojection* algorithm an adaptation to this method, presented in next Section, was made in order to include the electric current behavior through a material with constant properties.

4.2 Isopotential Calculation

In general, current imaging modalities are based on linear energy signals transmission. With this condition is possible to reconstruct, with relative accuracy, the limits and region of the image. But in the case of EIT the radiating energy proceeds along an unknown path or even along several paths making it impossible to reconstruct as accurate image. This poses the fundamental problem in EIT because the electric current cannot be forced to flow linearly in a non-homogeneous conductor.

For this reason the electric current path is estimated in a homogeneous conductor in order to assign every pixel in the image the corresponding electrical potential value registered at the electrodes on the boundary (see Figure 4.2). In the following Sections (4.2.1 and 4.2.2) two methods are described to estimate the electric field isopotential lines within a body.

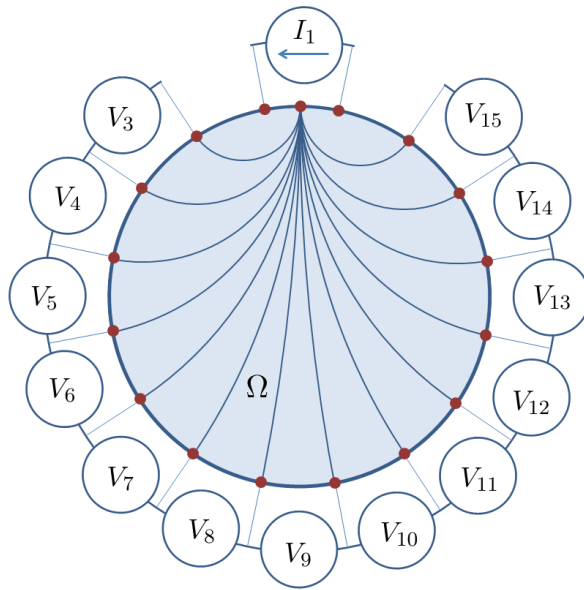


Figure 4.2: Image reconstruction conducted along the isopotential lines.

Because of this relation between image pixel and potential at the border electrode is immedi-

ate the conclusion that the number of electrodes is directly proportional to the image resolution. However, because the ill-posedness of the reconstruction problem this linear relationship is only valid if there is sufficient instrument precision so that with the increase of electrodes it also increases the variety of acquired information (Holder [2005]).

4.2.1 Electrical Field

Echoing the work done by Santosa and Vogelius [1990], the isopotential lines in a circular test phantom with homogeneous conductivity are built by following the electric field line that passes through each cell barycenter. When each electric field line reaches a specific place in the phantom boundary the correspondent electrical potential value at the boundary is assigned to the cell. Because the phantom boundary can not be entirely covered by discrete electrodes the assignment of electrical potential value to each cell is made with an weighted average of potentials recorded at the closest electrodes to the coordinates where the electrical field line reached in the border.

The implemented algorithm to construct the isopotential lines is presented in Algorithm 3. For every rotation of the dipole this algorithm is applied and the electrode-cell pair is stored in a matrix.

Algorithm 3 Assign border potential to pixel in image.

```

1: procedure BUILD_ISOPOTENTIAL(Body_IDs, Mesh, charged_coords, charge, step)
2:    $k \leftarrow \frac{1}{4\pi\epsilon_0}$ ;
3:   for element  $\leftarrow 1, \text{size}(\textit{Body\_IDs})$  do
4:     boolean  $\leftarrow 1$ ;
5:     coords  $\leftarrow \textit{mesh}\{\textit{Body\_IDs}(\textit{element})\}$ ;
6:     while boolean do
7:        $E_X \leftarrow 0$ ;
8:        $E_Y \leftarrow 0$ ;
9:       for q  $\leftarrow 1, \text{size}(\textit{charged\_coords})$  do
10:         $d_X \leftarrow \textit{coords}(X) - \textit{charged\_coords}(q, X)$ ;
11:         $d_Y \leftarrow \textit{coords}(Y) - \textit{charged\_coords}(q, Y)$ ;
12:         $E_{aux} \leftarrow \frac{k \cdot \textit{charge}(q)}{d_X^2 + d_Y^2}$ ;
13:         $\theta \leftarrow \arctan(d_X, d_Y)$ ;
14:         $E_X \leftarrow E_X + E_{aux} \cdot \cos(\theta)$ ;
15:         $E_Y \leftarrow E_Y + E_{aux} \cdot \sin(\theta)$ ;
16:       end for

```

```

17:    $\Delta_X \leftarrow \frac{-(step \cdot E_Y)}{\sqrt{E_X^2 + E_Y^2}};$ 
18:    $\Delta_Y \leftarrow \frac{-(step \cdot E_X)}{\sqrt{E_X^2 + E_Y^2}};$ 
19:    $coords \leftarrow [coords(X) + \Delta_X, coords(Y) + \Delta_Y];$ 
20:   if isCoordInBodyY(coords, Body_IDs) then
21:        $coords \leftarrow [coords(X) - \Delta_X, coords(Y) - \Delta_Y];$ 
22:        $iso\_matrix(element) \leftarrow closest\_electrods(charged\_coords, coords);$ 
23:        $boolean \leftarrow 0$ 
24:   end if
25: end while
26: end for
27: return iso_matrix;
28: end procedure

```

The result of this algorithm is presented in Figure 4.3 for a 2D circular phantom with 25600 elements, having taken nearly eight minutes to complete. At the phantom boundary 64 electrodes were equidistantly placed and the injection protocol consisted in adjacent electrodes injection as depicted in Figure 4.2.

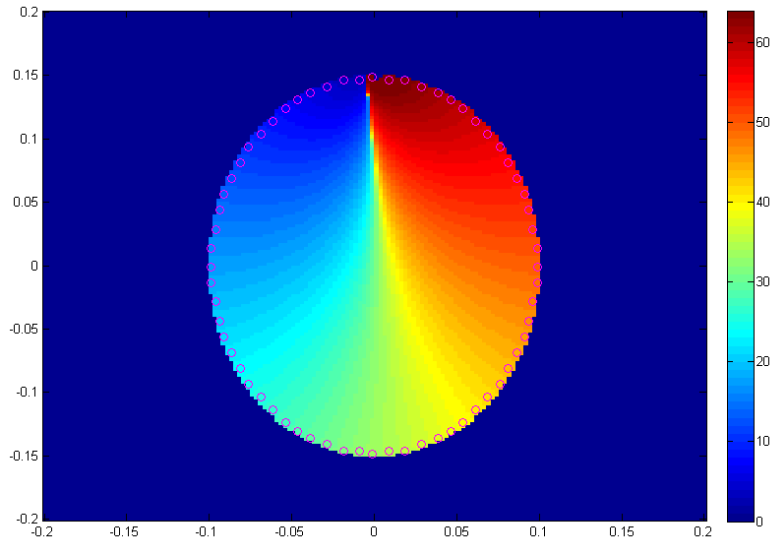


Figure 4.3: Isopotential lines obtained through the electric field calculation. Electrodes position are marked with magenta circles and the colorbar indicates the electrode identification number.

Figure 4.4 intends to demonstrate the isopotential lines dependence on the pattern in which the current is being injected, or in other words, the electric dipole placement at the boundary when, for instance, is applied the opposite method protocol. In this method current is injected

through two diametrically opposed electrodes.

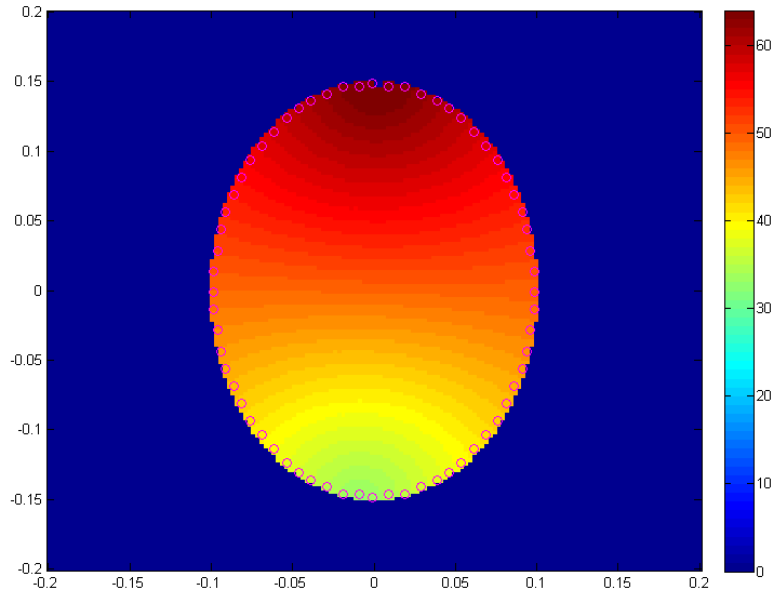


Figure 4.4: Isopotential lines with opposite method. Electrodes position are marked with magenta circles and the colorbar indicates the electrode identification number.

4.2.2 Möbius Transformation

One of the reasons that led to the search of another solution to calculate isopotential lines was the high computational cost involved in following each electric field line that passes through all cells barycenter until it reaches the phantom boundary. This method, previously defined in Section 4.2.1, also implies the knowledge of all border elements coordinates and a constant search between them to access the electric field line position evolution until it reaches one of the border elements.

Influenced by Barber and Brown [1986] where a more convenient space was arranged to find the relationship between electrical potential distribution at the boundary and the resistance within the problem region, and considering that the current flows along circular paths between electrodes (implying that isopotential lines are also arcs of circles), a bilinear transformation can be applied to convert the problem of construction isopotential lines into a more convenient rectangular system.

The Möbius transformation is a class of elementary mappings studied by *August Ferdinand Möbius* that are expressed as a quotient of two linear expressions (Equation 4.3) defined on the extended complex plane $\hat{\mathbb{C}} = \mathbb{C} \cup \{\infty\}$.

$$f(z) = \frac{a + zb}{c + zd} \quad (4.3)$$

$f(z)$ is an invertible meromorphic (complex differentiable on an open subset of the complex plane) function, and so conformal everywhere, that maps lines and circles into lines or circles. This complex mapping was defined later by Arnold and Rogness [2008] as a *stereographic projection of the complex plane onto an admissible sphere in \mathbb{R}^3 , followed by a rigid motion of the sphere in \mathbb{R}^3 , followed by stereographic projection back to the plane.* The condition $ad \neq bc$ must be satisfied to preclude the possibility that $f(z)$ reduces to a constant.

The general Möbius transformation in Equation 4.3 can be written as a sequence of simpler transformations composed by translations (maps of the form $z \mapsto z + k$ where $k \in \mathbb{C}$), dilations (maps of the form $z \mapsto kz$ where $k \in \mathbb{C} \setminus \{0\}$) and inversions (maps of the form $z \mapsto 1/z$) according to Expression 4.4.

$$f(z) = f_4 \circ f_3 \circ f_2 \circ f_1(z) \quad (4.4)$$

with $f_4(z) = z + \frac{c}{d}$, $f_3(z) = \frac{1}{z}$, $f_2(z) = \frac{ad - bc}{d^2}z$ and $f_1(z) = z + \frac{b}{d}$

Each of the simpler Möbius transformations is represented in Figure 4.5 for a circle with *radius* = 0.5 m and centered at $(x, y) = (0.5, 0)$ m.

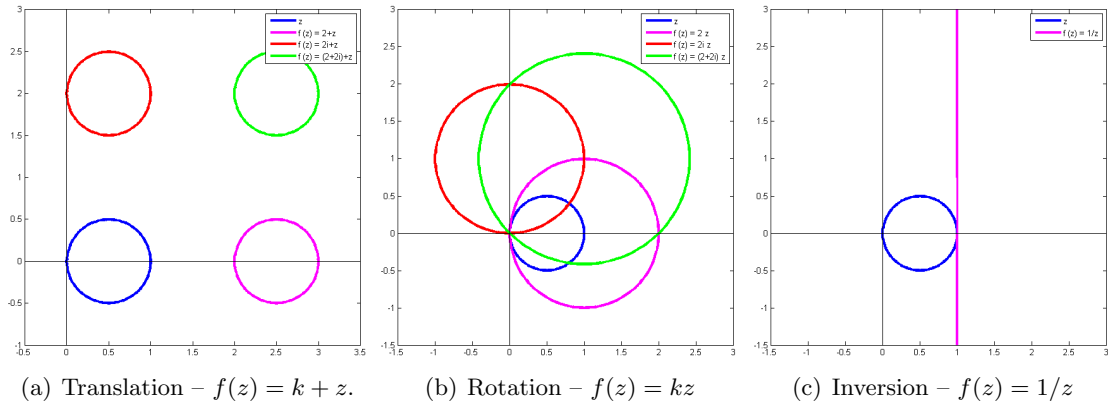


Figure 4.5: Möbius transformation. Axis in m

From the three simple transformations, displayed in the previous Figure, the inversion transformation ($f(z) = 1/z$) is clearly the ideal to convert the problem of construction isopotential lines into a more convenient rectangular system. Inspecting this transformation in the polar form, Equation 4.5, (1) f interchanges outside and inside of the unite circle, (2) if a circle is centered at zero it is mapped to a circle of reciprocal radius also centered at zero, (3) if a circle is not centered or passes through the origin is mapped to a circle and (4) if a circle is not centered at zero but intersects the origin is mapped to a line (also viewed as a circle trough infinity).

$$z = re^{i\theta} \Rightarrow f(z) = \frac{1}{z} = \frac{1}{r}e^{-i\theta} \quad (4.5)$$

The mapping of circles, or arcs of circles in the case of isopotential lines, to lines with the Möbius transformation is accomplished by placing the electric dipole (responsible for the electric injection in EIT) at the origin as is represented in Figure 4.6.

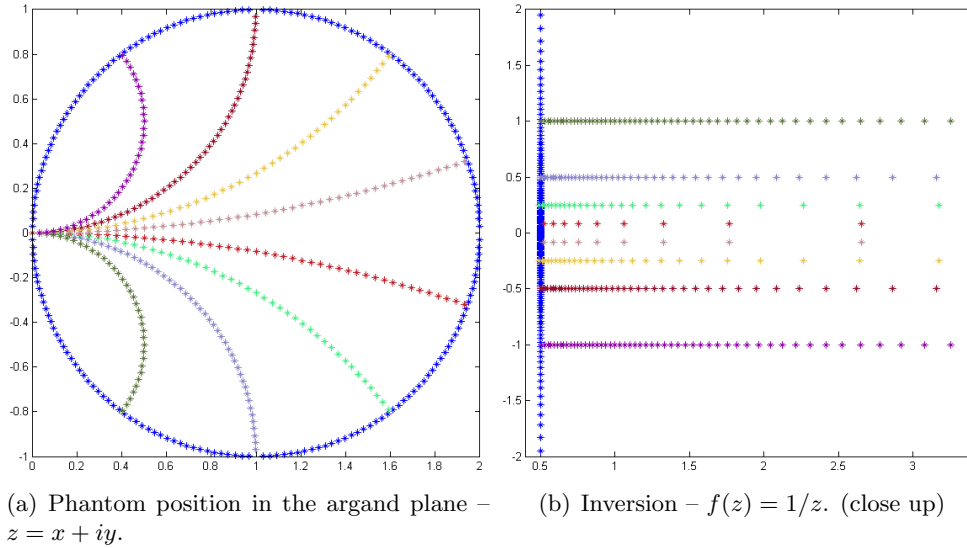


Figure 4.6: Möbius transformation of isopotential lines.

Inspecting Figure 4.6(b), is immediate the conclusion that for isopotential lines construction only imaginary part resulting from the Möbius transformation is relevant. The phantom border, marked in blue, is discretized and transformed into the new space according to number of electrodes and their location. Each electrode reconstruction imaginary part is stored, as are all cells in the phantom. The isopotential lines are constructed according to the proximity of cells and electrodes imaginary part. Unlike the algorithm implemented in Section 4.2.1 this reconstruction is only possible for tomographic imaging techniques. In Figure 4.7 the reconstruction result is presented, showing a more consistent isopotential geometry then the one obtained in previous section.

Compared with the isopotential reconstruction with the electric field lines, the Möbius transformation method is faster, in fact $93\times$ faster than its counterpart, and yields isopotential lines with better circular geometry. For these reasons, and others yet to be enumerated, Möbius transformation is considered best suited for isopotential lines reconstruction in the backprojection algorithm of tomographic images.

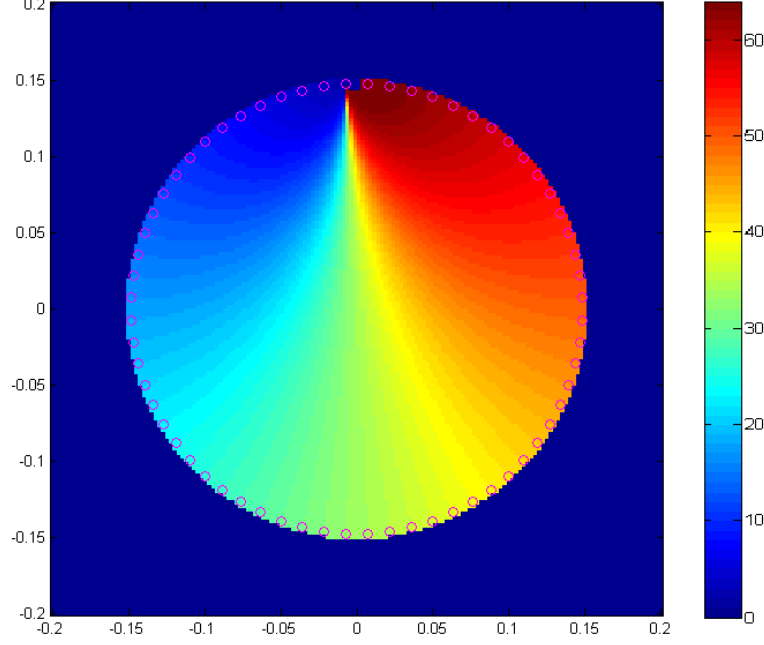


Figure 4.7: Isopotential lines calculated with the Möbius transformation method.

4.3 Input Data

For the reconstruction of any image in this thesis, using the backprojection algorithm, the *Input Data* consisted in the scalar potential obtained at the border of the phantom (particularly in the position of the electrodes) by solving the EIT forward problem when the external stimulus and the admittivity map distribution within the body is known. The derivation of the numerical form begins by re-writting the discrete *Ampere-Maxwell's law* and assuming negligible any magnetic and polarization currents ($\widehat{j} = \widehat{j}_e$):

$$\widetilde{curl} \widehat{h} = \frac{d}{dt} \widehat{d} + \widehat{j} \Leftrightarrow \widetilde{curl} \widehat{h} = \frac{d}{dt} [M_\epsilon \widehat{e}] + \widehat{j} \Leftrightarrow \widetilde{curl} \widehat{h} = [j\omega M_\epsilon + M_\sigma] \widehat{e} \quad (4.6)$$

where $\widehat{j} = M_\sigma \widehat{e}$ and $\frac{d}{dt} \widehat{e} = j\omega \widehat{e}$ given that the electromagnetic quantities are in the form of time harmonic fields.

A common approximation in EIT forward problem is that \widehat{h} is neglected for the operational frequencies, endorsing the assumption that the electric field is irrotational, and allowing the use of Equation 3.23 to obtain:

$$\widetilde{curl} \widehat{h} = -[j\omega M_\epsilon + M_\sigma] grad \Phi \quad (4.7)$$

The application of the *div* operator in both sides of the Equation 4.8, to make use of the

operators property in Equation 3.28, leads to the final numerical expression for EIT:

$$-\widetilde{div}[j\omega M_\epsilon + M_\sigma]grad\Phi = 0 \quad (4.8)$$

A new equation must be added in the final system to account for the additional current term (\widehat{j}_s) responsible for the cells representing electrodes that behave as the source and sink of electric current, yielding the implemented equation system:

$$\begin{cases} \Phi_{in} = -\Phi_{out}, \text{ current driving pair} \\ -\widetilde{div}[j\omega M_\epsilon + M_\sigma]grad\Phi = 0, \text{ elsewhere} \end{cases} \quad (4.9)$$

4.4 2D Image Reconstruction

In this section the computational mesh developed for simulation of the EIT forward problem consisted in simple bi-dimensional geometric figures. The focus of the simulation is to test the backprojection algorithm in several conditions, like phantom location inside the mesh or phantom size and shape or the number of electrodes used, to support the choices made for the 3D thorax imaging problem. No refinements were applied in these meshes and the total number of elements (N_c) was 25600 with grid resolution of 0.0025 m.

4.4.1 Results

The first result, in Figure 4.8(b), consists in one projection of simple voltage difference. This poor outcome is due to the fact that the admittivity inside the phantom besides being a function of the scalar electric potential at the border is also dependent on the area between the isopotentials. For this reason the backprojection *data* must be normalized using the potential between electrodes when the phantom has constant admittivity, also known as *reference data*. This method, named differential imaging, can only be applied if both *data* and *reference data* are acquired with the same injection current.

A more subtle argument, presented in Barber and Brown [1986], implied that images should be reconstructed with the *log* conductivity ratio rather than the conductivity itself. The results obtained for both cases, shown in Figure 4.9, are clear on the benefits of the *log* conductivity reconstruction.

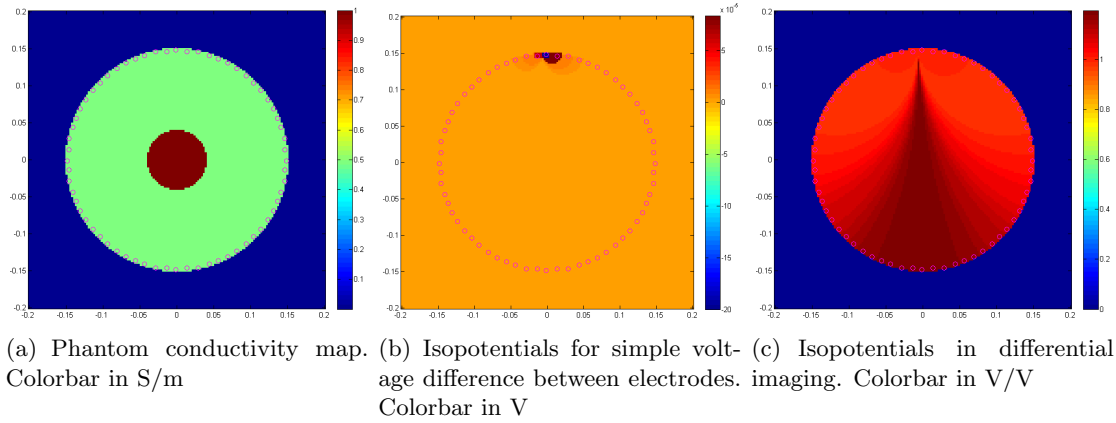


Figure 4.8: Backprojection isopotentials with adjacent electrodes protocol for phantom with an increased conductivity sphere with 0.04 m radius at the center.

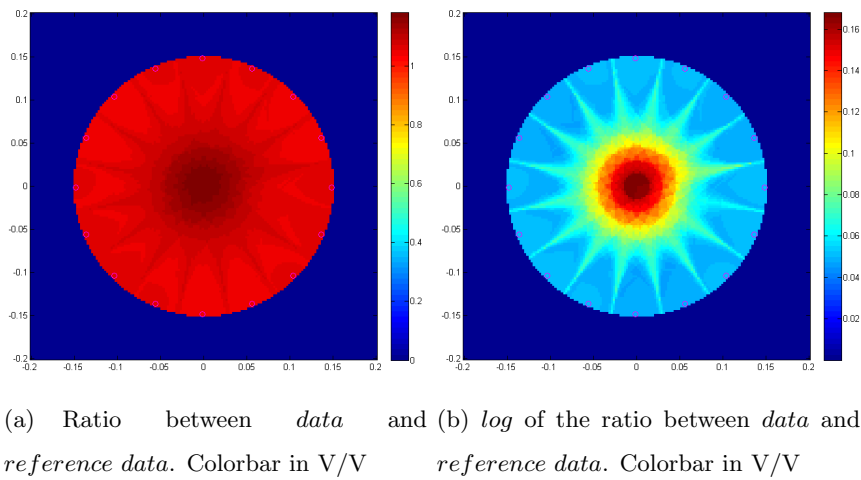


Figure 4.9: Backprojection reconstruction of phantom in Figure 4.8(a) for a system of 16 electrodes with adjacent electrode protocol.

Artifacts, like the ones presented in the previous figure, are commonly encountered in most clinical imaging systems, and may obscure or simulate pathologies. The artifacts that streaks the reconstructed images here presented, and in a similar way as it is verified in CT, arise from the limited number of projections used in the numerical reconstruction formula of the backprojection algorithm. If the number of electrodes is increases, the influence of these streaks in the image decreases as exhibit in Figure 4.10.

Due to hardware limitations and computer mesh resolution there is a limit to the number of electrodes that can be used in EIT imaging system. In the following reconstructed figures of this Section a set of 64 electrodes were used as a good compromise between images artifacts and computational burden.

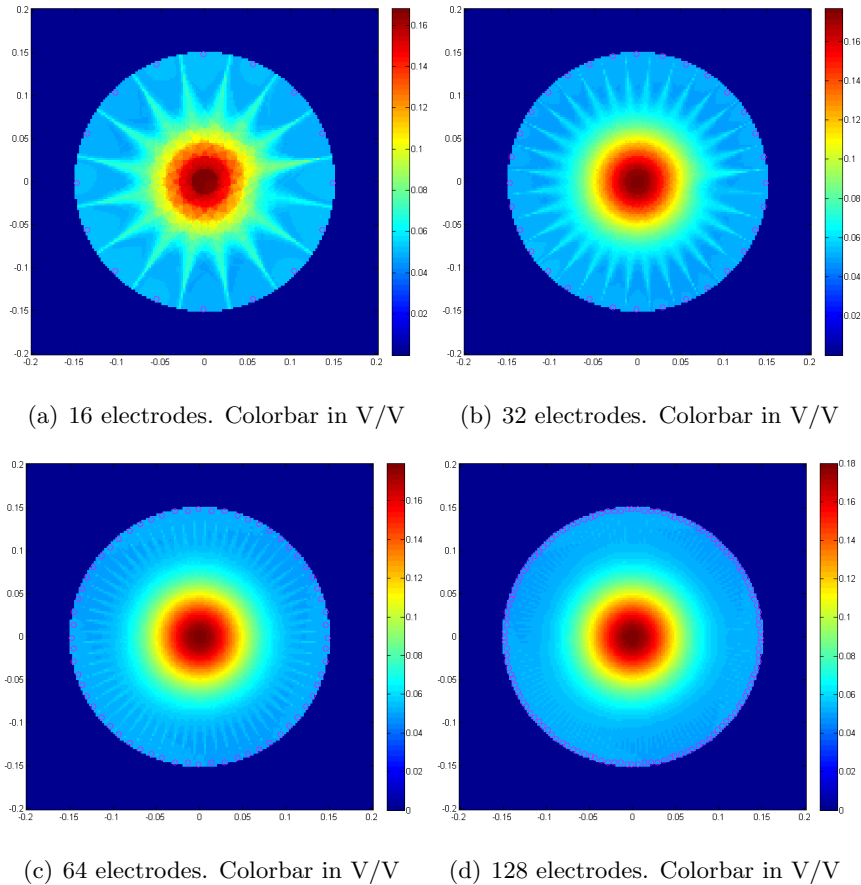


Figure 4.10: Backprojection reconstruction with increasing number of electrodes.

The next set of results aim to study the reconstruction algorithm for different phantom sizes and positions within the mesh. From Figures 4.11(a), 4.11(b), 4.10(c), and 4.11(c), with decreasing phantom sizes, is possible to view the effects of backprojection blurring in the reconstructed images. Despite a decreasing absolute value in each of the reconstruction, as expected, the size of the phantom becomes increasingly difficult to retrieve as the phantom reduces size due to the blur. Figures 4.11(d), 4.11(e), and 4.11(f) portrait the reconstruction of the same phantom (with a 0.04 m radius high conductivity area) as it approaches the border. Once again the streak artifacts become increasingly more evident as the phantom becomes closer to the border because the isopotential lines from each injection pattern tend to “close” through the electrodes near the phantom. This overlap causes an artificial increase of admittivity between the phantom and the border elongating the reconstruction. Finally, Figures 4.11(g), 4.11(h), and 4.11(i) intend to show the reconstruction result of several geometries within the phantom. It is clear the influence of the isopotentials arcs in the reconstructed images, with a tendency to reconstruct all objects as circles or with round edges. This is most evident in the quasi-symmetrical ellipse and in the square phantom reconstructions.

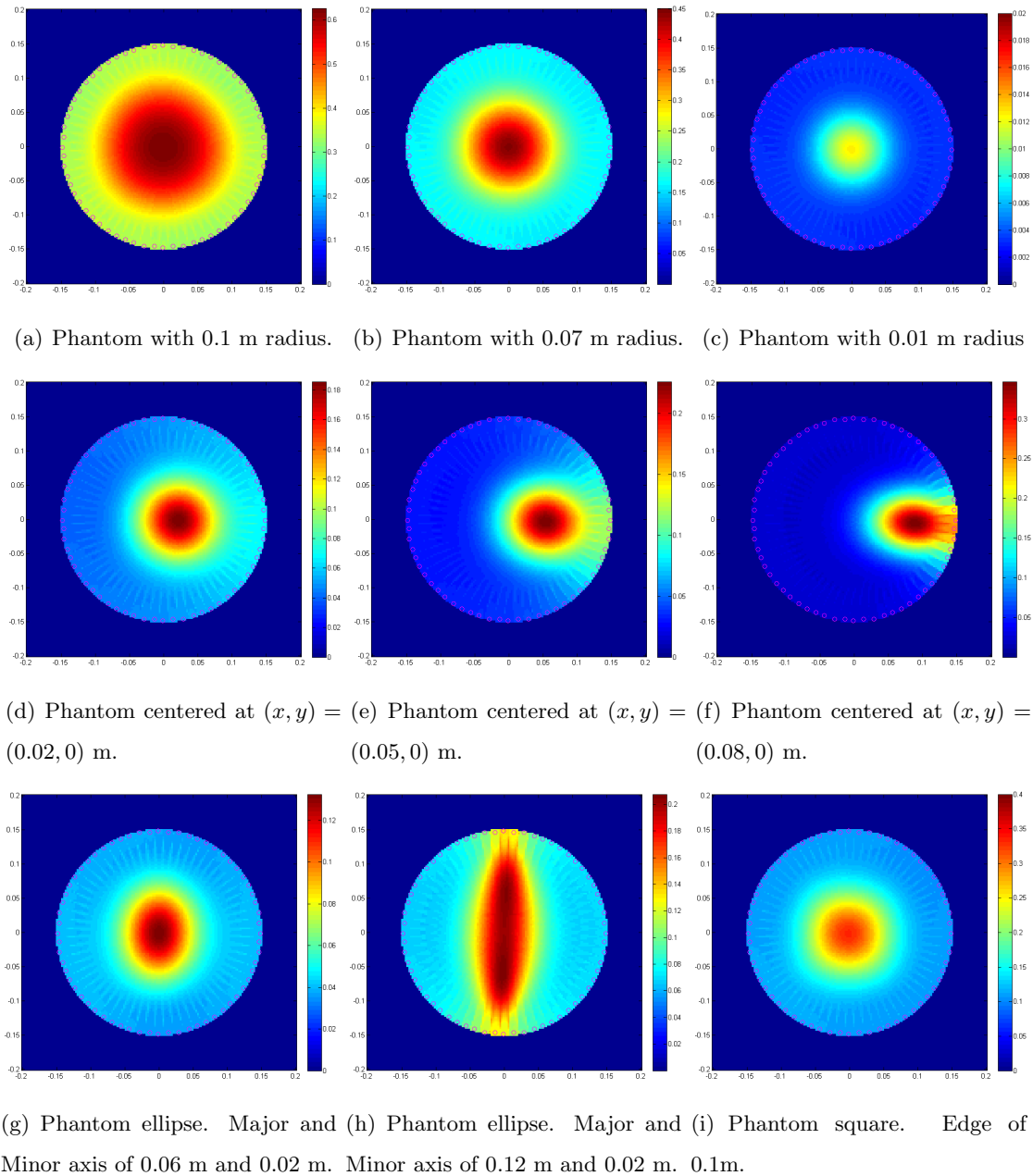


Figure 4.11: Backprojection reconstruction with different phantom sizes, placement and geometries. Colorbar in V/V

Some studies, like Nebuya et al. [2006] or Graham and Adler [2007], have shown the importance of electrode placement to increase the reconstruction accuracy. Victorino et al. [2004] was the first to propose a new set of electrodes placement to decrease the reconstruction error. In fact, the reconstruction of near boundary structures with greater anatomic and physiologic importance is increased if the electrodes in that boundary region are placed with higher density. This method is of most value in the cases that a low number of electrodes is imposed by a limited hardware capacity. Figure 4.12 depicts a reconstruction of a circular phantom with regularly spaced, randomly spaced and methodically spaced electrodes.

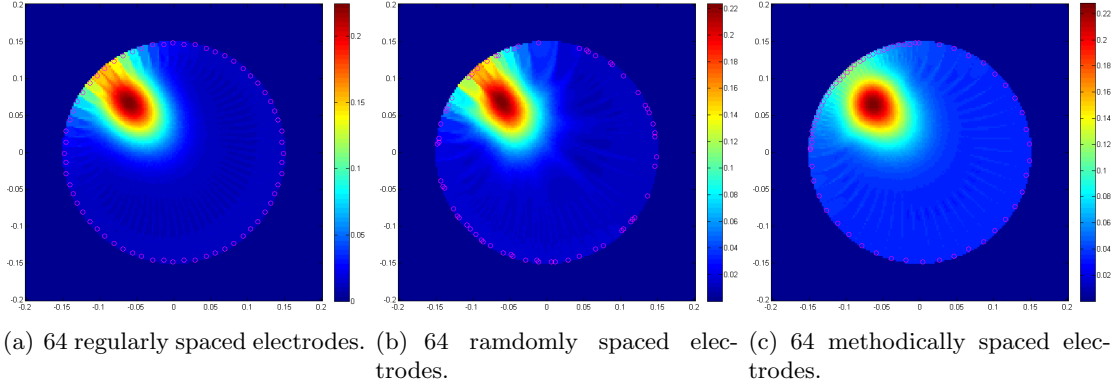


Figure 4.12: Backprojection reconstruction of circular phantom with 0.03 m and centered at $(x, y) = (-0.06, 0.06)$ m. Colorbar in V/V.

The following results correspond to image reconstruction of several phantoms with two areas with increased/decreased conductivity relative to the body within the electrodes. In Figure 4.13(a) the original image with two areas with equal conductivity is portrait and below the respective reconstruction result. In the central images the same phantom is used but in this case the two areas possess different conductivities but higher than the body (Figure 4.13(b)). Finally on the right (Figure 4.13(c)), one area has higher conductivity and the other lower conductivity when compared with the body within the electrodes.

This array of images shown evidence of a limitation in the EIT imaging technique when compared, for instance, with CT. Unlike other imaging modalities where each radiation beam is independent from its neighbors the same is not verified in EIT. Meaning that when an area of increased conductivity is present within the body there is a tendency for the electric field lines to direct themselves to that area, and by doing so decreasing the image contrast for the remaining phantom. This effect is visible in Figure 4.14 where a CT projection (on the left) is compared with an EIT projection (on the right) of the same phantom.

The last phantom presented in this section was built with a more complex conductivity distribution map to study thorax imaging with the backprojection algorithm. Several elliptical domains were used to represent the lungs, heart and spinal column and the admittivities assigned to them were intended to simulate tissues within the body (see Table 2.1). The original conductivity map is presented in Figure 4.15(a) and the reconstruction result in (b).

In the reconstruction is clear the presence of all four structures with the correct conductivity relation between them. However, and as it was visible in all previous examples, the blurring effect makes it impossible to distinguish between structure borders. To decrease this effect the filtered backprojection algorithm was studied (see Appendix A).

Filtered backprojection algorithm consists in the convolution, in time, of each one-dimensional

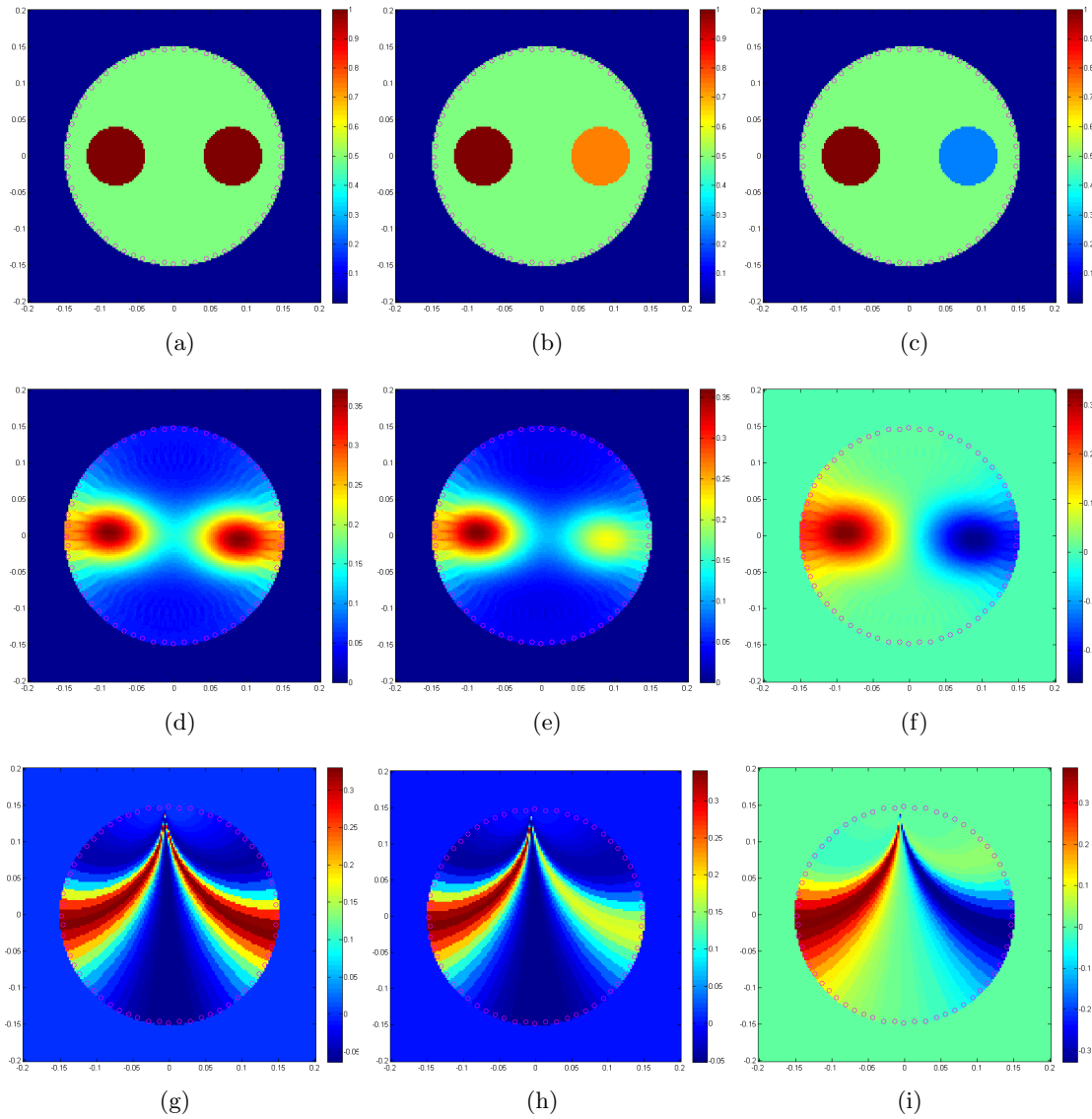


Figure 4.13: Backprojection reconstruction of multiple conductivity phantoms. (a),(b) and (c) are conductivity maps. (d),(e) and (f) are the reconstruction result. (g),(h) and (j) are single projections in the backprojection algorithm. Colorbar of all Figures in V/V.

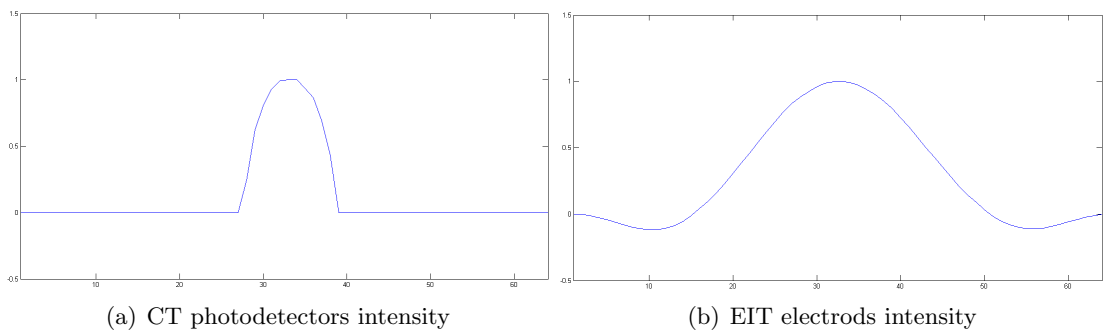


Figure 4.14: Normalized plots for one projection of a circular phantom.

projection with the $1/r$ blurring factor to remove the intensity of the backprojection image rolls. This is performed in the frequency space by multiplication of each projection Fast fourier trans-

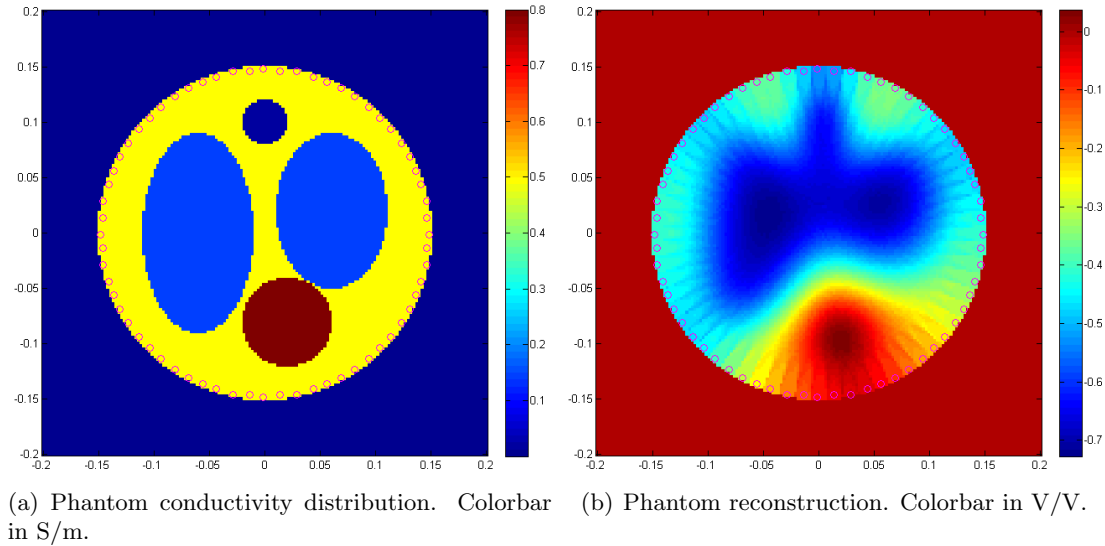


Figure 4.15: Backprojection image reconstruction from a phantom of a thorax.

form (FFT) by a ramp filter that consists in the FFT of the $1/r$ blurring effect.

In first-generation CT imaging technique the FFT of each intensity recorded at the array of photodetectors is performed without any issue because these sensors are placed equidistantly in the projection axis. However the same is not verified in the newer generation CT scanners (like Fan-beam scanners) or for that matter in the EIT, and so a space transformation is required before an FFT can be applied.

Recalling Section 4.2.2, a space transformation is already being used to create a Cartesian coordinate system for the isopotential lines. Hence, this transformation may also be used to transform the electrodes coordinates at the phantom border into a linear space and ultimately allowing for a FFT of each projection. Because this transformation does not produce equidistant points in the new space (see Figure 4.6(b)) the data must be oversampled. Since the electrodes coordinates in the Möbius space has an infinite period one may use any oversampling factor without violating the Nyquist theorem.

The filtered backprojection method, in CT, works by assigning negative attenuation values to the radiation beams at transition places within the phantom, reducing the $1/r$ blurring effect induced in the backprojected image. However, in CT imaging technique the high number of photodetectors allows some degree of projection data manipulation without compromising the end reconstruction. But in EIT technique the low number of electrodes is directly proportional to the signal resolution which means that this manipulation may yield incorrect image reconstructions. This limitation is surpassed by a computational increase in the number of isopotentials. This way some of the isopotentials may be assigned the necessary scalar potential value to correct the overall blurring effect.

In the following set of Figures the results of multiple type filters in the filtered backprojection algorithm are presented.

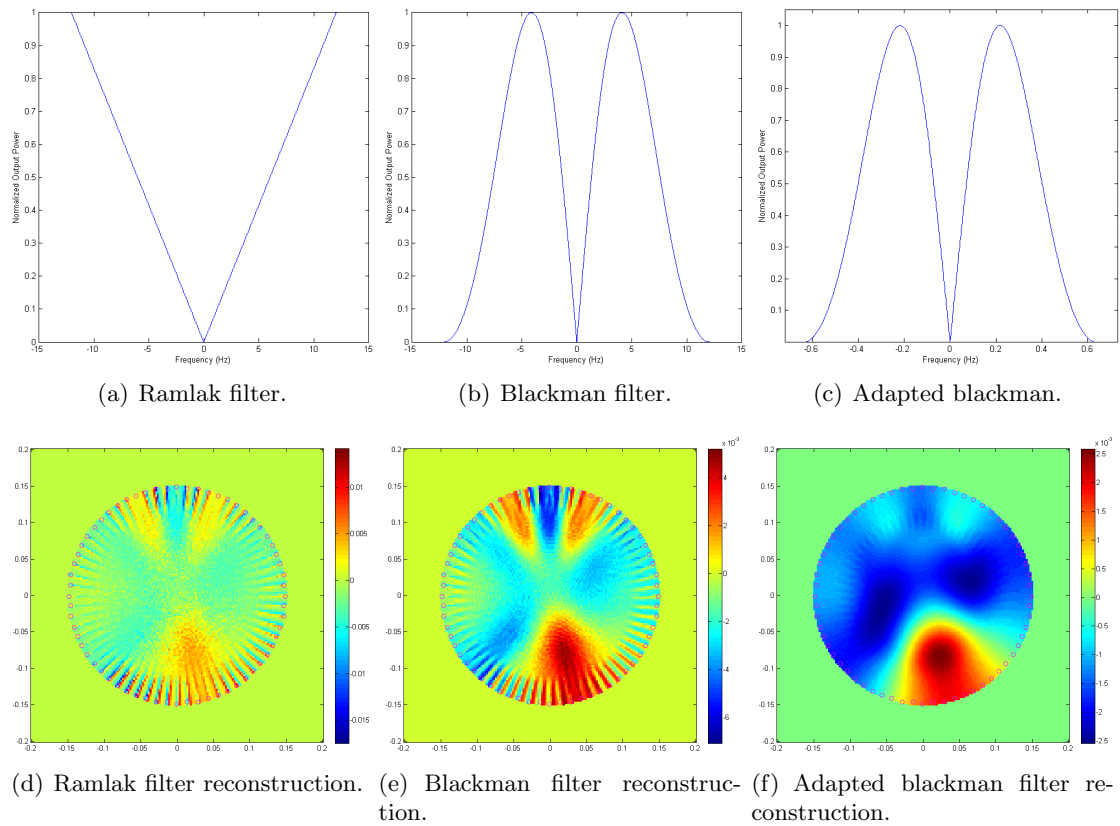


Figure 4.16: Filtered Backprojection reconstruction of phantom in Figure 4.15(a).

As expected and viewed in the spectral analysis of one EIT projection (Figure 4.17) the signal is composed of small frequency components due to the isopotentials geometry and the low number of electrodes. For this reason both standard *Ramlak* and *Blackman* filters performed

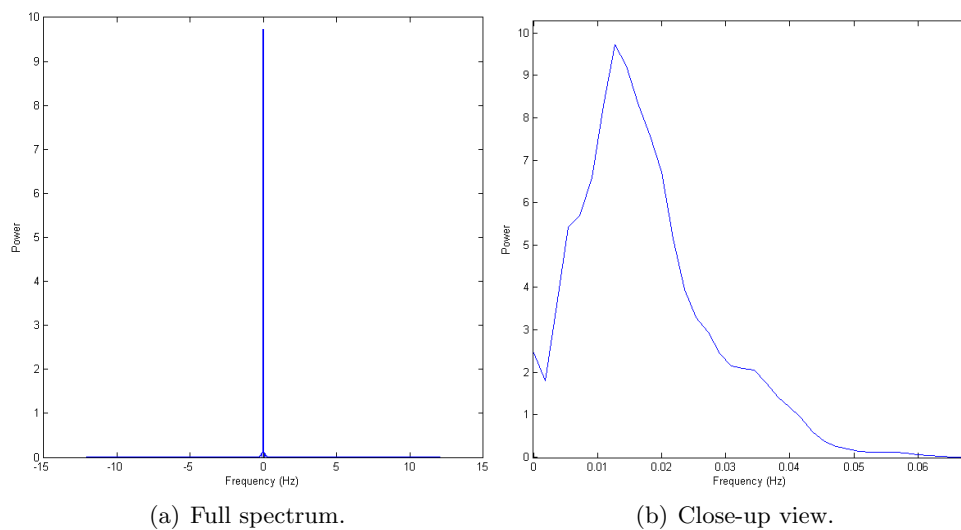


Figure 4.17: Spectral analysis of one projection of phantom in Figure 4.15(a).

poorly in the reconstruction algorithm because of the low frequency components attenuation when compared with the high frequency signal present in the data. With this in mind an adaptation to the *Blackman* filter was made to reduce the high frequency signals influence in the reconstruction. This yielded a result where all four thorax components are better distinguished between them but with some level of geometry distortion when compared with the original image.

4.4.2 Discussion

The software implemented to gather the input data for the 2D reconstruction problem used FIT to discretize the bounded space and allow the construction of a linear system of equations. Due to the system dimension the equations were implemented using sparse matrices and solved with $x = A^{-1}b$ method. This method was chosen for its implementation simplicity, however more robust methods may be applied with already available methods (like iterative Krylov, Tikhonov regularization or Biconjugate Gradient stabilized methods). Still in regard to the software, it is based on the dual grid method and besides the information regarding the geometry and physical properties of the problem the mesh generation, neighbor matrices and the system of equations are computed automatically to meet the user's specifications. This independence of software on the user is useful to enable quick changes in the mesh, charge protocol, admittivity maps, etc while obtaining useful and reliable results to test prototypes or EIT configurations.

Despite the simplifications that were done on the software implementation of the forward model, the results obtained in the reconstructed images are in accordance with the real admittivity distribution within the space. However, these same results show that there is still room for improvement. For instance, whilst the phantom position within the mesh is correctly predicted by the reconstruction algorithm its size and geometry suffers for some inaccuracy. This imprecision errors are mainly due to the low number of electrodes and their placement at the border (as seen in Figures 4.10 and 4.12(c)) and the isopotential lines large area of influence and their geometry. Despite small enhancement using the filtered backprojection reconstruction method when compared with the simple backprojection, both these linear methods fall short when compared with existent iterative and non-linear algorithms either in phantom geometry reconstruction and in conductivity distribution. And so, these results should only be considered as an non-calibrated indication of the material property distribution within the space between the electrodes and used as an excellent first approximation to non-linear methods.

4.5 3D Image Reconstruction

In this section the computational mesh developed for the simulation of the EIT forward problem was based on a CT scan of a male subject with 55 years old. Each CT slice was segmented, in a partitioning process to divide each slice into a set of five different regions. This regions consisted in: Lung, Bone, Cardiac Muscle and Skeletal Muscle tissue and Blood. This segmentation was intended to simplify the CT scan into a more meaningful and easier to analyze model. The focus of the simulation is to test the backprojection algorithm in a 3D thorax model. This mesh, subjected to refinements in the air to skin transition and in the heart region (as seen in Figure 4.18), presented an $N_c = 89370$, a size of $[x, y, z] = [0.40, 0.45, 0.15]$ m centered at the origin, a coarser element with $L_c = 0.01$ m and the finer element with $L_c = 0.005$ m.

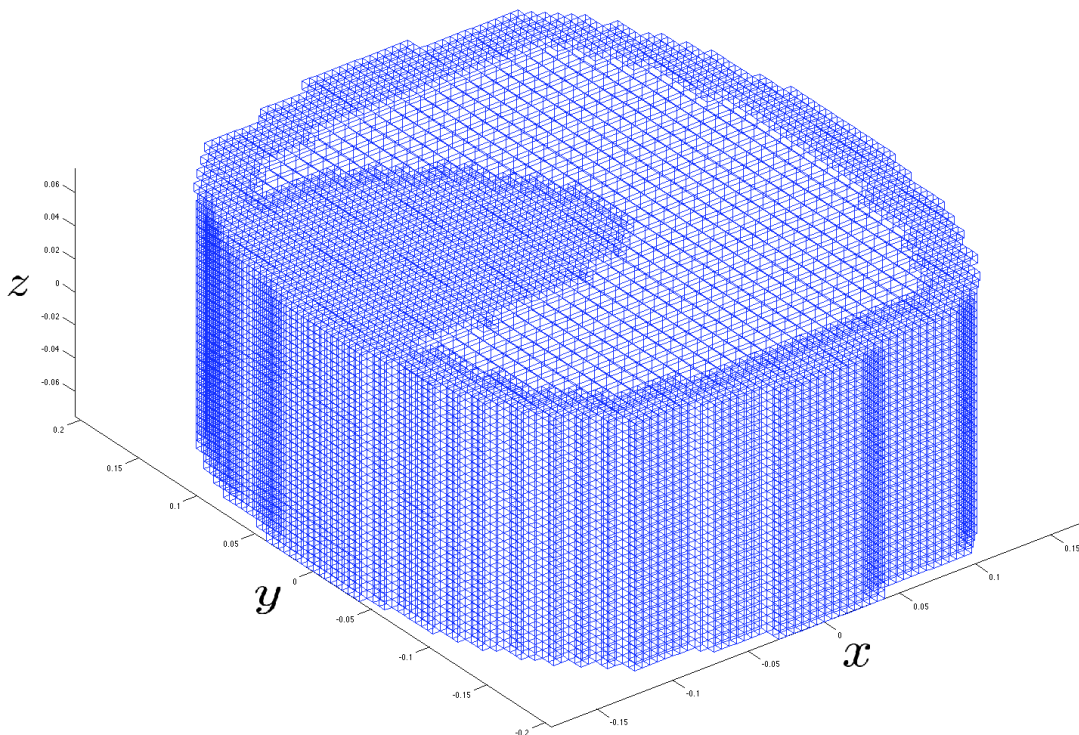
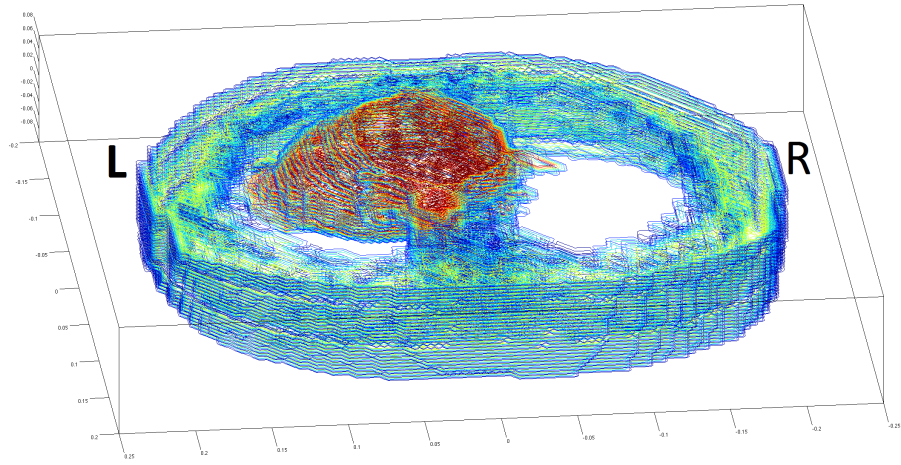
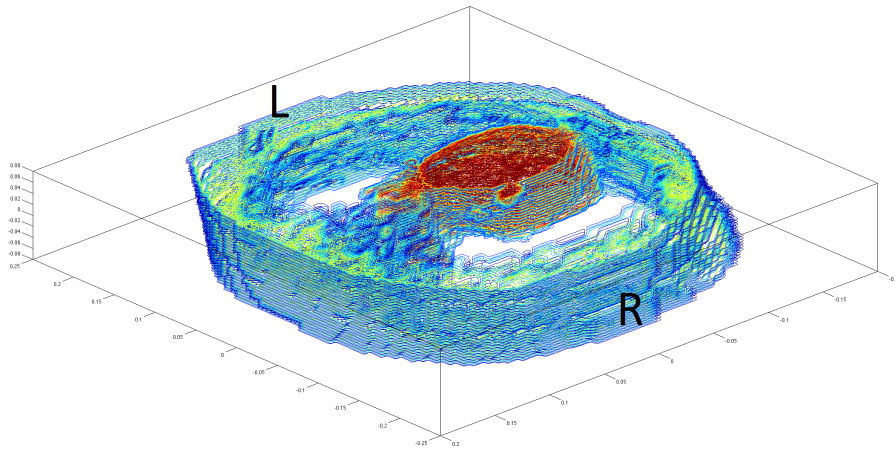


Figure 4.18: 3D mesh used to construct the thorax model. Axis in m

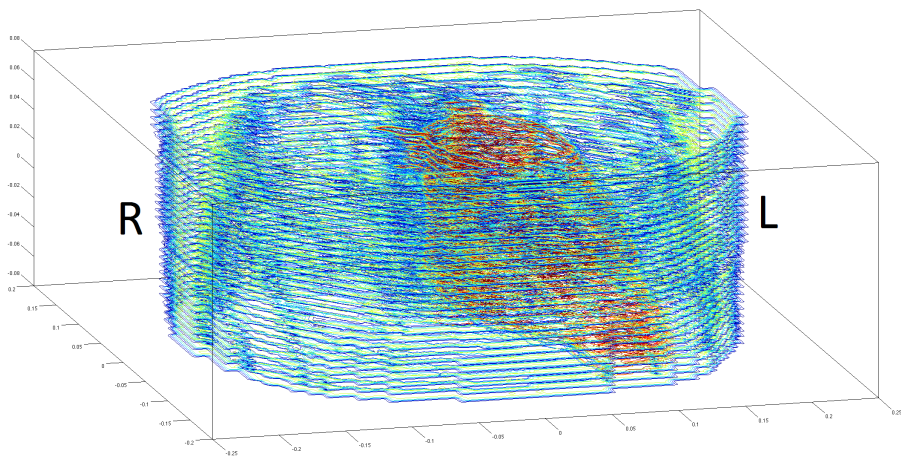
The segmentation result from the CT-scan can be seen in Figure 4.19.



(a) Posterior view.



(b) Lateral-Posterior view.



(c) Anterior view.

Figure 4.19: 3D Segmentation from CT-scan. Thorax transverse cut. Axis in m

4.5.1 Results

The results of the backprojection algorithm in a 3D thorax model were obtained in a similar way as the one described in Section 4.4. But unlike the 2D case, here a substantial approximation was needed to implement in order to accomplish the intended objective.

Because of the geometrical form of the isopotential lines, 2D circumference arcs, it is not possible to place the electrodes in the thorax (forming a sphere) in a way that there are no possible escape paths between the drive and receiver pair of electrodes. For this reason, the isopotential line calculation as described in Section 4.2 would yield several pixels, increasing in number as they approximate the abdominal cavity and the cervical region, without any electrical scalar potential value assigned from the distribution measured at the electrodes position.

Because of this, a choice was made to reconstruct the 3D thorax impedance model in a similar way to the CT-scan, where multiple 2D planes are reconstructed and later assembled in the final 3D model reconstruction.

The last approximation required for the 3D reconstruction was due to the physical limitation of the electrode size and the current electronic devices capability to acquire, discretize and process the electrical scalar potential obtained at each receiver pair. And so, a set of 12 slices, each with 64 electrodes, were chosen to accommodate all the 768 electrodes.

The distribution of these slices can be seen in Figure 4.20. The slices in which the electrodes were placed were chosen in order to obtain a better resolution in the central zone of the mesh (where the heart is located) and decreasing in space as one approximates the mesh Z- boundary. The remaining slices, where no electrodes are found, were reconstructed via interpolation from the closest 2 pair of electrodes.

The results obtained with the backprojection algorithm for the 3D thorax reconstruction are presented in Figures 4.21(a) and 4.21(b).

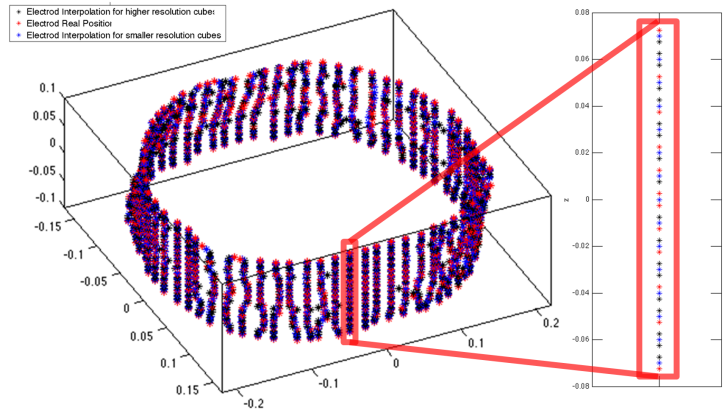
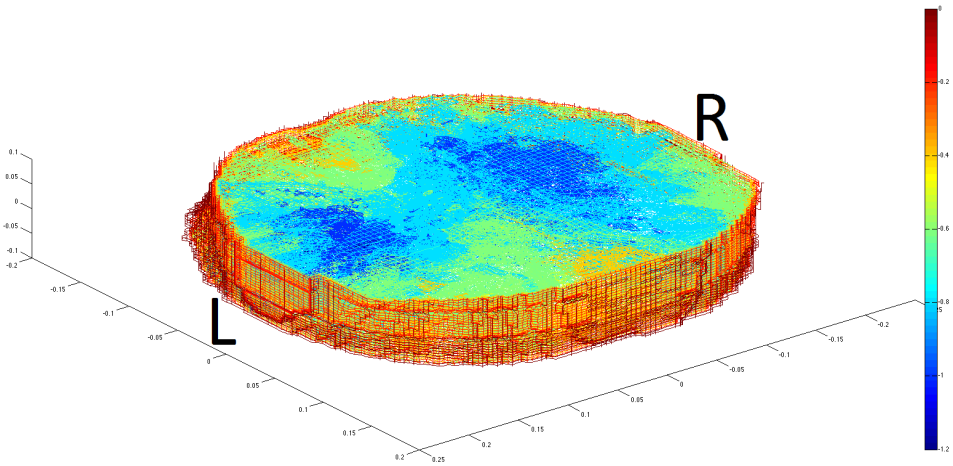
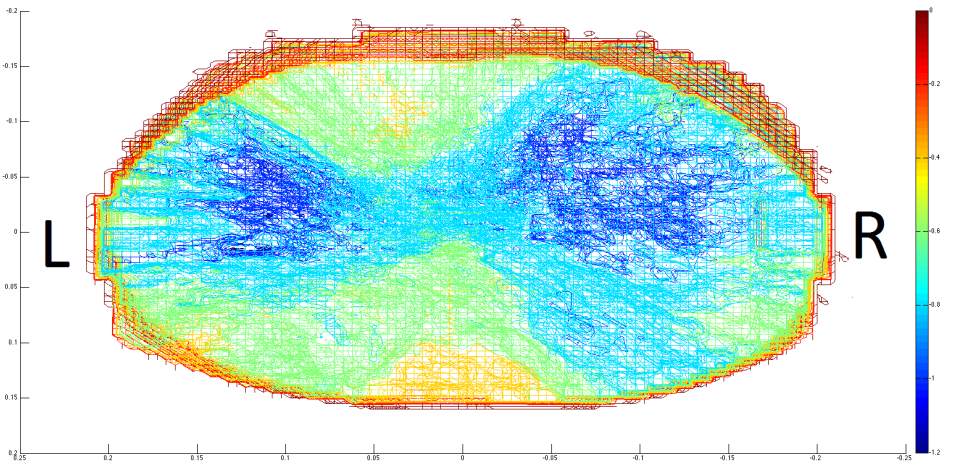


Figure 4.20: 3D electrodes distribution in the thorax. On the right is a close-up view of one vertical line of electrodes.



(a) Lateral-Posterior view. Colorbar in V/V.



(b) Superior view. Colorbar in V/V.

Figure 4.21: 3D Backprojection results for thorax impedance imaging. Axis in m

4.5.2 Discussion

After the image segmentation, and similarly to the 2D case, a software was developed and implemented to gather the input data for the 3D reconstruction problem using FIT. Due to the space dimension the system of equations were solved with the $x = A^{-1}b$ method.

Despite the simplifications that were done on the software implementation of the inverse model, in particular the limited number of electrodes and the CT-like reconstruction, the results obtained in the reconstructed images are in accordance with the impedance of the segmented image but lack the resolution required to make a clear distinction between tissues frontiers and proving, once again, that there is still room for improvement. For instance, whilst the lungs position within the chest and their relative size is correctly reconstructed, the number of artifacts due to the backprojection method and the grid variable resolution make it impossible to reconstruct small volume tissues like the heart blood chambers or the spine column.

As stated previously, these results should only be considered as a non-calibrated and approximate tissue distribution within the thorax or as an excellent first approximation to non-linear methods.

Chapter 5

Conclusions and Future Developments

Throughout this thesis two problems were tackled with computational electromagnetic models (the forward problem and the inverse problem) and each of the bounded space was successfully discretized to explore Electric Impedance Tomography imaging modality in 2D and 3D.

Based on FIT, a software was designed to generate an octree type variable resolution mesh in a way that it allows a concentration of increased resolution cells solely where they are needed (like the air-skin interface or the heart region) thus saving time to perform the discretization of the domain and solve the forward problem. Given the mesh generation, as well as all other developed software, is automatic in the sense that it only requires an input regarding the problem geometry and its physical parameters (number of electrodes and position, for instance) it is possible to perform quick changes in the computerized problem to predict real prototypes behavior before their development.

To measure the proximity of FIT and generated mesh behavior when compared with problems with known results a set of tests were implemented. These yielded no major discrepancies between the simulation environment and the real physics involved besides some discretization errors that, as proven, decrease as the mesh was increasingly discretized. And so, the accuracy of the developed computer model was proven accurate for the intended use, the imaging of tissues using differences in the electromagnetic tissue properties.

Having established the correct modeling of the physics involved, a set of 2D phantoms were proposed to assess the reconstruction method behavior, in particular the obtained artifacts due to the phantom material properties (location, magnitude and geometry), number of electrodes and their distribution within the phantom border. In the end, and as proposed in this thesis, a software was developed to reconstruct the thorax internal electromagnetic properties from

an CT-scan. In both inverse problems, solved using the Back-Projection and Filtered Back-Projection linear techniques, it was found that despite their serious limitations when more complex distributions with multiple material properties are present they performed very well for objects with simple conductivity distributions leading to the main conclusion that Back-Projection EIT should only be used to approximate tissue distribution within the thorax or as an excellent first approximation to non-linear methods.

Other important aspect that still needs development is the reproducibility of measurements not only between patients but between measurements in the same patient as well. This variability arises because the calibration for every imaging reconstruction is made using a reference data set consisting in a measurement of a homogeneous field. But this, is not viable for in vivo reconstructions, and it may be that the mismatch between the measured data and the predictions from the forward model is dominated by the errors in electrode position, boundary shape and contact impedance rather than interior conductivity. And this difficulty leads to problems in establishing a basal criteria or reference value for particular measurement results. This happens because the scatter data results from problems like electrode polarization, individual variability (the mesh used for each individual should be personalized for better results).

Although EIT presents some obstacles in the way to become a common practice in clinical imaging, its capacity to perform real time monitoring in patients or assist in medical guidance during small area surgeries (like the brain) allows an optimistic conclusion as far as the clinical perspective for EIT in the near future.

Looking back one can conclude that the objectives for this thesis were successfully accomplished, allowing the author to come in contact with the state of the art of a promising imaging technology and opening up new perspectives of research in one of the most challenging fields in medical and engineering common grounds. It is exactly the fact that some aspects may be second nature for some professionals and other completely incomprehensible is a major hurdle for EIT that may have been in the way of its establishment in the clinical environment.

Bibliography

- Y. A Moshkovitz, E. A Kaluski, O. A Milo, Z. A Vered, and G. A Cotter. Recent developments in cardiac output determination by bioimpedance: comparison with invasive cardiac output and potential cardiovascular applications. *Current Opinion in Cardiology*, 19(3):229–237, 2004.
- P. D. Alberto Yufera, Alberto Olmo and D. Canete. *Cell Biometrics Based on Bio-Impedance Measurements, Advanced Biometric Technologies*. Dr. Girija Chetty, 2011. ISBN:978-953-307-487-0.
- D. N. Arnold and J. Rogness. Möbius transformations revealed. *Notices Amer. Math. Soc.*, 55: 1226–1231, 2008.
- S. I. Babic and C. Akyel. An improvement in the calculation of the magnetic field for an arbitrary geometry coil with rectangular cross section. *International Journal of Numerical Modelling: Electronic Networks, Devices and Fields*, 18(6):493–504, 2005.
- N. B. Bandeira. *Magnetic Induction Tomography - New Approaches Towards a Higher Resolution Biomedical Imaging System*. Doctoral program in electrical and computer engineering, Instituto Superior Técnico. Universidade Técnica de Lisboa, 2009.
- D. C. Barber and B. H. Brown. Recent developments in applied potential tomography-apt. In S. Bacharach, editor, *Information Processing in Medical Imaging*, pages 106–121. Springer Netherlands, 1986. ISBN 978-94-010-8392-8.
- S. Barbieri, M. Cavinato, and M. Giliberti. An educational path for the magnetic vector potential and its physical implications. *European Journal of Physics*, 34(5):1209, 2013.
- A. Benabid, L. Balme, J. Persat, M. Belleville, J. Chirossel, M. Buyle-Bodin, J. de Rougemont, and C. Poupot. Electrical impedance brain scanner: principles and preliminary results of simulation. *TIT J Life Sci*, 8(1-2):59–68, 1978.
- N. B. Bras, R. C. Martins, A. C. Serra, and A. L. Ribeiro. A fast forward problem solver for

- the reconstruction of biological maps in magnetic induction tomography. *Magnetics, IEEE Transactions on*, 46(5):1193–1202, May 2010.
- B. Brown and A. Seagar. The sheffield data collection system. *Clinical Physics and Physiological Measurements*, 8:91–97, 1987.
- J. Caeiros. Electromagnetic tomography: Real-time imaging using linear approaches. Master’s degree in biomedical engineering, Instituto Superior Técnico. Universidade Técnica de Lisboa, 2010.
- M. Clemens and T. Weiland. Numerical algorithms for the fdt and fdf simulation of slowly varying electromagnetic fields. *International Journal of Numerical Modelling: Electronic Networks, Devices and Fields*, 12(1-2):3–22, 1999.
- M. Clemens and T. Weiland. Discrete electromagnetism with the finite integration technique. *Progress in Electromagnetics Research*, 32:65–87, 2001.
- D. Das, F. A. Kamil, K. Biswas, and S. Das. Evaluation of single cell electrical parameters from bioimpedance of a cell suspension. *RSC Adv.*, 4:18178–18185, 2014. doi: 10.1039/C4RA00400K.
- B. M. Eyuboglu, B. H. Brown, D. C. Barber, and A. D. Seager. Localisation of cardiac related impedance changes in the thorax. *Physiol. Meas.*, 8(A):167–73, 1987.
- R. P. Fedorenko. A relaxation method for solving elliptic difference equations. *{USSR} Computational Mathematics and Mathematical Physics*, 1(4):1092–1096”, 1962.
- I. Frerichs, J. Hinz, P. Herrmann, G. Weisser, G. Hahn, T. Dudykevych, M. Quintel, and G. Hellige. Detection of local lung air content by electrical impedance tomography compared with electron beam ct. *Journal of Applied Physiology*, 93(2):660–666, 2002.
- I. S. Gabashvili and G. S. Snider. Book review: Introduction to biomedical imaging, by andrew webb. *Annals of Biomedical Engineering*, 31(11):1443–1443, 2003. ISSN 0090-6964.
- B. M. Graham and A. Adler. Electrode placement configurations for 3d eit. *Physiological Measurement*, 28(7):S29, 2007.
- B. Grychtol, W. R. B. Lionheart, M. Bodenstern, G. Wolf, and A. Adler. Impact of model shape mismatch on reconstruction quality in electrical impedance tomography. *Medical Imaging, IEEE Transactions on*, 31(9):1754–1760, Sept 2012.

- E. Haber and U. M. Ascher. Fast finite volume simulation of 3d electromagnetic problems with highly discontinuous coefficients. *SIAM J. Scient. Comput.*, 22:1943–1961, 2001.
- E. Haber and S. Heldmann. An octree multigrid method for quasi-static maxwell’s equations with highly discontinuous coefficients. *J. Comput. Phys.*, 223(2):783–796, May 2007.
- G. Hahn, A. Just, T. Dudykevych, I. Frerichs, J. Hinz, M. Quintel, and G. Hellige. Imaging pathologic pulmonary air and fluid accumulation by functional and absolute eit. *Physiological Measurement*, 27(5):S187, 2006.
- R. J. Halter, A. R. Schned, J. A. Heaney, and A. Hartov. Passive bioelectrical properties for assessing high- and low-grade prostate adenocarcinoma. *The Prostate*, 71(16):1759–1767, 2011. ISSN 1097-0045.
- P. Hasgall, E. Neufeld, M. Gosselin, A. Klingenböck, and N. Kuster. IT’IS database for thermal and electromagnetic parameters of biological tissues, Version 2.5, August 1st 2014. URL www.itis.ethz.ch/database. [Online; accessed 26-August-2014].
- R. P. Henderson and J. Webster. An impedance camera for spatially specific measurements of the thorax. *Biomedical Engineering, IEEE Transactions on*, BME-25(3):250–254, May 1978.
- J. Hinz, P. Neumann, T. Dudykevych, L. G. Andersson, H. Wrigge, H. Burchardi, and G. Hedenstierna. Regional ventilation by electrical impedance tomography: A comparison with ventilation scintigraphy in pigs. *Chest*, 124(1):314–322, 2003.
- A. E. Hoetink, T. J. C. Faes, J. T. Marcus, H. J. J. Kerckamp, and R. M. Heethaar. Imaging of thoracic blood volume changes during the heart cycle with electrical impedance using a linear spot-electrode array. *Medical Imaging, IEEE Transactions on*, 21(6):653–661, June 2002. ISSN 0278-0062.
- D. S. Holder, editor. *Electrical Impedance Tomography, methods, history and applications*. Institute of Physics Publishing, 2005. ISBN:0-7503-0952-0.
- D. Jodorkovsky, J. Price, B. Kim, S. Dhalla, E. Stein, and J. Clarke. Multichannel intraluminal impedance-ph testing is clinically useful in the management of patients with gastroesophageal reflux symptoms. *Digestive Diseases and Sciences*, pages 1–6, 2014.
- R. Landaeta, O. Casas, and R. Pallas-Areny. Heart rate detection from plantar bioimpedance measurements. In *Engineering in Medicine and Biology Society, 2006. EMBS ’06. 28th Annual International Conference of the IEEE*, pages 5113–5116, Aug 2006.

- S. Leonhardt, A. Cordes, H. Plewa, R. Pikkemaat, I. Soljanik, K. Moehring, H. J. Gerner, and R. Rupp. Electric impedance tomography for monitoring volume and size of the urinary bladder. *Biomedizinische Technik*, 56(6):301–307, 2011.
- Y.-Y. Lu, J.-J. Huang, Y.-J. Huang, and K.-S. Cheng. Cell growth characterization using multi-electrode bioimpedance spectroscopy. *Measurement Science and Technology*, 24(3):035701, 2013.
- J. C. Maxwell. *A Treatise on Electricity and Magnetism*. Clarendon Press (Oxford), 1873.
- M. Michalikova and M. Prauzek. A hybrid device for electrical impedance tomography and bioelectrical impedance spectroscopy measurement. In *Electrical and Computer Engineering (CCECE), 2014 IEEE 27th Canadian Conference on*, pages 1–4, May 2014.
- W. Müller, J. Krueger, A. Jacobus, R. Winz, T. Weiland, H. Euler, U. Hamm, and W. R. Novender. Numerical solution of 2- or 3-dimensional nonlinear field problems by means of the computer program profi. *Archiv für Elektrotechnik*, 65(4-5):299–307, 1982. ISSN 0003-9039.
- I. Munteanu and T. Weiland. Rf and microwave simulation with the finite integration technique - from component to system design. In G. Ciuprina and D. Ioan, editors, *Scientific Computing in Electrical Engineering*, volume 11 of *Mathematics in Industry*, pages 247–260. Springer Berlin Heidelberg, 2007. ISBN 978-3-540-71979-3.
- D. Murphy, P. Burton, R. Coombs, L. Tarassenko, and P. Rolfe. Impedance imaging in the newborn. *Clinical Physics and Physiological Measurement*, 8(4A):131, 1987.
- S. Nebuya, M. Noshiro, A. Yonemoto, S. Tateno, B. H. Brown, R. H. Smallwood, and P. Milnes. Study of the optimum level of electrode placement for the evaluation of absolute lung resistivity with the mk3.5 eit system. *Physiological Measurement*, 27(5):S129, 2006.
- W. L. Oberkampf and T. G. Trucano. Guide for the verification and validation of computational fluid dynamics simulations. *Progress in Aerospace Sciences*, SAND2002 - 0529, Mar 2002.
- F. Podczeck, C. L. Mitchell, J. M. Newton, D. Evans, and M. B. Short. The gastric emptying of food as measured by gamma-scintigraphy and electrical impedance tomography (eit) and its influence on the gastric emptying of tablets of different dimensions. *Journal of Pharmacy and Pharmacology*, 59(11):1527–1536, 2007.
- O. Podebrad, M. Clemens, and T. Weiland. New flexible subgridding scheme for the finite integration technique. *Magnetics, IEEE Transactions on*, 39(3):1662–1665, May 2003.

- M. Proença, F. Braun, M. Rapin, J. Solà, A. Adler, B. Grychtol, M. Bühner, P. Krammer, S. H. Bohm, M. Lemay, and J. Thiran. Influence of heart motion on eit-based stroke volume estimation. In A. Adler and B. Grychtol, editors, *Proceedings of the 15th International Conference on Biomedical Applications of ELECTRICAL IMPEDANCE TOMOGRAPHY*, 2014.
- J. Richard, C. Pouzot, A. Gros, C. Tourevieille, D. Lebars, F. Lavenne, I. Frerichs, and C. Guerin. Electrical impedance tomography compared to positron emission tomography for the measurement of regional lung ventilation: an experimental study. *Critical Care*, 13(3):R82, 2009.
- B. Rosa. *Electromagnetic Tomography with application in the volume monitoring of fluids contained in biological cavities*. Doctoral program in electrical and computer engineering, Instituto Superior Técnico. Universidade Técnica de Lisboa, 2014.
- F. Santosa and M. Vogelius. A backprojection algorithm for electrical impedance imaging. *SIAM Journal on Applied Mathematics*, 50(1):216–243, 1990.
- H. Schwan. Biological effects of non-ionizing radiations: Cellular properties and interactions. *Annals of Biomedical Engineering*, 16(3):245–263, 1988.
- D. Siroopol, S. Hogas, L. Voroneanu, M. Onofriescu, M. Apetrii, M. Oleniuc, M. Moscalu, R. Sascau, and A. Covic. Predicting mortality in haemodialysis patients: a comparison between lung ultrasonography, bioimpedance data and echocardiography parameters. *Nephrology Dialysis Transplantation*, 28(11):2851–2859, 2013.
- E. Teschner and M. Imhoff. Electrical impedance tomography: the realization of regional ventilation monitoring. Dräger Medical GmbH, 2011.
- A. T. Tidswell, A. Gibson, R. H. Bayford, and H. D. S. Three-dimensional impedance tomography of human brain activity. *Neuroimage*, 13:283–294, 2001.
- A. T. Tidswell, A. P. Bagshaw, D. S. Holder, R. J. Yerworth, L. Eadie, S. Murray, L. Morgan, and R. H. Bayford. A comparison of headnet electrode arrays for electrical impedance tomography of the human head. *Physiol. Meas.*, 24:527–544, 2003.
- E. Tonti. On the geometrical structure of electromagnetism. In G. Ferrarese, editor, *Gravitation, Electromagnetism and Geometrical Structures*, pages 281–308. Pitagora Editrice Bologna, 1996.
- O. V. Trokhanova, M. B. Okhapkin, and A. V. Korjenevsky. Dual-frequency electrical impedance mammography for the diagnosis of non-malignant breast disease. *Physiological Measurement*, 29(6):S331, 2008.

- B. M. W. Tsui and E. C. Frey. Analytic image reconstruction methods in emission computed tomography. In H. Zaidi, editor, *Quantitative Analysis in Nuclear Medicine Imaging*, pages 82–106. Springer US, 2006. ISBN 978-0-387-23854-8.
- A. Victorino, B. Borges, N. Okamoto, J. Matos, R. Tucci, R. Caramez, H. Tanaka, S. Sipmann, V. Santos, B. ans Barbas, R. Carvalho, and P. Amato. Imbalances in regional lung ventilation. *American Journal of Respiratory and Critical Care Medicine*, 169(7):791–800, 2004.
- T. Weiland. A discretization model for the solution of maxwell’s equations for six-component fields. *Electronics and Communications (AEU)*, 31:116–120, mar 1977.
- T. Weiland. Lossy waveguides with arbitrary boundary contour and material distribution. *Archiv Elektronik und Uebertragungstechnik*, 33:170–174, apr 1979.
- C. Weinhold, H. Reichenspurner, P. Fulle, G. Nollert, and B. Reichart. Registration of thoracic electrical bioimpedance for early diagnosis of rejection after heart transplantation. *The Journal of Heart and Lung transplantation*, 12(5):832–836, 1993.
- R. J. Yerworth, R. H. Bayford, B. Brown, P. Milnes, M. Conway, and D. S. Holder. Electrical impedance tomography spectroscopy (eits) for human head imaging. *Physiol. Meas.*, 24:477–489, 2003.
- M. Yusof. Electrical impedance tomography (eit) in breast cancer screening. Health Technology Assessment Section (MaHTAS), Medical Development Division, Ministry of Health Malaysia, 2009.
- S. Zlochiver, M. Arad, M. M. Radai, D. Barak-Shinar, H. Krief, T. Engelman, , R. Ben-Yehuda, A. Adunsky, and S. Abboud. A portable bio-impedance system for monitoring lung resistivity. *Medical Engineering and Physics*, 29(1):93–100, 2006.

Appendix A

Filtered Backprojection Algorithm

In this Appendix the Backprojection Algorithm, with particular attention to the Filtered Backprojection process, for image reconstruction is tackled. Due to the historical relevance of this linear method in biomedical imaging systems and the fact that it was briefly approached in this thesis, the author saw fit to formulate here this technique in more detail.

As stated in Chapter 4, the backprojection reconstruction process consists in the overlapping of one-dimensional projection, $P_\phi(r)$, acquired at different angles (ϕ), as seen in Figure 4.1. Each projection is then equally divided for all elements in the radiation path and this process is repeated for all of the different angle projections. Recalling Equation 4.2:

$$\hat{f}(x, y) = \sum_{j=1}^n P_{\phi_j}(r) d\phi \quad (\text{A.1})$$

Because of the artifacts associated with the simple backprojection this method was deprecated. In its place a method able to reduce these artifacts is used, named filtered backprojection, that consists in applying a filter to each projection before the end summation.

This filter arises from the mathematical relation between the backprojected image and the real image. Starting from the integral form of Equation A.2, one gets:

$$\hat{f}(x, y) = \int_0^\pi P_\phi(r) d\phi \quad (\text{A.2})$$

where $r = x \cos(\phi) + y \sin(\phi)$.

If one substitutes $P_\phi(r)$ by its definition according to the *Radon transform* (Equation A.3) the backprojected image is defined by Equation A.4.

$$P_\phi(r) = \iint_{-\infty}^{+\infty} f(x, y) \delta(x \cos(\phi) + y \sin(\phi) - r) dx dy \quad (\text{A.3})$$

$$\hat{f}(x, y) = \int_0^\pi \left[\iint_{-\infty}^{+\infty} f(x, y) \delta(x \cos(\phi) + y \sin(\phi) - r) dx dy \right] d\phi \quad (\text{A.4})$$

To prevent confusion between variables in the real and backprojected image one must re-write the previous equation:

$$\hat{f}(\hat{x}, \hat{y}) = \int_0^\pi \left[\iint_{-\infty}^{+\infty} f(x, y) \delta(x \cos(\phi) + y \sin(\phi) - \hat{r}) dx dy \right] d\phi \quad (\text{A.5})$$

Applying $\hat{r} = \hat{x} \cos(\phi) + \hat{y} \sin(\phi)$ to the previous equation the backprojected image is defined by:

$$\hat{f}(\hat{x}, \hat{y}) = \iint_{-\infty}^{+\infty} f(x, y) \left[\int_0^\pi \delta((x - \hat{x}) \cos(\phi) + (y - \hat{y}) \sin(\phi)) d\phi \right] dx dy \quad (\text{A.6})$$

After some extensive numerical manipulation, that can be found in Tsui and Frey 2006, the final expression for the backprojected image is:

$$\hat{f}(\hat{x}, \hat{y}) = \iint_{-\infty}^{+\infty} f(x, y) \left[\frac{1}{\sqrt{(x - \hat{x})^2 + (y - \hat{y})^2}} \right] dx dy \quad (\text{A.7})$$

Applying the convolution definition to the previous equation the relation between real and bacprojected image is obtained (Equation A.8). For the real and backprojected images to be equal, and still satisfying Equation A.7, each of the projections must be multiplied in frequency by the Fourier transform of $1/r$. This is equivalent to apply a ramp filter, also known as *Ram-lak* filter, to all projections. The *Ram-lak* filter, and all its variants, are depicted in Figure A.1.

$$\hat{f}(\hat{x}, \hat{y}) = f(x, y) \times \frac{1}{r} \quad (\text{A.8})$$

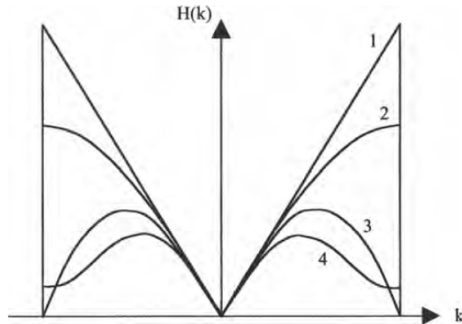


Figure A.1: Common filters employed in filtered backprojection method. 1, Ram-Lak; 2, Shepp-Logan; 3, low-pass cosine; and 4, generalized Hamming. Taken from Gabashvili and Snider 2003